Development of an Integrated Complex 3D Fluidic Device Assembled from Fully Characterised Functional Blocks: Michaelis-Menten Enzyme Kinetics Analysis as a Case Study

Anthony Buchoux

Thesis submitted for the degree of Doctor of Philosophy

The University of Edinburgh

2020

Abstract

The work presented in this thesis demonstrates a new approach to the design of integrated fluidic devices. Most ‘lab-on-a-chip’ are in fact ‘chips-in-a-lab’. The equipment used to operate them, such as microscopes and syringe pumps, is bulky, expensive and the portability is non-existent. Fluidic devices operate on multiple domains, such a fluidics, pneumatics, sensing, control, etc. By integrating the domains to a single device, cost can be reduced and portability increased.

A new manufacturing process was developed to allow for the integration of multiple domains. The vast majority of fluidic devices are two-dimensional, made via soft lithography, which limits the complexity and integration of other components. Three-dimensional fluidic devices can be used to create complex intricate networks and can include sensors, actuators and optics. A negative mould was 3D printed in Acrylonitrile Butadiene Styrene (ABS), encased in Polydimethylsiloxane (PDMS) before being placed in an acetone bath. Because of the swelling properties of ABS in solvents, Acetone could reach the embedded ABS. ABS was liquefied in the presence of acetone, making it possible to be flushed from the PDMS, leaving a void.

Following the development of the manufacturing process, functional fluidic blocks were developed to create more complex devices based on usage. Each block was designed to perform a given task, including a photometric sensor, a proportional valve, a turbulent flow mixer, and storage wells. Using the blocks that were developed, a device designed to perform Michaelis-Menten enzyme kinetics analysis was demonstrated. The device was operated by a combination of a custom PCB and a Matlab GUI, thus creating an

integrated system. Enzyme kinetics were analysed by determining the initial reaction rate of the enzyme-catalysed reactions for various concentration of its substrate. In order to determine reaction rates, it is common to monitor the opacity of the reaction product over time. This is often achieved by using a substrate (or a substrate analogue) which produces a product with a unique optical absorbance, thus the opacity of the product can be monitored by absorption spectroscopy. The experiment was repeated for multiple concentrations before the kinetics were extrapolated. The device created can perform the same task, as well as automating the mixing of any concentration necessary for the kinetic analysis, at fraction of the cost of commercial equipment.

Declaration of Authorship

I declare that this thesis has been composed solely by myself and that it has not been submitted, in whole or in part, in any previous application for a degree. Except where stated otherwise by reference or acknowledgement, the work presented is entirely my own.

Anthony Buchoux

23/01/2020

Acknowledgements

I first and foremost would like to thank my wife Kia for her support and love during those 4 years. I would like to thank my parents Alain and Sylvie, even from abroad they were of great support. I would also like to thank my little sister, Audrey, and my big brother, Florian. I would also like to mention my damaged and lazy cat, Léon for doing absolutely nothing useful.

I would like to thank my supervisor, Dr. Stewart Smith and my second supervisor, Dr. Adam A. Stokes for their guidance and support throughout this project as well as Dr. Vasilis Sboros and Dr. Prashant Valluri. I would like to thank my colleagues and friends for keeping me away from insanity: David, Mags, Ewen, Ilka, Andreas, Ross, Sayed and many more. I would like to thank the technical staff, especially Richard who provided me with litres upon litres of PDMS and acetone.

Finally, I would like to finish with the wise words from a famous French philosopher, Kadoc:

Elle est où la poulette?

Contents

List of Figures

List of Tables

Acronyms

ABS Acrylonitrile Butadiene Styrene

CAD Computer Assisted Design

FDM Fused Deposition Modeling

LED Light Emitting Diode

PCB Printed Circuit Board

PDMS Polydimethylsiloxane

PT Phototransistor

SMT Surface-Mount Technology

UV Ultraviolet

Chapter 1

Introduction

1.1 What is Lab-on-a-Chip?

Lab-on-a-chip integrates multiple discrete laboratory techniques into a system that fits on a chip. This technology is particularly interesting in the life sciences due to advantages over more conventional laboratory testing: low cost due to reduced reagents, decreased detection times, processing capabilities hundreds of times faster than current technologies, high throughput with a potentially massive number of manipulators [4,5]. Integrating fluidic systems to create devices requires a full understanding of the technology being used – whether it be microfluidic, microelectronic, or pneumatic. Soft lithography for the rapid development of microfluidic devices was established within an existing framework for cleanroom manufacturing [6]. Nowadays, a simple one-to-one microfluidic mixing device requires knowledge of the fluidic mechanics, mask design with computer-aided-design software, cleanroom processes, materials and device fabrication, and the experimental setup. The materials used (silicon or glass wafer, SU8 and PDMS) require skilful manipulation during the fabrication. Devices manufactured in the cleanroom using soft lithography have lacked the integration of all the key equipment necessary for operation. Syringe pumps, microscopes, and power supplies are all equipment required to use complex fluidic devices. Portability is non-existent as this equipment is heavy and bulky, leaving the very small lab-on-a-chip limited to the laboratory framework.

1.2 Designing components

The design of individual components is vastly different from integrating various systems into in single device. The upper-level trade-offs need to be done at the early stages of development. For instance, understanding the minimum power requirements can indicate the size, capacity, and functionality of a device before any of the individual components have been designed. Integrated fluidic systems are often designed by extremely experienced researchers who understand the chemistry of the interactions, the physics of the fluidics, and the design of the embedded systems, and can make such trade-offs whilst understanding the impact to the entire system.

1.3 A lack of integration

Up to now, fluidic or microfluidic devices that incorporate lab functionality on a miniaturized scale has been the main focus. Such systems, named lab-on-a-chip, demonstrate the scaling potential outlined by Manz et al. when they proposed the benefits of miniaturizing systems [7]. Manz et al. also defined the term miniaturized (micro) total analysis system, or µTAS as a system that: comprises a channel network wherein the channels have micro-dimensions; can be fabricated into or from a solid substrate; integrates multiple discrete laboratory functions on a single chip; the fluid flow in a microstructure is a required element of the analytical or preparative function of the device.

The term µTAS is less associated with devices nowadays instead representing miniaturized systems for life sciences through a popular conference of the same name. The conference brings together areas of microfluidics, microfabrication, nanotechnology, integration, materials and surfaces, analysis and synthesis, and detection technologies. We see a departure from fluidic devices that integrate many systems. The separation of these subject areas may be indicative of the changes in the community, to move away from devices and focus on components instead.

1.4 Scope of the project

Aims:

The aim of this project was to develop a new way of designing and manufacturing complex integrated fluidic devices with increased portability and usability while reducing the cost associated with cleanroom-based manufacturing.

Objectives:

There are three main objectives for this project:

- Design and characterise a new manufacturing process for fluidic devices in order to increase the complexity of the structures but also reduce the cost and complexity of current manufacturing technologies. Design guidelines, advantages and drawbacks, characterisation of the process and finish product will be addressed.

- Development and integration of simplified, independent components. General purpose components (passive or active), such as wells, connectors or valves and task-specific components, in order to study a specific process such as enzyme kinetics, will be designed and characterised. Integration of multiple domains, such as pneumatic, electrical, optical or fluidic, will be implemented..
- Design, manufacture and test of fully integrated devices. Based on system's requirements, the device will be assembled in CAD using individual components developed prior, manufactured and compared to available equipment regarding accuracy, cost and operator's time usage.

Outcomes:

A new manufacturing process, leveraging rapid prototyping technologies was developed. In order to simplify the design of integrated devices, building blocks performing individual tasks have been designed and characterised. Finally, as a proof of concept, a compact, autonomous and fully integrated fluidic device was created and compared to a laboratory measurement system.

1.5 Contribution to knowledge

A new method of manufacture is proposed, allowing to move away from bespoke solutions and cleanroom-based manufacturing, instead focusing on rapid prototyping technologies. By 3D printing an ABS sacrificial mould, casting PDMS around the mould and dissolving the ABS using acetone, complex 3D fluidic structures can be manufactured. Electronic components can be added before the PDMS is poured, thus increasing the complexity and integration of the device without increasing the cost, both financial and time wise. By leveraging this new manufacturing process, building blocks design for task-specific application can be manufactured and tested independently. Those building blocks can be used to create more complex devices without extensive testing, akin to the design process of electronic circuits. When applied to enzyme kinetics analysis is a practical example, the results show a reduction in cost in orders of magnitude by using off-the-shelf components (battery, electronics, pumps, etc.) while increasing the degree of integration of our device with an array of different interfaces (electrical, pneumatic or fluidic).

1.6 Thesis structure

The thesis will first cover the background of the project in the second Chapter. This will include a review of manufacturing technologies for fluidic devices, fluidic component (including valves, sensors, mixers, etc.). The literature review will also include examples of applications for fluidic devices and well as the materials used to manufacture them. The third Chapter will demonstrate a new manufacturing method, based the lost-core process using ABS and acetone. Each manufacturing step will be explained and manufacturing guidelines will be demonstrated. The fourth Chapter will focus on the development of individual fluidic components, leveraging the manufacturing process seen in chapter 3. The developed components include a port, a reservoir, a chaotic mixer, a proportional valve and a photometric sensor. The design and performance will be demonstrated. The fifth Chapter will focus on the design of a fully integrated fluidic device for enzyme kinetics analysis. The device will be based on the fluidic components developed in chapter 4. The performance of the device will be demonstrated by performing Michaelis–Menten enzyme kinetics analysis and comparing the results with a commercially available tool. The sixth Chapter will discuss the results from each chapter and explore the possibilities offered by the work presented in this thesis as future work. Finally, the seventh Chapter will offer a conclusion to the project.

Chapter 2

Literature Review

2.1 Microfluidics

2.1.1 Introduction to microfluidics

The origin of modern microfluidics can be traced back to the work on inkjet printer nozzles by IBM [8] in the 1960s and the work on gas chromatography at Stanford University [8] during the same period. Experimentation with microfluidics was first published in 1993 [9]. D.J. Harisson described a small network of capillaries (10 by 30 μm) etched in a glass surface. The device was used to separate amino acids via electrophoresis. In 1998, George Whitesides published two papers that changed the world of microfluidics [6, 10]. The microfluidic devices where not manufactured in glass but in Polydimethylsiloxane (PDMS), a transparent silicone elastomer. A negative mould was patterned on a wafer using a photosensitive resin. Then, PDMS was poured over the mould and cured. Once cured, the PDMS was peeled off the wafer, replicating the microfluidic network, and the device would be closed by bonding to a plain layer of PDMS or glass. With this new process, a microfluidic device could be manufactured in a day in a flexible and transparent material. Microfluidic devices typically use small volumes of reagents, from micro litres down to pico litres [11]. Microfluidic devices are used in a variety of research fields, such as chemistry [12–15], bio-chemistry [16–19] or biology [20–23].

2.1.2 Manufacturing technologies

2.1.2.1 Soft lithography

Microfluidics became popular after a simple and quick manufacturing method was published by D.C. Duffy *et al.* [6]. Known as soft lithography, microfluidic devices could be easily manufactured using PDMS in a cleanroom. The soft lithography manufacturing goes as following: (1) the fluidic network is designed via CAD software and a mask is created from the design (2) a substrate is coated with a light cross-linked resin. The thickness of the resin will determine the height of the channels; (3) the resin is exposed to UV light through the mask, selectively curing the resin, and thus creating the pattern of the fluidic network. The uncured resin is washed away; (4) PDMS is poured over the substrate, covering the resin pattern; (5) once cured, the PDMS is peeled off the substrate. As the resin remains on the substrate, the fluidic network is reproduced in the PDMS; (6) finally, the PDMS is bonded to a new substrate to close the channels. The substrate can be PDMS, glass, silicon etc.. If necessary, ports can be punched through the PDMS, connecting the network with external devices.

This methodology greatly simplifies the manufacturing of microfluidic devices. Previously, microfluidic devices were manufactured by etching the network in glass [9], requiring expensive laser equipment while bei*ng extremely fragile. By using a negative mould, microfluidic devices can be manufactured in bigger quantities and the use of PDMS means that the microfluidic devices are durable. Additionally, being able to seal off the network with a silicon substrate introduces the possibility of integrated sensing. Electrodes can be manufactured on the silicon and the PDMS microfluidic device can be placed above the sensing area [24–26].

2.1.2.2 Micromachining

Micromachining or computer numerical control manufacturing (CNC), offers an alternative to soft lithography. This subtractive manufacturing method removes material with specialized tooling spinning at high speeds. A fluidic network can be manufactured by removing successive layers. Metals, ceramics and plastics can be machined to offer a range of material that can be used based on chemical and temperature tolerances required for the microfluidic devices. Chen *et al.* [27] demonstrated fluidic devices manufactured in polycarbonate using a high-speed spindle with an average wall roughness of 0.15 µm ± 0.08 µm. As demonstrated by Yen *et al.* [28], micromachining can offer a cost-effective platform for rapid prototyping of microdevices removing the clean room step necessary for the soft lithography process. More recently, Lashkaripour *et al.* [29]. demonstrated ongoing work to optimize the manufacturing of microfluidic devices on polycarbonate using a desktop CNC machine. They manufactured patterns with feature sizes as small as 75 µm and determined that surface roughness was reduced with lower step-overs. Their work concluded that due to the size of the cutting tools, feed rates should be greatly reduced compared to manufacturer specifications.

2.1.2.3 Paper microfluidic

Paper microfluidic presents a low-cost alternative to the manufacture of microfluidic devices. Channels are patterned on a piece of paper using a wax printer. The wax is melted and infuses through the paper to create hydrophobic barriers. Fluidic devices can be designed and manufactured in minutes [30,31]. The low cost and biodegradable materials offer good solutions for devices that must be single use, such as blood sample analysis.

Xu *et al.* [32] demonstrated a complex design of paper microfluidic. By using origami techniques, they were able to create multilayer devices. Using 5 layers, the device was able to perform 4 tests for the detection malaria, using a single drop of blood. Martinez *et al.* [33] used a different technique to create multilayer device. Each layer of paper were stacked on top of each other, separated by double sided tape. Through holes were cut to allow liquids to travel through the layers and thus created the 3D network

2.1.2.4 Additive manufacturing - 3D printing

Three-dimensional printing is a flexible tool to create complex fluidic devices. Kitson *et al.* [34] demonstrated simple chemical reactors manufactured by fused deposition modelling using polypropylene. The devices used 1/16” connectors to PTFE tubing with channel sizes of 800 µm. Although the devices showed limited use of the 3-dimensional aspect of the manufacturing technique, several chemical reactions were conducted successfully and demonstrated the possibilities of 3D printing for microfluidics. Using Stereolithography (SLA) printing Anderson *et al.* [35] manufactured a microfluidic device that incorporated a threaded port for a simple connection to syringe pumps and cavities for cell culture inserts. The device included an array of 8 channels, 3 mm wide and 1.5 mm deep. Using the same SLA printing technology, Shallan *et al.* [36] produced a series of complex 3D microfluidic devices, including a 3D mixer, a gradient generator, a droplet generator and a tool to analyse nitrate in tap water. They were capable of producing fluidic channels as small as 500 µm by 500 µm, showing that complex microfluidic devices could be manufactured for a low cost.

2.1.2.5 The lost-core method

The lost-core method consists of creating a negative mould, encasing the mould in the manufacturing material and removing the core. Threads of molten sugar, easily dissolved in water, can be used as a sacrificial material [37]. The sugar fibres are stretched between two thicker wax cores, acting as inlet and outlet, before being embedded in PDMS. Once the PDMS is cured, the microfluidic devices is placed in a bath of water and ethanol for several days, maintained at 70°C. The resulting microfluidic device has a large network of channels, with diameters ranging from 1 to 100 µm. However, there is no control over the geometry nor the diameter of the channels. Therriault *et al.* [38] developed a controllable manufacturing process to create 3D microfluidic devices. A sacrificial material is 3D printed with a fugitive organic ink (a non-permanent type of ink that can be modified with heat, light, humidity, etc.), creating a scaffold of circular channels less than 200 µm in diameter, overlapping each other. An epoxy resin is poured over the scaffold and cured, before the sacrificial material is removed. Subsequently, the gaps are filled with a photo-curable resin, and carefully designed masks are placed around the device, to allow the selective curing of the resin. The unexposed resin is washed out with water, leaving the desired network of channels behind with circular channels. This work shows a limited control on the geometry, but is a complex manufacturing process. Only channels of the same diameter can be manufactured, and their orientation is very limited. Freitas et al. [39] described a methodology to manufacture an optically transparent blood flow phantom. The fluidic network is modelled from CT scan data and converted to a printable file. A negative mould is manufactured using Acrylonitrile Butadiene Styrene (ABS) with a Fused Deposition Modeling (FDM) printer, and smoothed with sand paper. PDMS is then poured over the mould and cured. To finish the device, the mould is mechanically pulled from the PDMS block, leaving a void. While being able to control the shape and surface of the device, this technique lacks network complexity, as the negative mould has to be fairly straight and strong enough to be pulled out of the PDMS block without risking destroying the phantom. The manufacturing of a more complex 3D microfluidic network was made possible by Geoghegan *et al.* [40] using a sacrificial core, 3D printed using a plaster powder based 3D printer. Once the model is printed, instead of being strengthened with epoxy as is usual for the printing technology, the core is covered in Polyvinyl Alcohol (PVA), making it impermeable to PDMS while giving it a more realistic surface finish. When embedded in PDMS, the sacrificial core is washed away in water, leaving a void behind. The described manufacturing process allows for more complex accurate 3D fluidic devices compared to previous attempts. Unfortunately, the printing technology does not allow for small elongated features, like microfluidic channels, to be made. Such designed would simply break due to the low strength of the finished product printed using a plaster based printer. Figure2.1 shows the blood flow phantom manufactured.

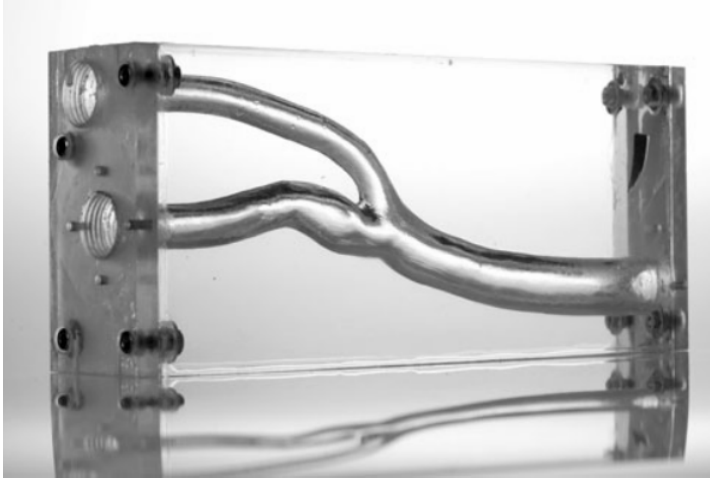

Figure 2.1: Blood flow phantom manufactured using a 3D printed plaster core, washed away with water [40].

2.1.2.6 Comparison

A comparison of the manufacturing techniques is summarised in Table 2.1. This table can be used to choose a manufacturing process based on the requirement of the design. For example, if the minimum feature size is important, then soft lithography is the best candidate. If cost is a concern then paper based microfluidic is the most suitable choice.

Table 2.1: Comparison of the manufacturing techniques

	Soft lithography	CNC	Paper	3D printing	Lost core
Min. feature size	Very high	High	Low	Medium	Medium
Cost	Very High	Medium	Very low	Low	Low
Complexity	Medium	Medium	Very low	High	Medium
Integration	Medium	Low	Low	Medium	High
Lead time	Low	Low	Very low	Low	Medium
Skill level	High	Medium	Very low	Very low	Low

2.1.3 Components

2.1.3.1 Mixers

Mixers are a key component in microfluidic devices. By definition, microfluidics is the handling of fluids through microchannels. Being able to mix different fluids is essential to perform experiments. Laminar flow mixers aid to create a wide number of solutions on a single package [41]. Two inlets merge to a single channel via a Y-junction. Due to the laminar nature of the flow, the solutions do not mix but diffuse into one another, creating a gradient across the channel [42]. By placing multiple outputs at the end of the channel, a wide range of concentrations can be prepared at once. The longer the channel, the more the solutions will diffuse into one another. If the length is sufficient, the solutions will be fully mixed. Turbulent flow mixers offer different advantages. By creating turbulence, the size of the mixer needed to create a fully mixed solution is much smaller. Hong *et al.* [43] proposed to use Tesla microstructures to induce turbulences for the design of planar mixers (i.e. 2D). A fluidic channel is split into two and merged back together after one of them made a 180° turn. The two flows merging together with opposite flow directions creates large turbulences. mixing, sample preparation. Ahmed *et al.* [44] proposed an innovative design for a micromixer. A wide chamber was flanked by recesses on either side where air bubbles were trapped. A piezo transducer was placed nearby. Two fluids were introduced in the mixer via two inlet ports and the transducer was switched on. The vibration from the transducer would induce pressure waves in the air bubbles, creating turbulences in the fluid, thus mixing the solution.

2.1.3.2 Microvalves

The design of valves is an important aspect of microfluidics. Valves are used to control the flow in the device, allowing for higher level of integration. Unger *et al.* [45] developed a simple ON/OFF valve. The valve requires two layers to function, a control layer and a fluidic layer. Each layer has a channel and the control layer is placed above the fluidic layer, in a cross pattern. The intersection of the two channels forms the valve. When pressurised air in applied to the control channels, the wall between the two channels deforms into the fluidic channel, blocking the flow. Opening switching frequencies as high as 400 Hz where achieved with a combination of 100 µm channels for both layers. This work formed the basis for much more complex devices. Furst *et al.* [46] created a fluidic memory device combining 1000 independent compartments and 3574 microvalves. The second device demonstrated had 2056 microvalves 256 reaction chambers. Biswas *et al.* [47] presented a valve without any moving part. By depositing a hydrophobic coating, called self-assembled monolayer, on a platinum electrode, directly in contact with the fluid, they could stop the flow. When a small electrical potential (between -1.0 V and 1.0 V) was applied to the electrode, the valve was opened, with a switching time of a few seconds.

2.1.3.3 Sensors

Microfluidic based sensor have the potential to reduce the size of microfluidc devices and turn them into true lab-on-a-chip by doing the sensing locally, as opposed to a large, lab-based apparatus. Up to now, only a few examples of embedded sensors have been developed. Mitrovski *et al.* [48] demonstrated a Pt InterDigitated Array (Pt-IDA) working electrode used to monitor the level of oxygen in an microlfulidic device.

The sensor was embedded in the PDMS and was part of the fluidic device. Redha *et al.* [49] demonstrated a microfluidic device, made by injection modelling, where a printed carbon electrodes was embedded into the fluidic network. The chip was used successfully for voltametric and electrochemiluminescence (ECL) measurements. For low-cost application, Delaney *et al.* [50] demonstrated a disposable paper based sensor. Using electrochemiluminescent detection and the camera from a smartphone, they were able to manufacture a sensor capable of detecting nicotinamide adenine dinucleotide (NADH) with concentration varying from 0.9 µM to 72 µM. Because NADH is from the same species as ethanol, glucose or lactate, the team demonstrated that, in principle, it was possible to detect a wide range of analytes using low-cost disposable paper-based sensors.

2.1.4 Applications for microfluidic

2.1.4.1 Biology

Currently, before drugs can be tested on humans, researchers have to use animal models. Such use of animals is controversial for ethical reasons [51]. Researchers are required to demonstrate and justify the need for animal models, which slows down the pace of research. Organ-on-a-chip has the potential to change the way drugs are tested [52]. By reproducing fully functional miniature organs in microfluidic devices, drugs can be tested without causing suffering [53]. Another benefit is that human cells can be used in those devices, which reduces the risk of the drugs being reject during human trials [54]. An example of organ-on-a-chip is the lung-on-a-chip developed by Dongeun H. *et al.* [55]. The device consists of 2 fluidic layers. At the centre of the device is a chamber, divided in two by a porous membrane. On one side of the membrane endothelium cells (i.e. cells present on the inner surface of blood vessels) are grown. On the other side of the membrane are epithelium cells (i.e. lung cells). This configuration reproduces the alveolar-capillary interface. On each side of the central channel are two pneumatic chambers. By putting the chambers under vacuum, the porous membrane is stretched and mimics the stress induced by breathing. The response of the cells was successfully tested by introducing bacteria, inflammatory cytokines and silica nanoparticles into the system. Recently Zhang *et al.* [56] developed a complex organ-on-a-chip using a biodegradable scaffolding. The same design was used to mimic a blood vessel, with the channel coated with endothelium cells. The porosity of the scaffolding reproduced the interstitial space and movement of monocytes was observed through the wall of the blood vessel. The same scaffolding was used to mimic a vascularize liver and vascularize cardiac tissues.

2.1.4.2 Enzyme kinetics

Enzymes are biological catalysts. They accelerate the transformation of a substrate into a product within the cell. This is necessary for the metabolism, as naturally occurring reactions are too slow to sustain life [57, 58]. The study of enzyme kinetics is useful to understand how they work, their role in the metabolism and for the development of drugs [59–61]. The rate of the reaction can be influenced in several ways:

- The concentration of the substrate
- The presence of an inhibitor
- Temperature

- The pH of the solution

A single substrate enzyme reaction can be simplified as a two step mechanism which occurs as follows:

$$E + S \Leftrightarrow ES \Leftrightarrow E + P \tag{2.1}$$

where:

- E is the enzyme
- S is the substrate
- P is the product

The enzyme and substrate bind together forming the ES complex, then the formation of product occurs before being released by the enzyme. Michaelis and Menten [1] demonstrated that the rate of the reaction was proportional to the concentration of substrate and could be predicted with the following equation:

$$v = \frac{v_{max}\,[S]}{K_m\ + [S]} \tag{2.2}$$

where:

- v : reaction velocity
- v_{max} : maximum reaction velocity
- *[S]* : substrate concentration
- K_m : Michaelis-Menten constant

In order to find K_m an enzyme assay is performed. One of the common methods is to perform a spectrophotometric assay [62–67]. The absorbance of the solution is observed as the reaction occurs. The change of absorbance can be correlated to the initial velocity of the reaction, which is recorded at different substrate concentrations. The resulting values can be fitted in the Michaelis–Menten saturation curve, see Figure 2.2.

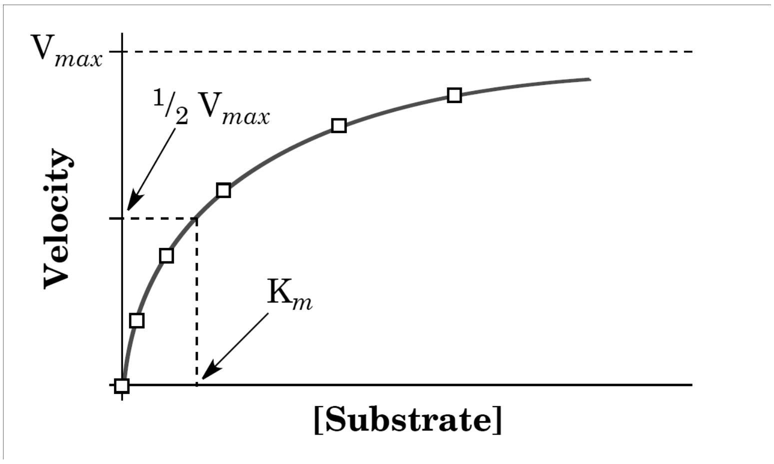

Figure 2.2: Michaelis–Menten saturation curve [1]

Examples of microfluidic devices used of enzyme kinetics are numerous. Song *et al.* [68] demonstrated a microfluidic device capable of performing enzyme kinetics analysis. The simple device consisted of a mixer and a long serpentine channel. The mixer is used to combine the enzyme and the substrate. The resulting solution then flows along the channel where the reaction takes place. The channel is designed to be long enough for the reaction to happen in full before leaving the device. A camera is placed above the serpentine channel and records the reaction. The change in colour is then analysed and the enzyme kinetic can be determined. A more improved version was proposed by Han *et al.* [69]. Instead of a fixed length, the serpentine channel could be extended or reduced using pneumatic valves to change the path of the flow. This device was designed to be used for enzyme kinetic analysis with different reaction time. By changing the length of the channel, the experiment can be conducted at a faster pace.

2.2 Polydimethylsiloxane (PDMS)

Polydimethylsiloxane (PDMS) is a silicone polymer, which, when mixed with a cross linker, creates a optically transparent rubber. PDMS is a soft material, with typical Young's modulus of 1-3 MPa [70–72]. It is mostly bio-compatible [73–76] and permeable to most gases [77–79]. PDMS is hydrophobic, with a contact angle of around 110° [80–83]. Hydrophobicity of PDMS can be a problem for microfluidics, it can have an influence the formation of droplet [84, 85] and will act against flow of water, requiring pumps for transport through the network.

The most commonly used form of PDMS for the manufacturing of microfluidic devices is Sylgard 184 [6,10,13,71,86–89]. Sylgard 184 is manufactured by DowCorningDupont and is a two part product, sold as a kit. A PDMS oligomer is mixed with a platinum based curing agent, at a ratio of 10:1 (by weight). Curing time depends on the temperature, ranging from 48 hours at room temperature, to 10 minutes at 150 °C, according to the manufacturer [86].

2.2.1 Polydimethylsiloxane mechanical properties

The Young's modulus of PDMS varies greatly by varying two parameters: reducing the amount of curing agent decreases the stiffness while curing the PDMS at high temperatures increases the stiffness. J.Y. Choir *et al.* [71] showed that the stiffness of PDMS could be changed from 1.74 MPa for a 20:1 ratio to 3.57 MPa for a 10:1 ratio

(PDMS cured at 60°C for 12 hours). I.D. Johnston *et al.* [72] studied extensively the mechanical properties of PDMS by varying the curing temperature (curing time was adjusted according to the manufacturer's recommendations), the PDMS was prepared with a 10:1 ratio. At a curing temperature of 25°C, the Young's modulus of PDMS was found to be 1.32 MPa. At a curing temperature of 200°C, E reached 2.97 MPa, showing that the stiffness of PDMS increases with temperature. A Young's modulus of 1.72 MPa for PDMS with a 10:1 ratio, cured at 65°C for 12 hours, was similarly found by R.N. Palchesko *et al.* [70]. Similar to the Young's modulus, tensile strength was found to vary with the oligomer:cross linker ratio and the curing temperature. I.D. Johnston *et al.* [72] found the tensile strength to vary from 3.51 MPa to 7.65 MPa with increased curing temperature (from room temperature to 200 °C). Those values are consistent with DowCorningDupont's own data sheet, showing a tensile strength of 6.7 MPa [86].

2.2.2 Polydimethylsiloxane chemical properties and behaviour in the presence of solvents

An extensive study of PDMS compatibility with solvents was carried by J.N. Lee *et al.* [90]. The swelling ratio of PDMS was studied and a measurement of the length of the samples was taken before being exposed to the solvent and right after being taken out of the solvent bath. The swelling was calculated as a ratio of the increased length over the original length. Some of the solvents studied had a no swelling effect, such as water, but some, such as diisopropylamine, had a swelling ratio of 2.13, and could potentially damage a microfluidic device. Other solvents like acetone had had limited swelling capacities, with a swelling ratio of 1.2 . The same study revealed that the swelling of PDMS in acids and bases was largely non-existent. When swollen with solvents, structures in the microfluidic device will be deformed, which can be calculated [91], changing the flow and the characteristics of the device. Great effort has been made to make PDMS resistant to organic solvents by surface treatment, such as coating the surface with perfluoropolyether [92], with a hybrid inorganic/organic polymer (HR4) [93], or by modification of the surface using poly(urethaneacrylate) [94].

Chapter 3

The Lost-Core Method for the Manufacture of 3D Fluidic Structures in PDMS

3.1 Introduction

This chapter presents a novel manufacturing process for the fabrication of complex of 3-dimensional fluidic devices using the lost-core method. 3D printed ABS scaffolding are embedded in PDMS and cured, after which the ABS is dissolved with acetone. The first section describes the limitations of the manufacturing technique as well as the design constraints that have to be taken into consideration during the design process. The second section describes the manufacturing process by explaining each step necessary to make a simple 3D fluidic device. The third section studies the effect of the acetone bath on the mechanical properties of PDMS.

3.2 Design Specifications

The manufacturing process should meet the following requirements:

- Complexity: the manufacturing process should enable the design and fabrication of complex 3D fluidic structures, down to a 1 mm feature size.
- Low cost: the manufacturing process should not require the use of expensive consumables or expensive equipment. The access to a cleanroom should not be required.
- Integration of electronic components: the manufacturing process should allow electronics to be embedded into the fluidic network. Direct contact of the electronic with the fluid flowing inside the channels is desirable.
- Low technical skills: the person using the manufacturing method should be able to do so with minimum training.

The manufacturing process described in this chapter uses the lost-core method: (1)A negative mould of the fluidic device is 3D printed in ABS. (2)The mould is processed with acetone do reduce the surface roughness inherent to FDM printers. (3)PDMS is poured into the mould and cured at 60°C for 2 hours. (4)The mould is placed in an acetone bath for 48 hours. The PDMS swells in the presence of solvents, allowing the acetone to reach and liquify the the embedded ABS. (5)The fluidic device flushed of the liquified ABS and cleaned. It takes 48 hours for the acetone to fully evaporate. This manufacturing process allows for the creation of complex structures. Electronic components can be integrated before the PDMS is poured while surviving the acetone bath. The manufacturing process requires little skill and by using inexpensive tools and consumables, the fluidic devices can be made at a low cost.

PDMS is used for a large number of microfluidic devices, see Section 2.1.3, therefore its characteristics are well documented. One property of PDMS is that it swells in the presence of solvents [90, 91] and the problem can be solved by surface treatment or by adding chemical components to the PDMS to change its properties [92–96]. For the manufacturing process described in this chapter, the swelling property of PDMS is an advantage. By flowing through the PDMS, acetone can reach the embedded ABS. ABS liquifies in the presence of polar solvents, such as acetone [97–99], therefore the sacrificial material can be removed without risking damaging the fluidic device. Once cleared of ABS, the fluidic device can be left to rest at room temperature and the acetone will evaporate out of the PDMS due to its low vapour pressure (30.6 kPa at 25°C). PDMS is transparent, a key advantage during the manufacturing process. If any ABS remains present in the channels during the cleaning and flushing phases, it can be easily spotted and removed.

3.3 Design Guidelines

Before designing a mould, outlining guidelines are necessary to ensure the part comes out of the printer as intended and can survive the fabrication process. The manufacturing is mostly limited by the equipment used and the nature of the process itself.

3.3.1 Understanding the 3D printer's limitations

The diameter of the channels are determined by the printer used, more specifically the layer thickness and the layer width. If a printer has a layer thickness of 250 µm then the channel cannot be any smaller. Unfortunately, the material deposited by the 3D printer does not result in a square shape but has a rectangular cross section, therefore more than one layer is necessary to print a round channel. A one layer square could be used to manufacture a channel, as the acetone smoothing process would round the corner, although it would not be circular. Figure 3.1 shows an example of how a round channel could be printed if it was 4 times the diameter of the layer thickness, and was printed parallel to the printer bed.

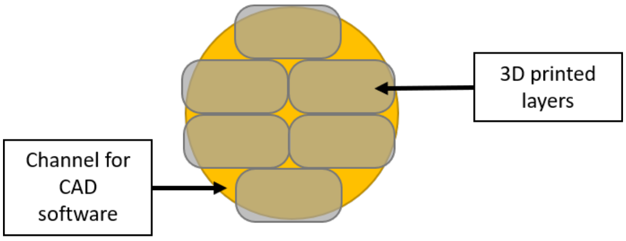

Figure 3.1: Graphical representation of how a thin feature is produced by a FDM printer when the parallel to the bed

Similar reasoning applies if the channel is printed perpendicular to the printer bed. 3D printers build parts by adding layers of material on top of each other. FDM parts are the weakest at the interface between two layers [100–103]. If the surface area between two layers is small, the part is more likely to delaminate. Printing a channel vertically with a length much greater than its diameter would result in a lot of layers with a very small surface area between each of those layers, creating a fragile part. Therefore, the devices described in this thesis will always be designed with the longer channels parallel to the bed.

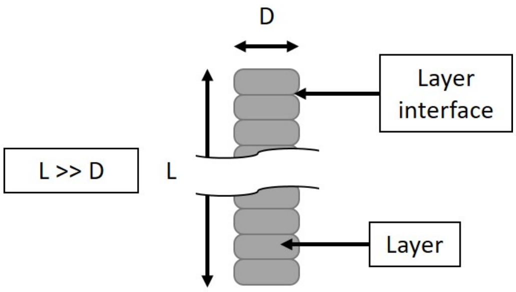

Figure 3.2: Graphical representation of how a circular feature is produced by a FDM 3D printer when perpendicular to the bed

3.3.2 Account for structural limitations

This methodology allows the creation of very complex networks but some design guidelines are necessary to ensure the manufacturing will be successful:

1. Consider how to flush the material out of the device. The acetone will reach everywhere and dissolve all of the embedded ABS but how it will be removed has to be planned at the CAD design stage. Small channels leading to large cavities will need an inlet and an outlet to flush out the liquified ABS. Without an outlet it will be very difficult if not impossible. The output can be sealed later if it is not necessary for the device. Figure 3.3 a) shows a design that was extremely difficult to clear of liquified ABS due to the multiple parallel channels connecting to the same main channels. Once one path was cleared, the remaining liquefied ABS could not be flushed out.

2. Be aware of hidden cavities. If cavities are upside down when the PDMS is poured, they will trap air creating unwanted features.

3. Small cavities may be filled with liquefied ABS during smoothing process, and

sub-millimetre features could be erased. A shallow depression on a surface will be filled and narrow cavities blocked when exposed to acetone.

4. Channels smaller than 1 mm should be avoided or they could warp/break, especially if they are a couple of centimetres long.

5. Flat surfaces need to be a minimum of 0.5 mm apart. The viscosity of acetone will increase with the quantity of ABS it has dissolved and will easily accumulate if two surfaces are close to each other due to surface tension. The acetone evaporates quickly and will create a bridge between the surfaces that will be difficult to separate.

6. The device should not be placed in high temperature environment immediately after the smoothing process, as acetone is still present in the surface on the ABS. The higher temperature will increase the evaporation rate of acetone an lift off an small layer of ABS from the surface. Figure 3.3 b) shows a device that was put in an oven at 60°C 20 minutes after the acetone smoothing process. Large quantities of bubbles can be observed on the surface. Furthermore, the presence of acetone inside the ABS makes the mould mechanically weaker.

7. The device should not be left to rest for more than 4 hours. The presence of acetone in the ABS as it evaporates will put stress on the device and large surfaces will start to warp, witch could lead to some of the structures touching each other. Figure 3.3 c) shows a device that has been left to rest for 48 hours after the acetone smoothing step. The top channel is touching another part of the device, making the mould unusable.

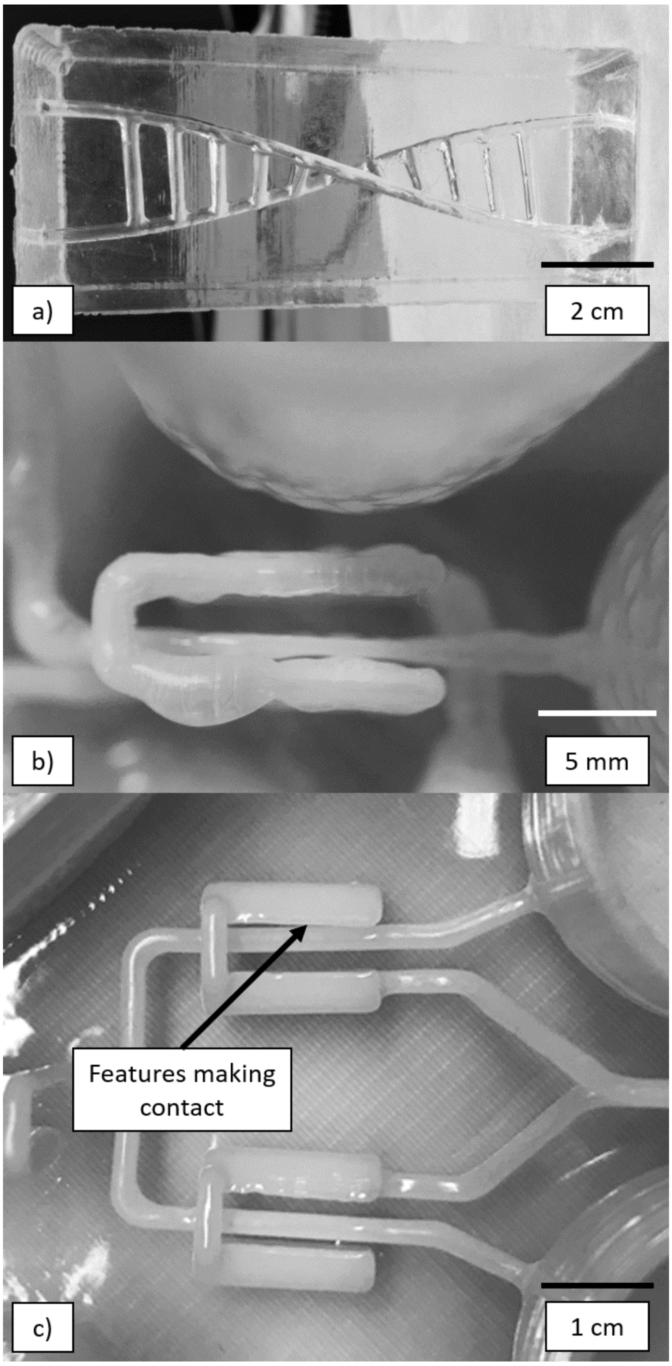

Figure 3.3: a) Example of design where the channels were extremely difficult to clear of liquefied ABS. b) Example of a device 48 h after the acetone smoothing. The walls warped and some of the features are now touching each others. c) Example of a device placed in an oven at 60°C 20 minutes after the acetone smoothing step. The surface of the mould is covered with bubbles

3.4 Manufacturing Process - Lost-Core Method Using ABS and acetone

The lost-core method consists of creating a negative mould, which replicates the desired part, encasing the mould in different material and removing the mould leaving a void behind. Removing the core can be done by different means:

- Mechanically, by pulling the mould from the device
- With heat, the mould will melt and flow out
- Chemically, the mould is dissolved from within the device and flushed out.

Section 2.1.2.5 provides a detailed explanation of the lost-core method. To demonstrate the manufacturing process, a simple 3D structure not manufacturable using traditional methods was made.

3.4.1 Mould design

For demonstration purposes, a simple 3D fluidic device that can be easily manufactured using this process only was designed using SolidWorks 2015 [104]. The mould is a negative image of the final microfluidic device. The structure consists of two 1.5 mm diameter channels 5 mm apart, twisting around each other for 2 full rotations. A 1 mm thick wall on the sides and bottom is added to contain the PDMS while it cures. The final fluidic device is 60 mm long, 15 mm wide and 10 mm deep, or 62 x 17 x 11 mm including the casing (Figure 3.4).

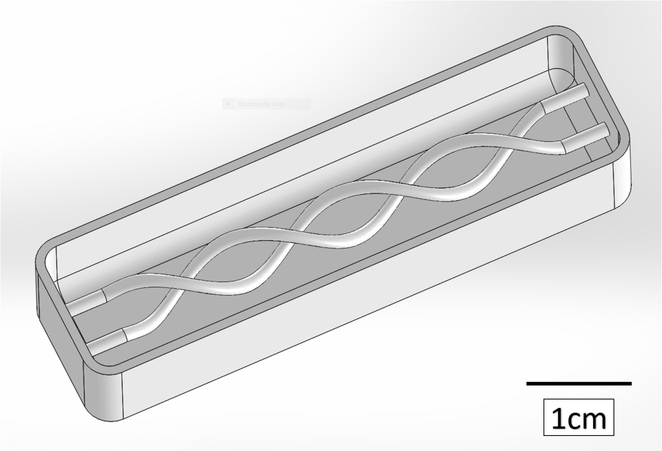

Figure 3.4: CAD design of a sacrificial mould with two 1.5 mm diameter channels and the casing used to hold the PDMS before it cures

3.4.2 3D printing of the sacrificial mould

The design is exported as a STL file, a commonly used file type by 3D printer software packages. The device is printed with a Stratasys Print SE ABS 3D printer [105], via the provided CatalystEX software, see Figure 3.5 a). This printer has a minimum layer thickness of 254 µm with a x/y resolution of 25 µm. This printer model is expensive both to buy and to operate. The price for a 1 L spool of material is £350. Although the costs are high, the printer is both reliable and consistent and the prints come out with a high fidelity. The printer also uses a soluble support material, allowing the printing of complex and fragile structures that would otherwise be impossible with a printer using only one extruder. Once printed, the mould is put in a bath to remove the support material. The support material is a combination of Terpolymer of Methacrylic Acid, Styrene and Butylacrylate [106] dissolved with an Alkaline cleaning agent [107], mixed with hot water (the exact compositions are unavailable, being commercial products). Figure 3.5 b) shows the sacrificial mould after the support material is washed away.

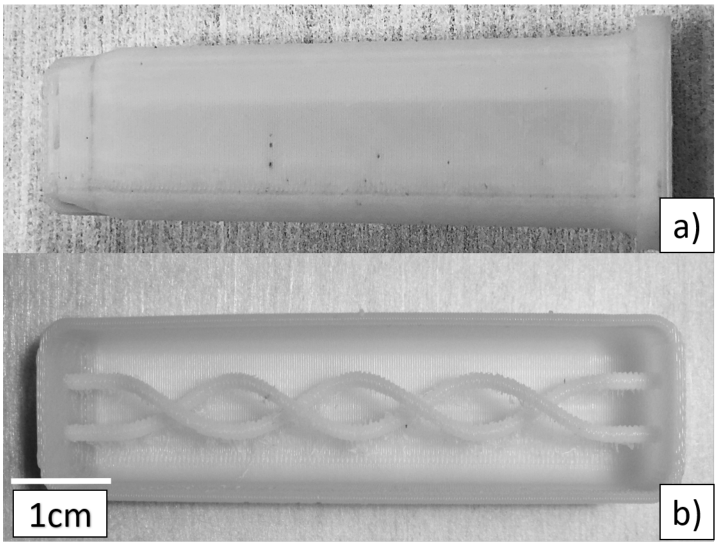

Figure 3.5: ABS sacrificial mould a) before and b) after dissolution of the support material

3.4.3 Acetone smoothing of the mould surface

As seen if Figure 3.5, Fused Deposition Modeling (FDM) technology creates a rough surface finish, especially when the dimensions of the parts are close to the printer's resolution. To have better flow in the channels, because rough surfaces increase flow resistance, and to enhance transparency, smoothing of the surfaces is necessary. One solution is to use sand paper to clean the rough surfaces, although for such small features and with surfaces that are not directly accessible, it would be impossible. As presented in 3.2, ABS is dissolved by acetone, a property that can be used to smooth the surface. They are two possible ways to use acetone to smooth the surface, either in acetone vapour or liquid acetone. The use of acetone vapour takes a long time, a minimum of 24 hours, but is less prone to mishaps, such as over exposure that can lead to the destruction of the printed part. The use of liquid acetone bears more risks but is more time efficient, as only a few minutes are necessary to smooth the surface of the entire device.

For this reason, the liquid acetone solution is used for the manufacturing process. The mould is completely filled with acetone. After 15 s the acetone is removed and the mould carefully dried with compressed air. Once all the acetone is evaporated, this step is repeated a second time. Extra care is taken with this step, as if the compressed air flow is too high, it risks lifting a thin layer of ABS of the mould, essentially creating an air bubble on the surface. If that happens, a third exposure to acetone is necessary.

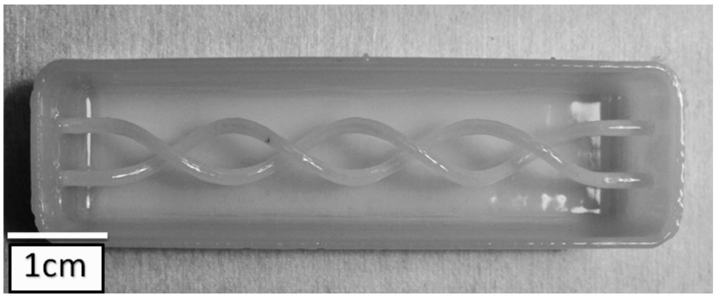

Figure 3.6: Sacrificial mould after the surface was smoothed with liquid acetone

Figure 3.6 shows the mould after the surface smoothing step. Once the surface treatment is finished, the device is left to rest for 2 hours. The ABS still contains small quantities of acetone and pouring PDMS in the mould would create bubbles as the acetone evaporates.

3.4.4 Preparation of the Polydimethylsiloxane and its curing

Once the mould is ready and resting, PDMS, Sylgard 184 [86], is prepared as per the manufacturer's instructions (10 parts of monomer for 1 part of curing agent) and mixed for 1 minute by hand. Due to the high viscosity of PDMS (3.5 Pa.s), a lot of bubbles are created during the mixing. Therefore, the PDMS is placed under vacuum for 45 minutes to remove any bubbles (time varies with the quantity of PDMS and the equipment used). The PDMS is then poured in the mould. While pouring, extra care is taken to prevent the formation of bubbles. Once the PDMS is in the mould, it cannot be degassed again. 3D printed ABS is porous and contains air pockets. If put under vacuum, some of the gas will move into the PDMS, forming more bubbles and greatly increasing the degassing time. If a few bubbles are formed, a pipette is sufficient to extract or burst them. Once the mould is filled up, the device is put in a convection oven at 60 °C for 2 hours. Figure 3.7 shows the device after the PDMS is cured.

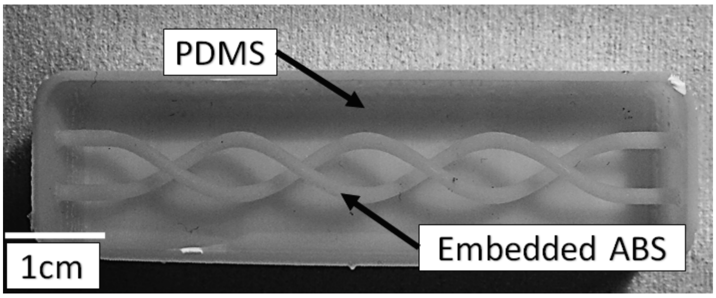

Figure 3.7: Sacrificial mould after the PDMS cured (60 °C for 2 hours)

3.4.5 Dissolution of the sacrificial mould in acetone and evaporation

Once the PDMS is cured, the device is placed in an acetone bath, at room temperature. Figure 3.8 shows the polypropylene container used for the acetone bath, due to its resistance to damages from solvents [108, 109], including a sealed lid, preventing the evaporation of acetone over time.

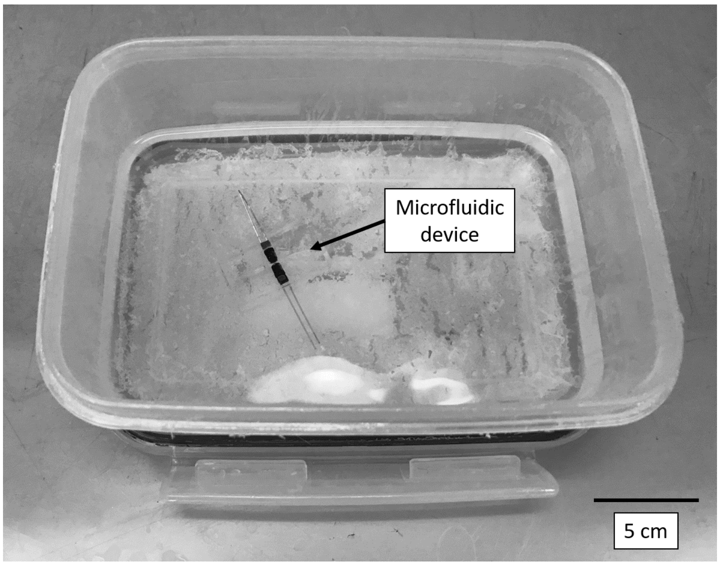

Figure 3.8: Polypropylene bath used to dissolve the ABS embedded in PDMS with a microfluidic device submerged in acetone

The length of time spent in the bath depends on the volume of the device, however for the example shown here, 24 hours is sufficient. When taken out of the bath, the device is fully swollen as the acetone had reached every part of the PDMS, dissolving the embedded ABS. A 3 ml pipette is used to clear the liquified ABS from the channels but care must be taken to prevent any damage. When swollen with acetone, PDMS becomes more fragile and can be easily torn, potentially destroying the device. After the ABS is flushed out, the device is cleaned with fresh acetone and left to rest in a fume cupboard for the acetone to completely evaporate from the PDMS. 24 hours was the time necessary for the devices described here. This time can be reduced by placing the device under low pressure, such as in the vacuum vessel used to degas the PDMS.

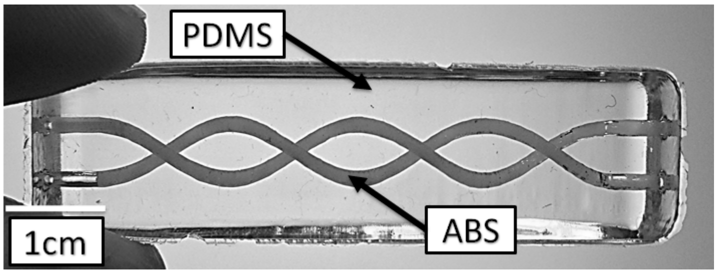

Figure 3.9: Microfluidic devices with the shell removed, showing the ABS encased inside the PDMS

Figure 3.9 shows the device with the casing removed, for illustration purposes. Although removing the casing reduces the quantity of ABS to be dissolved, and could potentially speed up the swelling of PDMS, it could result in irreversible damages to the microfluidic device. Figure 3.10 shows the finished device after treatment in the acetone bath with the acetone fully evaporated from the PDMS.

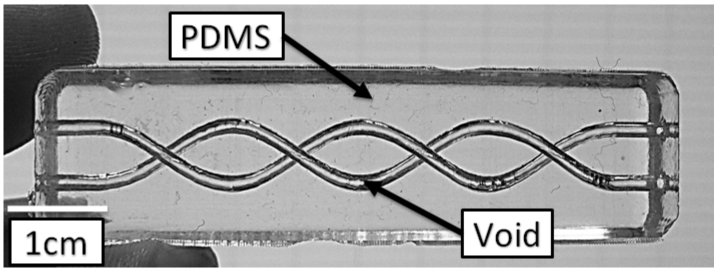

Figure 3.10: Finished microfluidic device. The ABS was flushed out and the device was left to rest until the acetone had evaporated.

3.5 Mechanical testing of PDMS after acetone bath

Tensile and compressive tests are conducted to study the effect of the acetone bath on mechanical properties of PDMS. As explained in 3.2, PDMS swells in solvents. PDMS swollen by acetone becomes fragile and easily tears. Therefore it is possible that the acetone bath could physically damage the PDMS and change its mechanical properties. The samples for the mechanical testing, six for tensile test and six for compressive test, were made from Sylgard 184, with a ratio monomer/curing agent of 10:1, as per the manufacturer's recommendation, and cured at 60 °C for 2 hours in a convection oven. Each batch of PDMS is mixed with a magnetic stirrer for 5 mins (120 rpm, room temperature), as previous experiments revealed that poor mixing significantly changed the Young's modulus and produced unreliable data. When cured, three tensile samples and three compressive samples are submerged in acetone for 72 hours before being left to rest for the acetone to evaporate fully. The rest of the samples are left untouched. The dimensions of the samples are taken using digital vernier calipers. The design of the tensile sample is 80 mm long, 15 mm wide and 5 mm thick, with a cross section A of 75 mm^2, shown in Figure 3.11 a). The compressive sample is designed as a cylinder with a height of 10 mm, a diameter of 10 mm and a cross section A of 78.5 mm^2, see in Figure 3.11 b).

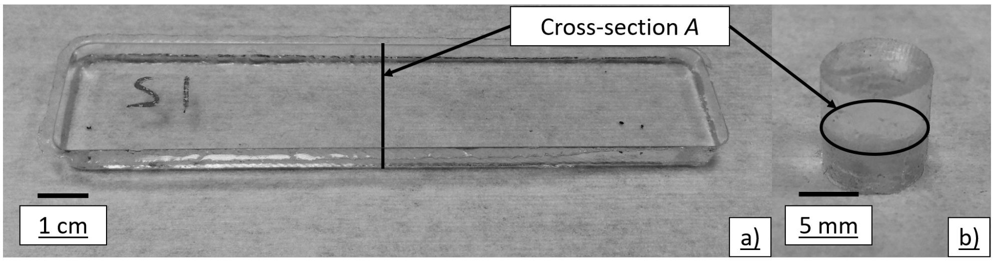

Figure 3.11: Sample used for a) tensile test and b) compressive test

Due to manufacturing variability, the samples have different dimensions. This can be explained due to multiple factors. The acetone smoothing modifies the surface of ABS and can change the dimensions of the mould. Although all the samples come from the same mould, the width of the tensile samples, as well as the diameter of the compressive samples, are not the consistent. Measuring the thickness of a soft material with a digital vernier calipers can be difficult and leads to small errors. The increased thickness is simply explained by over filling while pouring the PDMS. The measured dimensions of the samples are summarized in Table 3.1.

Table 3.1: Measured dimensions for the tensile and compressive test samples

	No acetone bath			Acetone bath		
Tensile test	Sample 1	Sample 2	Sample 3	Sample 1	Sample 2	Sample 3
Width (mm)	14.84	14.82	14.54	14.68	14.66	14.66
Depth (mm)	5.52	5.54	5.32	5.56	5.56	5.40
A in (mm^2)	81.92	82.21	77.35	81.62	81.51	79.16
Compressive test	Sample 1	Sample 2	Sample 3	Sample 1	Sample 2	Sample 3
Height (mm)	9.89	9.94	9.96	10.18	10.30	10.07
Diameter (mm)	9.09	9.23	9.17	9.53	9.45	9.37
A in (mm^2)	64.89	66.91	66.04	71.33	70.14	68.95

For the tensile test, the samples are clamped at each end, with the clamps separated by $L = 50$ mm. An Instron 3369 with a 30 kN load cell [110] is used to perform the test, with a velocity of 50 mm/min. Although this value is high for mechanical testing, it is consistent with the testing methodology found in literature review (see Section 2.2.1). The high velocity is due to the mechanical properties of soft polymers. The results of the experiment is shown in Figure 3.12:

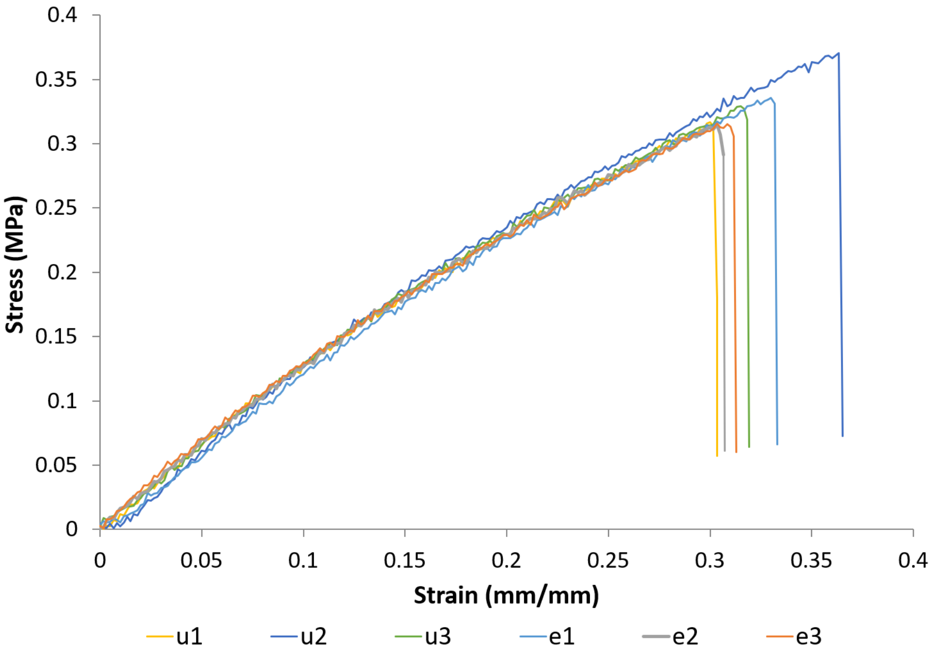

Figure 3.12: Stress-Strain graph of the tensile experiments, combining the data from the samples exposed to acetone (ex) and unexposed (ux).

The data shows no discernible difference between the samples processed through the acetone bath and the unexposed samples. The mechanical properties of PDMS under tensile load do not seem to be affected by the time spent in acetone, at least up to 72 hours. For the compressive test the samples are placed between two plates and the load is applied. Due to availability, the Instron machine is replaced by a ESM303 from MARK-10 [111] with 1.5 kN load cell, with the velocity set at 13 mm/min. This value is lower than the velocity used for the elongation testing in order to prevent the barrelling effect and give accurate numbers (see Section 2.2.1). Because of the properties of PDMS, the software can't detect the point of failure and stop the experiment before it drives the probe into the base, which can damage the load sensor. Therefore, the test is stopped once the load reached 300 N by the control software.

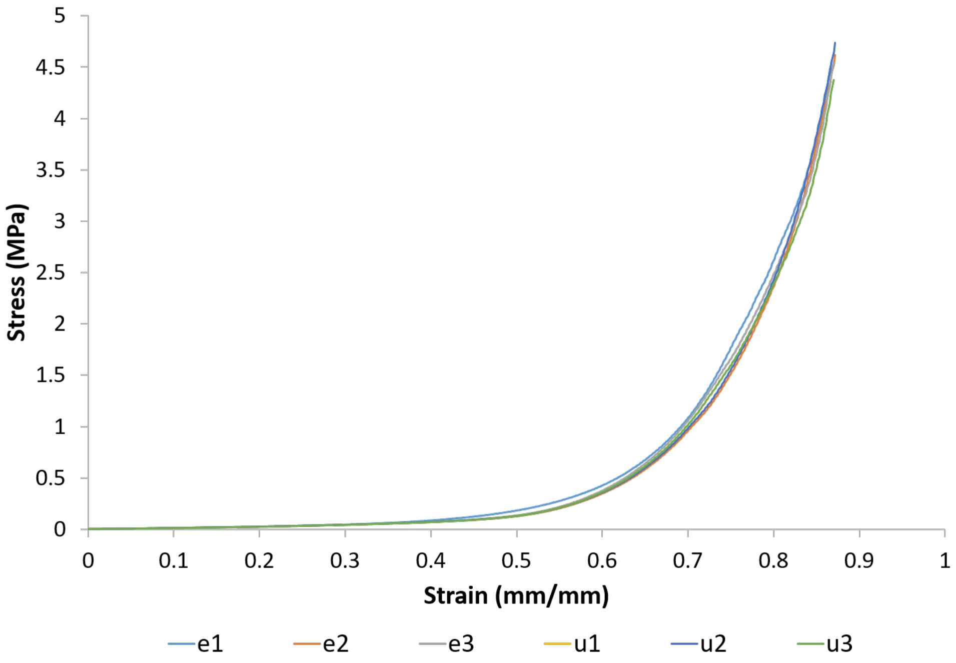

Figure 3.13: Stress-Strain graph of the compressive test, combining the data from the samples exposed to acetone (ex) and unexposed (ux).

Similarly to the tensile test results, the acetone bath does not seem to affect the mechanical properties of PDMS under compressive load. Using the data from the tensile test, the Young's modulus is calculated. The Young's modulus is used to quantify the stiffness of a material. It is defined by the ratio between the tensile stress applied to a sample and the strain, i.e. the elongation of the sample over its initial length, as described with the following equation:

$$E = \frac{\sigma}{\epsilon} = \frac{F/A}{\Delta l/L} \tag{3.1}$$

where:

E : Young's modulus (Pa)

σ : stress (Pa)

ϵ : strain (dimensionless ratio)

F : tensile force (N)

A : cross section (m^2)

Δl : elongation (m)

L : length (m)

Table 3.2: Calculated Young's modulus for each samples

	Sample 1	Sample 2	Sample 3	Mean (SD)
No acetone bath (MPa)	1.18	1.20	1.19	1.19(±0.01)
Acetone bath (MPa)	1.14	1.18	1.19	1.17(±0.03)

Table 3.2 shows the Young's modulus for each sample. We can observe that the Young's modulus is similar between the samples which were subject to the acetone bath and the unexposed samples. This indicates that the stiffness of PDMS is unaffected by being exposed to acetone for up to 72 hours. The calculated Young's modulus is comparable to previous study with similar curing time, curing temperatures and monomer/curing agent ratios. A Young's modulus of 1.72 MPa for PDMS with a 10:1 ratio, cured at 65°C for 12 hours, was similarly found by R.N. Palchesko *et al.* [70]. For comparison, the Young's modulus given by the manufacturer of Sylgard 184, Dow Corning, is higher, 6.7 MPa [86] compared to 1.19 MPa calculated from this experiment, although the curing conditions of the commercial test samples are not provided.

3.6 Summary

This chapter has demonstrated the manufacturing process to create three-dimensional fluidic devices using the lost-core method and each step of the procedure was explained in detail. Design guidelines were summarized, to ensure the device can be manufactured. The minimum diameter for a channel was established to be 1 mm for the Stratasys µPrint SE [105], smaller features are unlikely to be manufactured with a guaranteed success and will be damaged during the acetone smoothing process. Small, narrow features should be avoided and upside down voids will likely trap air while pouring PDMS, making the device unusable. Each section of the manufacturing process explained the design and printing process, how to reliably perform the acetone smoothing procedure and finally the removal of the ABS using the acetone bath, as well as how to safely flush the swollen device.

Using tensile and compressive test experiments, the mechanical properties (Young's modulus) of PDMS samples, before and after being left in acetone for 72 hours, were compared and they were found to be similar. The Young's modulus of PDMS was calculated. For the samples placed in the acetone, the average Young's modulus was 1.17 ± 0.3 MPa while the average Young's modulus for the unexposed samples was 1.19 ± 0.1 MPa.

Chapter 4

Design and Characterisation of 3D Fluidic Components: Creating Functional Blocks for Complex Fluidic Devices

4.1 Introduction

Electronic devices are manufactured by putting together individual components. Resistors, sensors, transistors, etc. are selected based on characteristics given by the manufacturer. By understanding their behaviour beforehand, complex circuits can be created without having to test and characterise every single component, saving a considerable amount of time. This chapter is presenting a similar approach for the design of fluidic devices. Functional blocks, each performing an individual task (sensors, proportional valves, etc.) are designed and characterised. Each of those functional blocks are manufactured using the process developed in Chapter 3. The objective of this design approach is to be able create a complex 3D fluidic device without having to characterise it.

4.2 Inlet and outlet ports

Ports are essential for a fluidic device, as they allow for connection to external components such as pumps or containers. The connection should be reliable, easy to implement and manufactured using the process presented in Chapter 3.

The design of the port consists of a 1.5 mm diameter channel leading to the inlet/outlet, ending with a truncated cone shaped volume. The initial diameter of the truncated cone is 4 mm and a final diameter is 5 mm, with a length of 7 mm (engineering drawing available in Appendix B). The port is designed to connect a 4 mm outer diameter silicone tube to a fluidic device, see Figure 4.1.

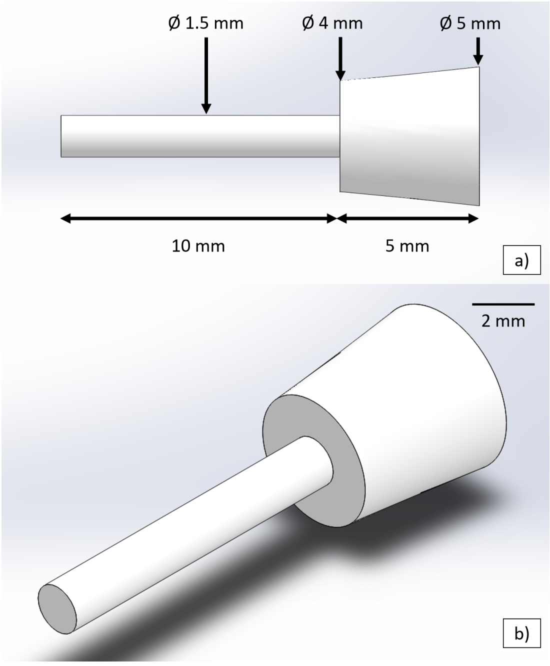

Figure 4.1: CAD representation of a port designed to connect 4 mm outer diameter tube. a) Shows the dimensions of the port. b) Shows a 3D representation

Sil-Poxy [112], a highly viscous silicone glue, is used to bond the silicone tube to the fluidic device. The high viscosity of the silicone glue compared to PDMS (600 Poise vs. 35 Poise for PDMS) prevents it from spreading into the fluidic channel, stopping any possibility of restricting or blocking the flow. Additionally, the high viscosity stops the silicone glue from spilling out of the port while it sets, simplifying the manufacture of the fluidic device. The silicone glue cures into a soft compliant material, similarly to the PDMS and the silicone tube it binds together, reducing the possibility of the glue detaching from either the fluidic device or the silicone tube. The port is designed as a cone so that the silicone tube can easily fit into the port, as well as ensuring enough silicone glue is present to create a strong bond between the silicone tube and the fluidic device. This design provides a stable and reliable connection. Figure 4.2 shows the port as a functional block.

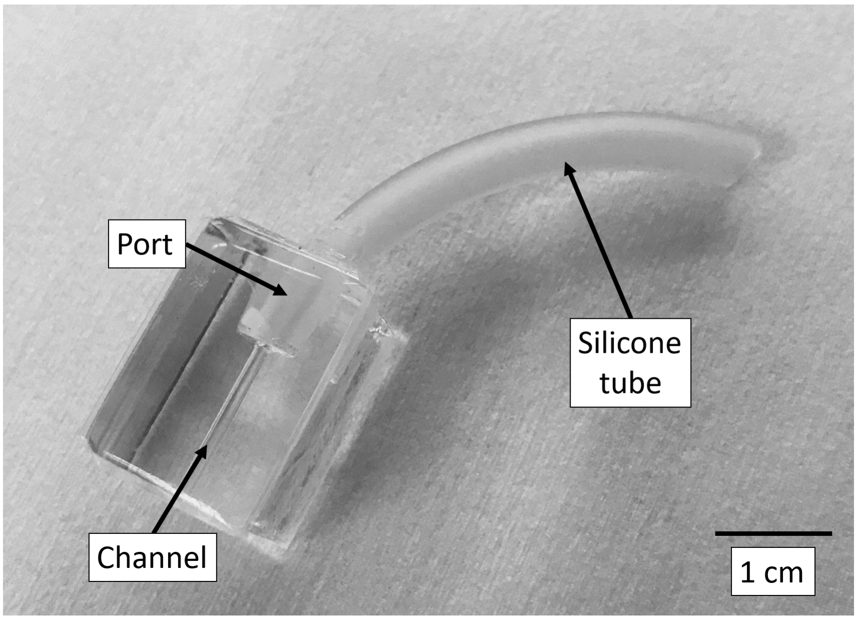

Figure 4.2: Functional block of the 4 mm port

4.3 Reservoir

The 3D process described in Chapter 3 allows for the design of large reservoirs, reducing the number of connections to external components. The design of the reservoir is simple and consists of a cylinder of a diameter of 25 mm and a height of 20 mm, with a 1.5 mm channel at the bottom, for a maximum volume of 9.8 ml. The CAD model of the cylinder is hollow, to save on material, with a 1 mm thick wall. Figure 4.3 shows a CAD view of the reservoir.

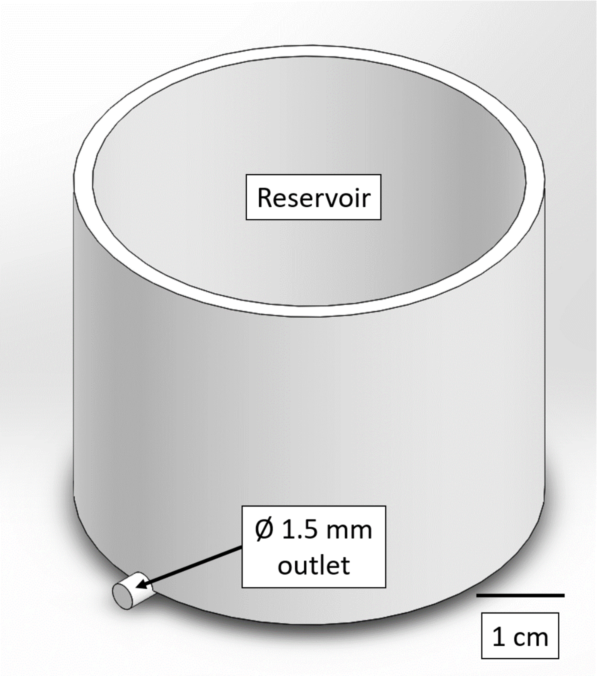

Figure 4.3: CAD representation of the reservoir functional block

Figure 4.4 shows two different views of a reservoir used in a fluidic device.

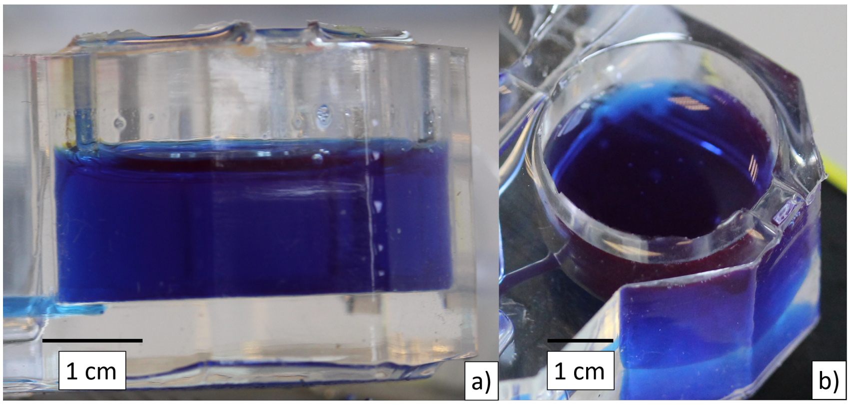

Figure 4.4: Reservoir used in a fluidic device. a) Cross-section of the reservoir through the PDMS, outline by the blue dye present in the reservoir. The outlet is visible at the bottom left. b) View of the reservoir filled with dyed water

4.4 Chaotic flow mixer

4.4.1 Design of the mixing module

The design of the mixing module consists of a channel with flattened profile, with a 1.5 mm diameter input/output. To help induce turbulence and improve the mixing efficiency, the profile changes from the circular input/output to a vesica piscis shape (two intersecting circles), 3 mm high and 0.8 mm wide. The vesica piscis shaped section is 5 mm long, with an additional 3 mm on each side, used to connect the module to a to 1.5 mm circular channel. Figure 4.5 a) shows the CAD of the mixing module with dimensions, with Figure 4.5 b) showing an overall view of the mixing module.

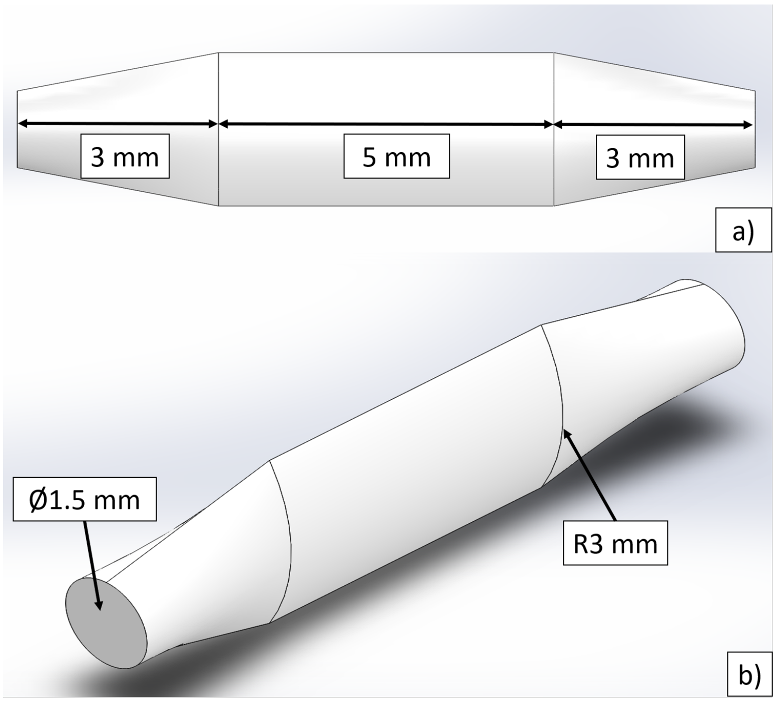

Figure 4.5: CAD representation of the mixing module, showing a) the length of each sections and b) the diameters of each sections

To determine if turbulent flow is generated, which would validate the design of the mixer, the Reynolds number is calculated. If $Re \leq 2300$ then the flow is laminar. If

$2300 < Re < 4000$, the flow is transient. Finally, if $Re \geq 4000$, then the flow is fully turbulent. The Reynolds number is calculated using the following equation:

$$Re = \frac{\rho\, v\, D_H}{\mu} \tag{4.1}$$

where:

- Re : Reynolds number (dimensionless)
- ρ : Water density (kg/m^3)
- v : Velocity (m/s)
- D_H : Hydraulic diameter (m)
- μ : Water dynamic viscosity (Pa.s)

D_H is calculated with the following equation:

$$D_H = \frac{4\, A}{P} \tag{4.2}$$

where:

- D_H : Hydraulic diameter (m)
- A : Cross section area (m^2)
- P : Wet perimeter (m)

The velocity in the mixing module is calculated with the following equation:

$$\overline{v} = \frac{\dot{Q}}{A} \tag{4.3}$$

where:

- $\bar{v}$: Mean velocity (m/s)
- $\dot{Q}$: Volumetric flow rate (m^3/s)
- A : Cross section area (m^2)

The following parameters were used to calculate the Reynolds number:

- The density of water, ρ, is $997\,\mathrm{kg/m^3}$ at 25 °C.
- The dynamic viscosity of water, μ, is $8.9 \times 10^{-4}\,\mathrm{Pa\,s}$ at 25 °C.
- The flow rate was determined via experiment with the peristaltic pump used in Section 5.3.3. The measured flow rate was $4.67\,\mathrm{mL/s}$.
- The perimeter, P, which was measured in SolidWorks, is $6.28 \times 10^{-3}\,\mathrm{mm}$.
- The cross section area, A, measured in SolidWorks, is $1.63 \times 10^{-3}\,\mathrm{mm}^2$.

Therefore:

$$D_H = \frac{4\,A}{P} = \frac{4 \times 1.63 \times 10^{-3}}{6.28 \times 10^{-3}} = 1.04 \times 10^{-3}\,\mathrm{m} \tag{4.4}$$

Then, the mean velocity is calculated:

$$\bar{v} = \frac{\dot{Q}}{A} = \frac{4.67 \times 10^{-3} \times 997}{1.63 \times 10^{-3}} = 2.88\,\mathrm{m/s} \tag{4.5}$$

Finally, the Reynolds number can be calculated:

$$Re = \frac{\rho\, v\, D_H}{\mu} = \frac{997 \times 2.88 \times 1.04 \times 10^{-3}}{8.9 \times 10^{-4}} = 3355 \tag{4.6}$$

With a Reynolds number under 4000, the flow is therefore transient. The mixer is designed to create turbulences, via change in cross section area. Because the calculations of the Reynolds number do not take into account the design, a verification via CFD simulation is necessary. The design is exported to StarCCM+ 12 as an IGES file. The mesh is generated with the following parameters:

- Surface wrapper
- Surface remesher
- Prim layer remesher
- Tetrahedral
- Base size of 0.1 mm
- Prism layer thickness of 0.1 mm

The mesh consists of 44,906 cells. Next the physics setting need to be specified. The mixer is expected to incur turbulent flow, therefore the parameters are:

- Three dimensional
- Steady
- Liquid
- Segregated flow
- Constant density
- Turbulent

- k-epsilon model

The boundary conditions are “Mass flow inlet”’ for the inlet, set at 4.66×10^{-3} kg/s (same value used to calculated the Reynolds number) and “Pressure outlet” for the outlet. The simulation is now configured and ready to start. Verifying if the simulation converged is done by monitoring the residuals. The residuals express the difference between the model’s variables calculated during one iteration and the previous one. The simulation is considered converged if the residuals are lower than 1×10^{-3}. Running the simulation for longer to decrease the residuals only increases the computing time while not improving the accuracy in a meaningful way. After the simulation stopped, the residuals remained higher than the threshold, indicating the model cannot be solved i.e. the flow is not turbulent. Therefore the simulation was modified to use a laminar model, with the following settings:

- Three dimensional
- Steady
- Liquid
- Segregated flow
- Constant density
- Laminar

After 120 iterations, the residuals reached values lower than 1×10^{-3}, indicating that the simulation converged. Figure 4.6 shows the velocity field across the mixing module:

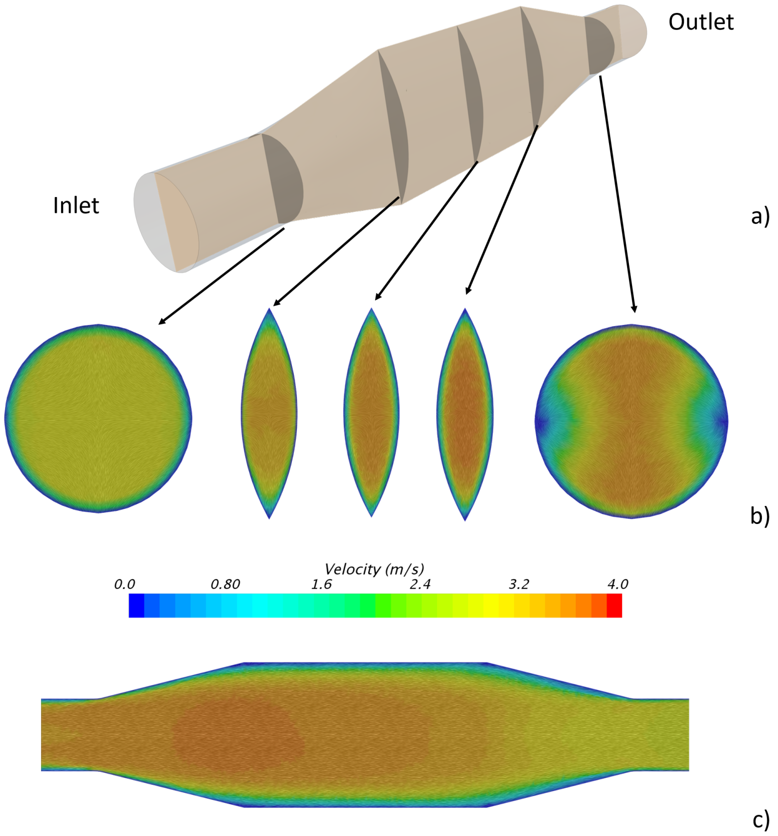

Figure 4.6: Scene showing the results of the simulation. a) represents the geometry of the mixing module, showing the location of the cross sections. b) shows the velocity profile along the mixing module, perpendicular to the flow. c) shows the velocity profile in the mixing module, axial to the flow. No vortices are present, indicating that no turbulent flow is present, mixing is unlikely to occur within the short distance of the mixing module

The stimulation shows that the design does not create turbulences under the specified conditions. No vertices are present, a sign of turbulences, therefore mixing is unlikely to occur along the short length of the module.

Figure 4.7 shows a configuration designed to improve the mixing. To ensure the fluids are thoroughly mixed when leaving the mixer, 6 mixing modules are combined to create the full mixer block. The modules are arranged vertically and tightly packed to keep the space usage to a minimum. Each module is connected to the next via a 1.5 mm channel, creating a 180 ° bend for the flow. The overall dimension of the block is 11 mm long, 7 mm wide and 15.5 mm tall.

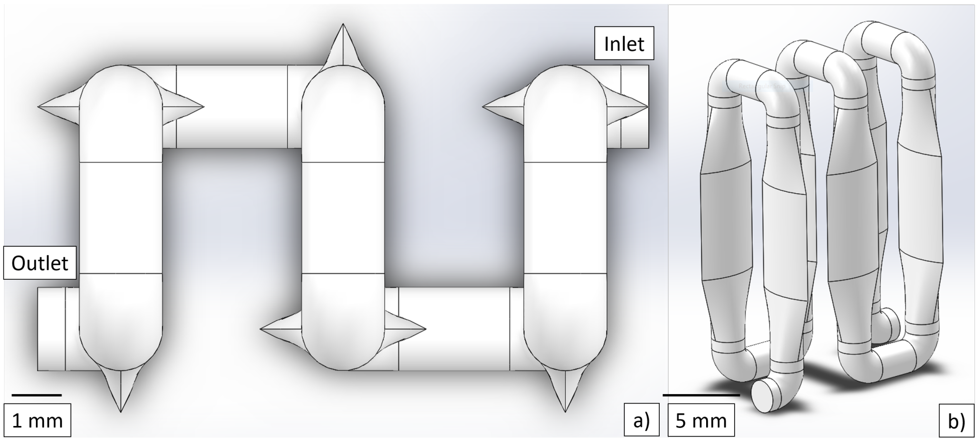

Figure 4.7: CAD representation of the mixer block. a) shows a top view, with the inlet an outlet. b) shows a general view of the design

A CFD simulation is also necessary to evaluate the mixer block design. The same parameters for Mesh, Physics and Boundaries used for the simulation of the module are applied for the simulation of the mixer block. Due to the larger design, the number of cells in the mesh increased to 386,973. The simulation satisfied the convergence criteria after 1250 iterations (i.e. the residuals reached values lower than 1×10^{-3}). Figure 4.8 show the location of the cross sections used to display the results of the simulation. A front and back view, cutting through the middle of the first and second row of mixer modules, axial to the flow as well as a top view, cutting through the middle place of the mixer block, perpendicular to the flow, are visible.

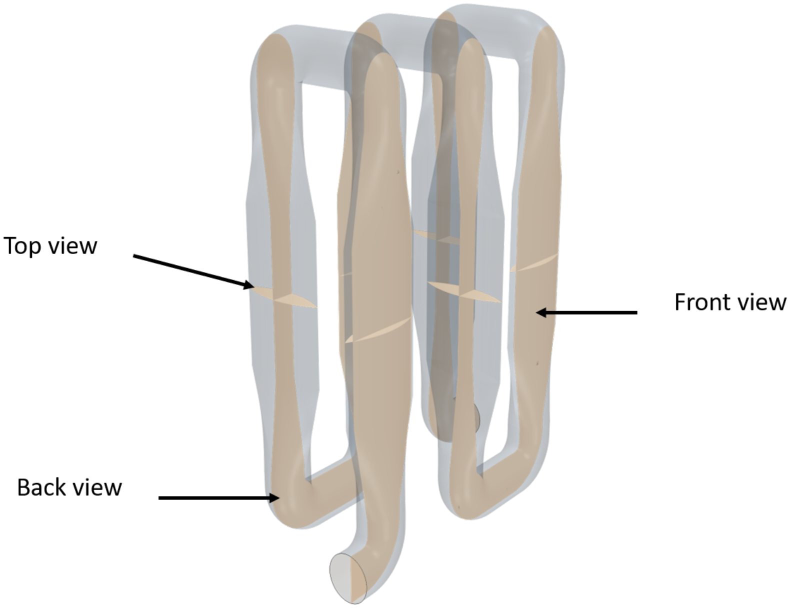

Figure 4.8: The figure shows where the cross sections are located in the mixer block. The front cross section runs though the middle of the first row of mixer modules while the back cross section runs through middle of the second row of modules, both axial to the flow. The top cross section runs through the middle of the mixer modules, perpendicular to the flow direction

Figure 4.9 shows the velocity, as well as the flow streamlines, through a side cross section of the mixer block. Figure 4.9 a) shows the velocity filed of the front view, while Figure 4.9 b) represents the flow in the back cross section.

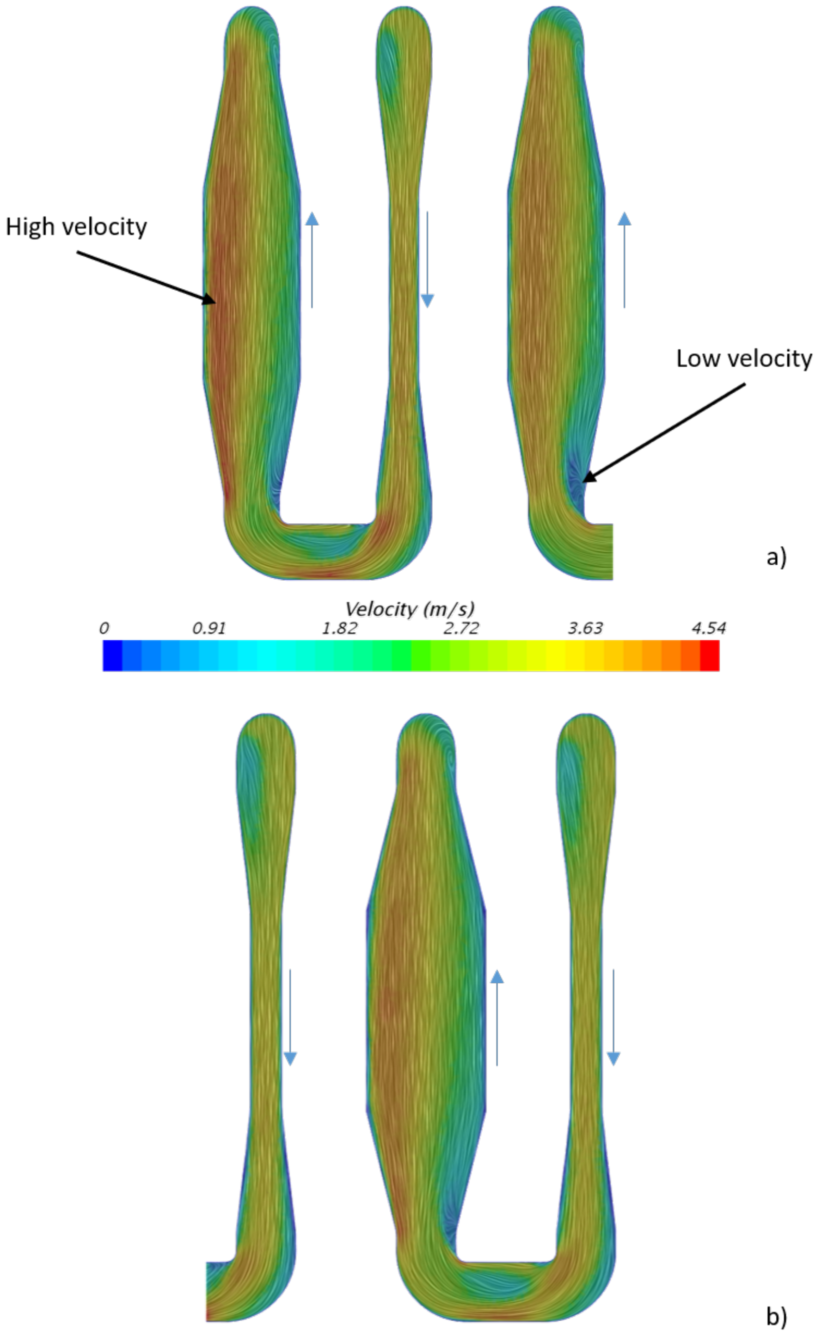

Figure 4.9: Scene showing the results from the simulation expressed in terms of velocity. a) Velocity in the front cross section. b) Velocity in the back cross section. The blue arrows indicate the flow direction. No vorticity are visible but the velocity map shows that the flow is clearly not laminar. The velocity across the mixing modules is not consistent, with higher velocities visible left of the flow direction

Figure 4.10 shows the velocity and the streamlines in the top cross section view of the mixer block.

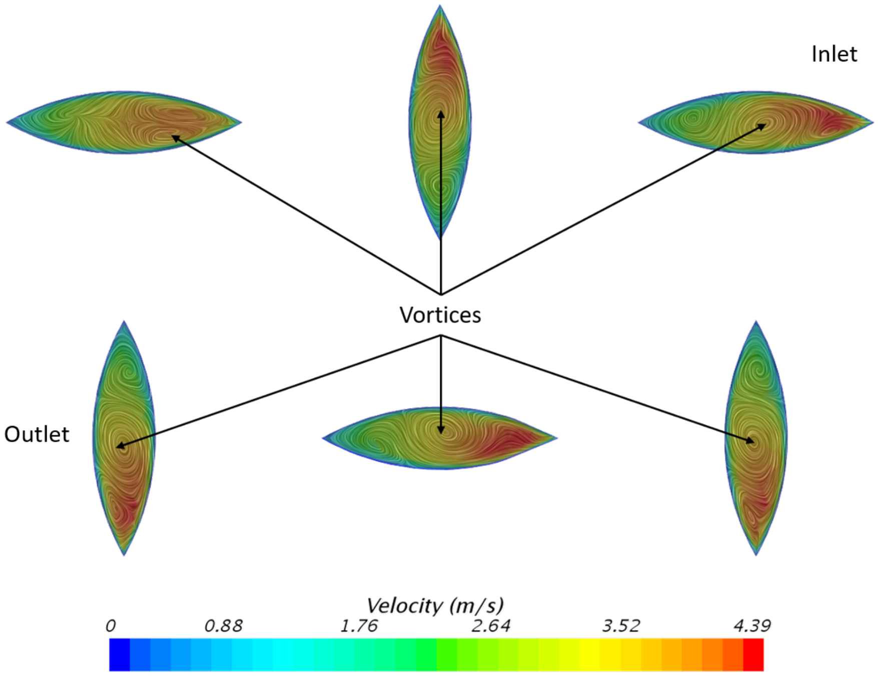

Figure 4.10: Scene showing the velocity filed in the top cross section view. Multiple vortices are clearly present in every part of the mixing block, an evidence of turbulent flow

The results of the simulation show a high number of vortices present in the mixing modules, a strong evidence of a turbulent flow. As much as 3 vortices are present in some of the section, arranged along the larger dimension of the mixing module. The vortices are axial to the flow and the maximum velocity displayed in the cross section reaches a value of 4.39 m/s nearly doubling the mean value V = 2.88 m/s, calculated to determine the Reynolds number of the mixing module. The simulation demonstrates the turbulent nature of the flow in the mixer block, generated by the arrangement of the modules. While each module on their own is not enough to generate a turbulent flow, the stacking of 6 modules as well as the 90 ° used to connect the modules is enough to generate the turbulent flow.

4.5 Proportional pneumatic valve

4.5.1 Design of the proportional valve

The design of the valve is dictated by the following requirements:

- The design should accommodate the manufacturing process from Chapter 3.
- The valve should be capable of controlling a wide range of flow i.e. be proportional. This is to allow a greater control of the flow through a fluidic device. The valve should also be capable of performing ON/OFF operations.
- The valve could be implemented in a 3D space, anywhere within a fluidic device, therefore the use of hard surface for the actuation is not possible.

The design of the pneumatic valve is similar to the “Quake” valve [45]. This design is chosen because of the simplicity and it requires no moving parts. Figure 4.11 shows a graphical representation of the working principle of the “Quake” valve. The valve consists of 3 parts: a solid substrate, a fluidic layer and a control layer. The flow in the fluidic layer is controlled by applying a pressure inside the control layer, using compressed air. With the pressure difference, the layer of PDMS makes the roof of the fluidic channel expand in the fluidic channel, obstructing the flow. Further, increasing the pressure will block the flow entirely. Since the pneumatic valve presented in this work should be able to be placed anywhere in a fluidic device, the reliance on a hard surface for actuation is not possible.

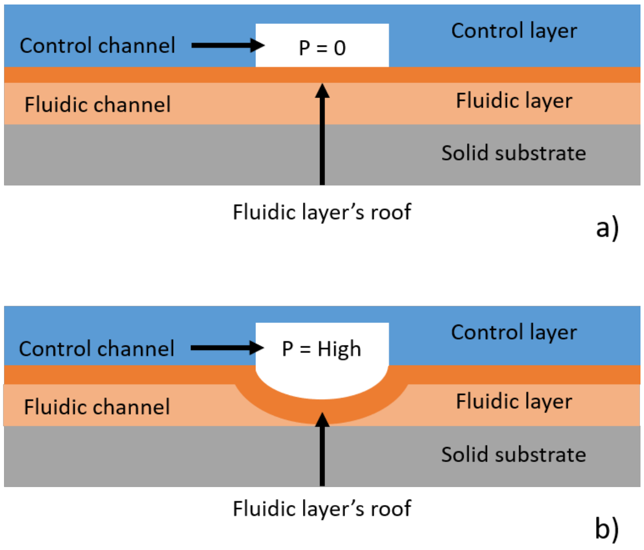

Figure 4.11: Graphical representation of the "Quake" valve. a) Valve in its open state. The pressure in the control layer is low, the fluidic layer's roof, is at its rest position and the fluidic channel is open. b) Valve in its closed state. The pressure in the logic layer is high, the fluidic layer's rook is stretched and pressing against the substrate, the fluidic channel is obstructed, stopping the flow

Figure 4.12 shows a CAD view of the pneumatic proportional valve design. The pneumatic valve consists of 2 parts. A fluidic channel, or fluidic layer, with an elongated profile to promote the collapse of the channel ensuring full blockage of the flow, with a length of 10 mm and a cross section of 0.8 mm by 3 mm. Each ends merges from the middle section to a circular channel with a diameter of 1.5 mm. The shape is similar to the design of the mixing modules, see Section 4.4. On each side of the fluidic channel are two semi-circular pressure chambers, acting as the control layer. The shape of the pressure chamber is designed to ensure the force is primarily directed towards the fluidic channel. The chambers have a 5 mm diameter, with the planar side facing the channel, and are 10 mm long. A 1.5 mm channel connects both chambers to a single port to control the pressure inside the chambers. A second port is used to flush the chambers of liquefied ABS before being sealed with Sil-Poxy. The valve is designed to be easily flushed. The acetone can be pumped through one of the two ports. The flow of acetone crosses the entire first chamber before flowing through the connecting channel into the second chamber. It then flows through the second chamber and leaves the device by the second port. Figure 4.12 a) shows a CAD view of the design while Figure 4.12 b) shows the device used for testing.

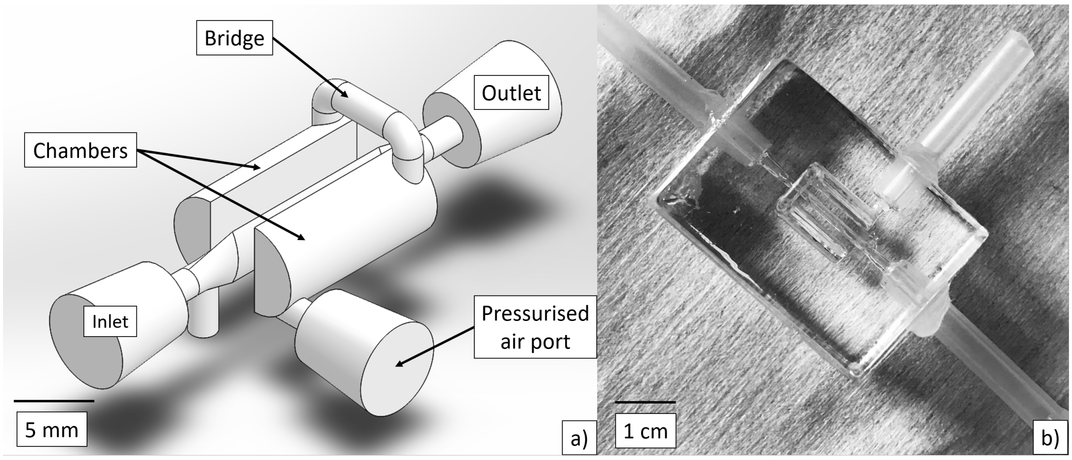

Figure 4.12: a) CAD representation of the proportional valve design and b) fabricated proportional valve used for the testing of the design

4.5.2 Characterization of the proportional valve

A container of water, placed 1 m above the device thus creating a head pressure of 100 mbar, is connected to the fluidic device's inlet via a 4 mm (inner diameter) silicone tube. The outlet tube is blocked with a clamp to stop any flow through the fluidic device. To calculate the mass flow rate, the pneumatic valve is pressurised to a fixed value, adjusted with the combination of a small air pump and a pressure sensor, the clamp is removed, and the water flowing through the device is collected into a beaker. The clamp is placed back after a predetermined period of time and the weight of water is measured. With the mass of water measured, the mass flow rate can be calculated. Starting at atmospheric pressure, the pressure in the pneumatic valve is increased by increments of 17 mbar (the resolution of the pressure sensor) for each mass flow measurement, until the flow is completely stopped. To keep the measurements accurate, by collecting a sufficient mass of water in the beaker, the amount of time the clamp is removed increases with the pressure in the pneumatic valve, from 15 s to 120 s. This is to compensate for the reduced flow rate out of the pneumatic valve. The experiment was repeated 3 times and a mean value was calculated, as well as the standard deviation (see Appendix C).

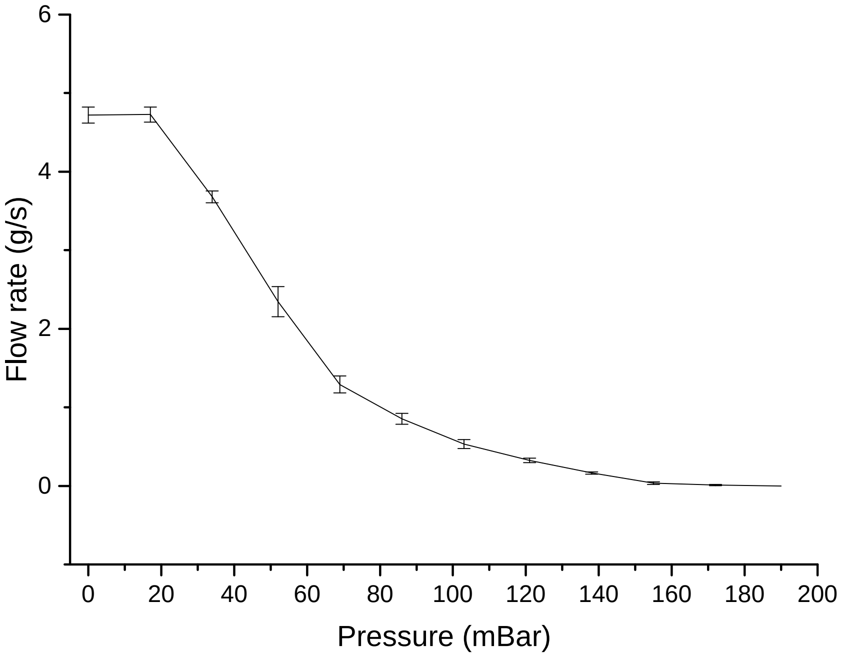

Figure 4.13: Plot showing the relationship between the mass flow rate of water and the pressure inside the proportional valve. The mass flow rate decreases as the pressure in the pneumatic valve is increased. At 190 mbar, the flow is stopped, indicating that the pneumatic valve is fully shut. Mean of 3 reading, 1SD

Figure 4.13 summarizes the results from the experiment, showing the relation between the valve pressure and the water flow rate. At first, a small increase in pressure, from 0 to 17 mbar, has no effect on the flow rate. Then a further increase in pressure dramatically affects the flow rate, dropping from 4.72 ±0.10 g/s down to 3.68 ±0.06 g/s. Further increase in pressure yields a comparable drop in flow rate, up to 70 mbar. Additional pressure increases have a reduced effect on the flow rate as the valve is approaching its closed state. After the pressure has reached 155 mbar, the flow is severely restricted, now less than 1 % of its original value. The valve is fully shut with a pressure of 190 mbar.

Finally, since the head pressure of the water is 100 mbar, the 90 mbar difference is the pressure necessary to deform the PDMS and close the valve. Therefore, the pressure necessary to close the valve at under any flow conditions should be the sum of the pressure due to the flow in the fluidic channel plus 90 mbar.

4.6 Photometric sensor

Michaelis–Menten enzyme kinetics analysis is used as a practical example of an experiment requiring such a sensor. The focus is on the development of a photometric sensor that can record the change of absorbance as the enzyme-catalyzed reaction occurs. The reaction of the colourless p-nitrophenyl phosphate with an alkaline phosphatase creates p-nitrophenol, a yellow by-product. This is used to implement the sensor. The reason for choosing this particular reaction is the speed at which it happens, typically within minutes, making the iterative development easier [113, 114].

The design of the sensor is guided by the following requirements:

- The sensor design should realise the manufacturing process design in Chapter 3
- The sensor should be optimised for the detection of p-nitrophenol
- The sensor needs to produce its light source

- The light source and light detector should be set apart at a constant distance with no material present in the light path other than the sample to be studied
- The sensor should be protected from surrounding disturbances

4.6.1 Working principle

The photometric sensor functions by relying on the change in light absorption of the fluid present in a analysis chamber, either due to a chemical reaction taking place in the analysis chamber (intermittent flow) or the fluid flowing with a changing concentration of an absorber, achieved with the proportional valve described in Section 4.5 (continuous flow). A LED is placed on one side of the channel and a phototransistor, or PT, on the opposite side. The LED would emit light through the analysis chamber, which would be received by the PT. Figure 4.14 shows the circuit of the PT. Phototransistors vary the amount of current they let through with changing light intensity [115]. The more light received, the more current they let through. If the current increases, the voltage drop across the resistor would be increased as well. By measuring the voltage across the PT, the light intensity can be measured. The amount of light received by the PT will depend on the absorbance of the fluid present in the channel. Therefore, the concentration of a light absorbing substance present in the fluid can be correlated to the voltage across the PT.

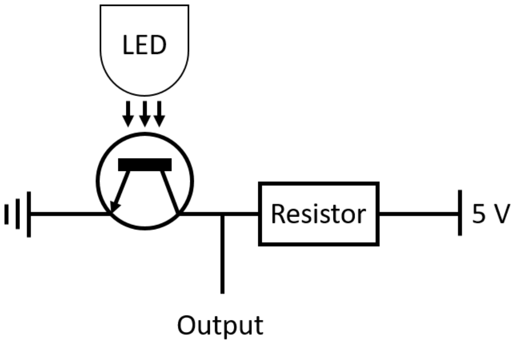

Figure 4.14: Schematic representation of the PT circuit

4.6.2 Design of the photometric sensor

Ideally, the entire fluidic device would be manufactured using dyed PDMS, to block any light leakage. Unfortunately, this would cause problems during the manufacturing of the fluidic device. While flushing the liquefied ABS, some could remain inside the channels and affect the flow or the operation of the components. Furthermore, if the device is opaque, potential problems would be hidden and this could slow the development process.

Figure 4.15 shows a CAD view of the mould design for the photometric sensor:

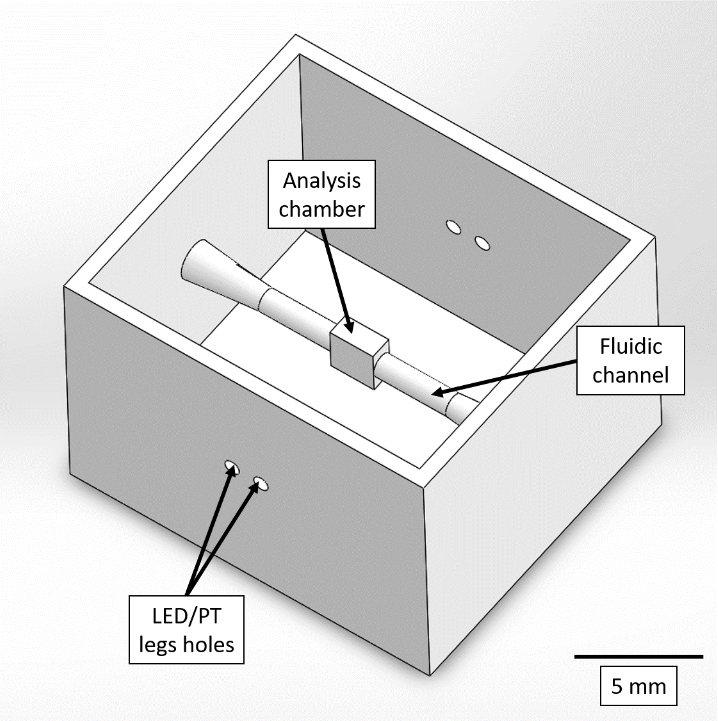

Figure 4.15: CAD representation for the mould of the photometric sensor block

The negative mould of the photometric sensor consists of a 1.5 mm channel, with a 3 mm by 3 mm by 1.5 mm analysis chamber, where a 3 mm package LED and 3 mm package PT are attached to the analysis chamber with superglue (Cyanoacrylate adhesive). Both the LED and PT are wrapped in heat-shrink tubing (a thermoplastic that shrinks radially when heat is applied [116]) before being attached to the negative mould. The analysis chamber with the heat shrink allows the LED and PT to be more precisely positioned. The small windows created by the heat-shrink tubing allows for a quasi flat surface, reducing the quantities of glue necessary to attach the components to the channel, and preventing the creation of an unwanted void, as superglue is soluble in acetone. The final step is to surround the LED, PT and analysis chamber with dyed PDMS. Before PMDS is poured in the mould, PDMS dyed with Silc Pig blue silicone pigment [117] is applied with a pipette around the analysis chamber. Due to gravity and longer curing time at 60°C, the PDMS moved to the underside of the analysis chamber before it cured. Therefore, a second application is necessary, with the mould held upside down. Once the dyed PDMS had covered the entire analysis chamber and cured, regular PDMS was poured in the mould and cured. This step was necessary to block any surrounding light reaching the PT, which would invalidate the readings from the sensor.

Although PDMS is not sensitive to long exposure to acetone, consideration has to be taken regarding electronic components. LEDs and PTs are usually encased in acrylic and will be damaged by acetone over time [108,109], and should stay no longer than 72 hours in the bath. Once the acetone had evaporated from the device, the area where the pins were protruding out of the device was covered with SilPoxy to seal any possible leaks. Figure 4.15 shows CAD of the photometric sensor functional block. As well as the analysis chamber, two 1 mm holes were added on the walls of the mould for the pins of the components to fit thought, further improving the alignment of the sensor. Figure 4.16 shows the photometric sensor device used for testing:

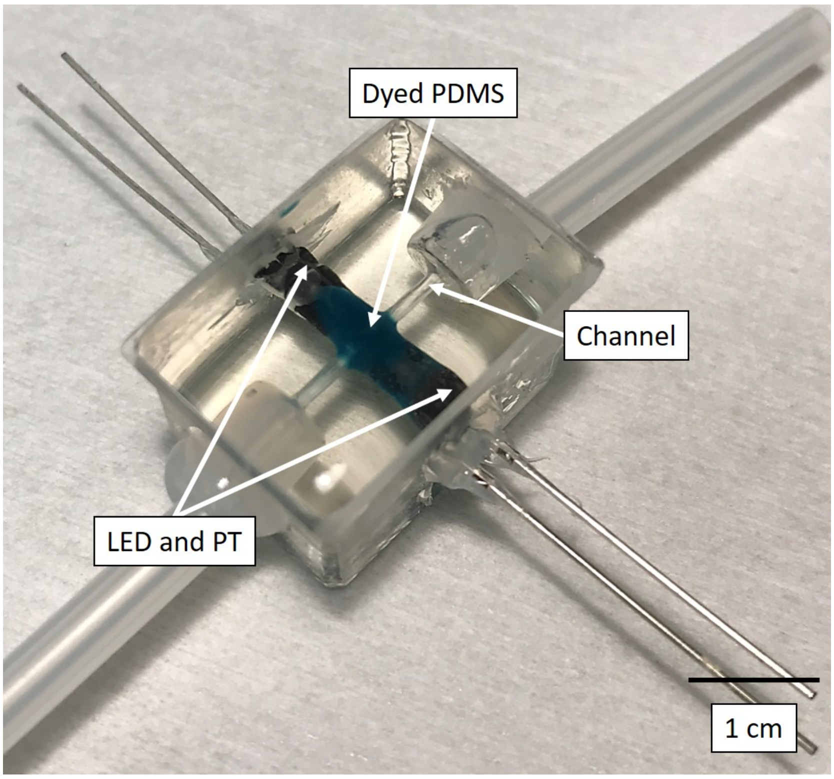

Figure 4.16: Photometric sensor. The LED and PT, protected by the dyed PDMS are visible at the centre of the device

4.6.3 Electronic components for the photometric sensor

p-nitrophenol has a peak absorption of 400 nm [113, 118]. Therefore a 400 nm LED was chosen for the sensor (see Figure 4.18 a), with a luminosity of 350 mcd. With a typical forward voltage of 3.8 V, the LED needed a resistor in series to drop the voltage, connected to a 5 V supply. The calculation of the resistor was done following this equation:

$$R_{LED} = \frac{\Delta_V}{I} \tag{4.7}$$

where:

- R_{LED} : Resistor (Ω)

- $\varDelta_V$: Difference of voltage between the 5 V supply at the typical voltage of the LED (V)
- I : LED typical current (I)

The manufacturer of the LED provided the following data:

- Typical voltage = 3.8 V
- Typical current = 20 mA

Therefore the resistor is:

$$R_{LED} = \frac{\Delta_V}{I} = \frac{5 - 3.8}{0.02} = 60\,\Omega \tag{4.8}$$

Due to unavailability of a 60 Ω resistor at the time, it was swapped for a readily available resistor of 68 Ω. Although the value is not the same, the characterisation of the sensor will show that this has no implication.

The next step is to choose a PT. Unfortunately, UV specific phototransistor in a 3 mm package are not available for purchase. Therefore a visible light sensitive PT, with a non-negligible sensitivity at 400 nm is required. The chosen PT, while not advertised as being UV sensitive, has a sensitivity of around 30 % at 400 nm, see Figure 4.17 a). Figure 4.17 b) shows the spectral sensitivity of a PT advertised a being UV sensitive, yet it has a sensitivity lower than 20 % at 400 nm. Therefore, extra research had to be done when choosing components. The PT was associated with a 10 kΩ resistor, a typical value. Details of the components can be found in Appendix 1.

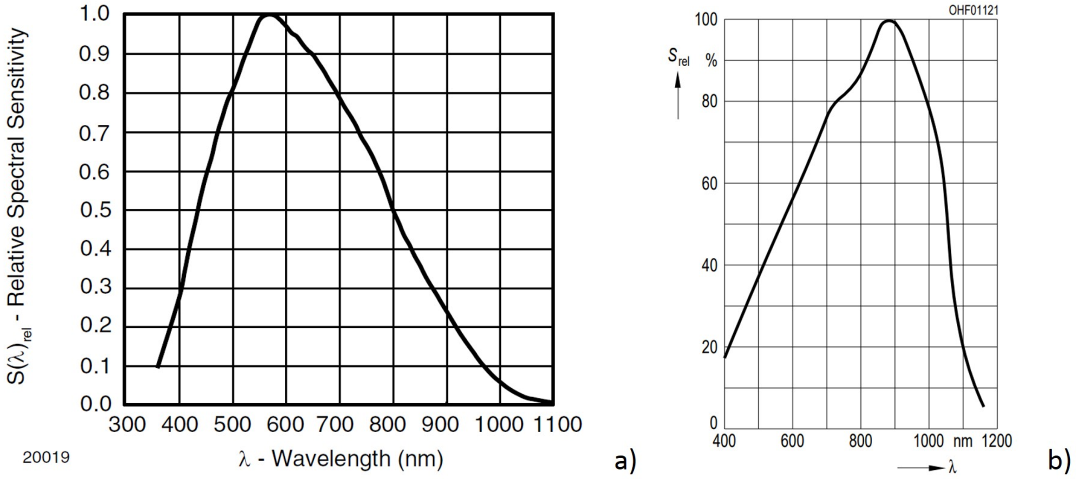

Figure 4.17: Spectral sensitivity of two PT, a) Vishay TEPT4400 [2], advertised as non UV sensitive (used for the photometric sensor) b) Osram SFH 309 [3], advertised as being UV sensitive

4.6.4 Characterization and calibration of the photometric sensor

For the characterisation of the sensor, varying the values for the resistors of both the LED and PT are explored. The aim was to find the most suitable combination of LED and PT resistors for enzyme kinetics. Michaelis–Menten enzyme kinetics studies the velocity of reaction, therefore a sensor with a linear behaviour is crucial. Increasing the resistance associated with the LED reduces the light intensity received by the PT, while increasing the resistance connected to the PT influences the sensitivity of the sensor. Additionally to the 68 Ω resistor, the LED is paired with 4 more resistors of 150 Ω, 220 Ω, 330 Ω and 390 Ω. As per the PT, it is paired with a 10 kΩ, 22 kΩ, a 27 kΩ and a 33 kΩ resistor.

The characterisation was conducted by pipetting a solution of *p*-nitrophenol of varying concentrations inside the analysis chamber of the sensor. The initial concentration was 225 µM, the lower concentration were prepared via double dilution down to 0.879 µM. The voltage was recorded with an Arduino Uno combined with a Matlab GUI, described in Section 5.2.3. A voltage reading was taken every 100 ms for 30 s (3000 data points total). The mean value was then calculated by the Matlab code and displayed to the user, which entered the data in a spread sheet. A simple GUI was designed for the calibration of the photometric sensor. The code run as following:

1. Before the GUI appeared on screen, the code scanned for connected devices and listed them to the user.
2. The user was presented with the GUI seen in Figure 4.18. The first input box let the user choose the COM port associated with the device (usually the only option available). The second input box was used to define the length of the experiment, in seconds.
3. When the “Start” button was pressed, the code read the user’s inputs, communicated with the board and set the pin D2 to 1, allowing the LED to be supplied with 5 V. A loop then started, with the length of the loop set as 10 times the user’s defined experiment length, and read the voltage from the PT on pin A0. The loop then paused for 100 ms minus the time it took to complete. All the readings were stored in a matrix and the mean value of the voltages was calculated once the loop was finished. The resulting value was then displayed in the GUI using a static box.
4. A clear button is available to clear the static box before taking an new reading.

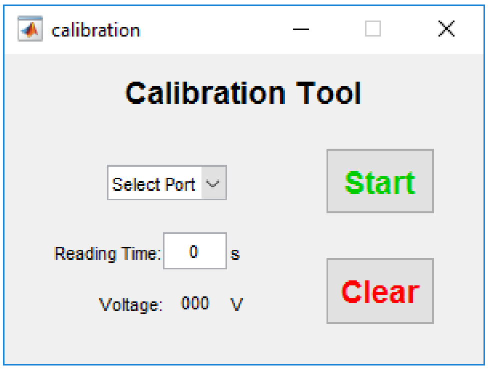

Figure 4.18: Graphical User Interface used to calibrate the photometric sensor

Figure 4.19 displays the results from the characterisation, the data is organised by LED resistor. A few observations can be made:

- With the LED resistor of 68 Ω, the sensor saturated with all the PT resistor at lower concentrations, apart from the 10 kΩ.
- Throughout the test, the 10 kΩ resistor had a poor range compared to the other PT resistors with the same LED resistor.
- Increasing the LED resistor is increasing the voltage output from the sensor but the range remains similar.
- The sensor is behaving more linearly with decreasing LED resistor.

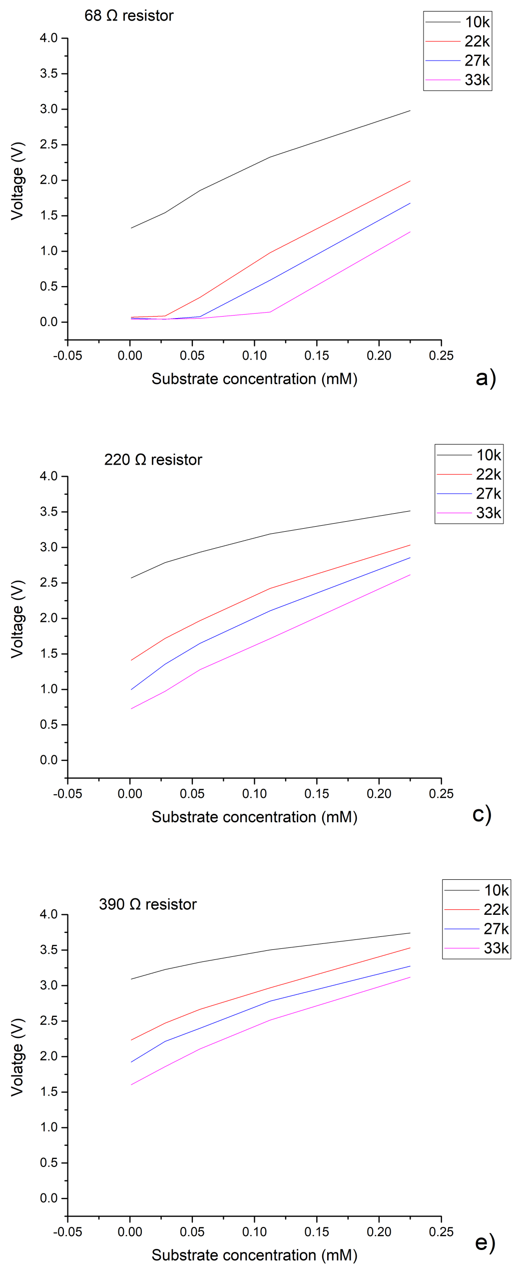

Figure 4.19: Data arranged by LED resistor. The aim of the study is to find the best LED/Pt resistor combination for the sensor to express a linear behaviour at the studied substrate concentration range. a) LED resistor of 68 Ω. All but the 10 kΩ PT resistor show saturation of the sensor at low substrate concentration. b) 150 Ω LED resistor. The combination with a 33 kΩ PT resistor shows a good candidate for a sensor with a linear change in voltage with change of substrate concentration. c) 220 Ω LED resistor. Similar to the 150 Ω LED resistor, the combination with a 33 kΩ PT resistor seem to present a linear behaviour. d) 330 Ω LED resistor. The combination with a 33 kΩ PT resistor shows another candidate for the sensor's final configuration

Based on the characterisation data seen in Figure 4.19, three combination of resistors that appear to express a linear behaviour are chosen: (1) a LED resistor of 150 Ω and an PT resistor of 33 kΩ, (2) a LED resistor of 220 Ω and an PT resistor of 33 kΩ and (3) a LED resistor of 330 Ω and an PT resistor of 33 kΩ. To determine the best candidate, a linear fit analysis is performed using the data from the calibration. Figure 4.20 shows the results:

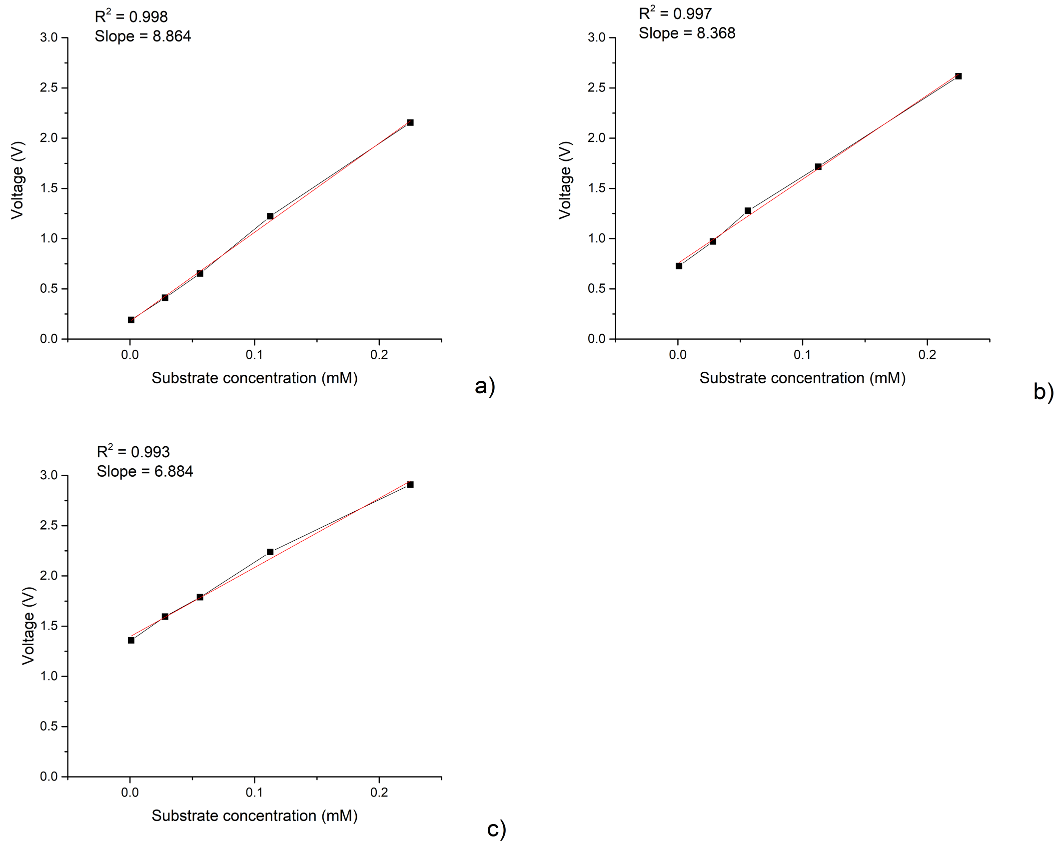

Figure 4.20: Linear fit analysis used to determine the best combination of LED resistor and PT resistor for a linear behaviour. a) Analysis for the 155 Ω LED and 33 kΩ PT resistor, b) Analysis for the 220Ω LED and 33 kΩ PT resistor and c) Analysis for the 330 Ω LED and 33 kΩ PT resistor. With the higher slope of 8.864, equating to the sensitivity of the sensor and a R^2 of 0.998, the combination of the 150 Ω resistor and the 33 kΩ for the PT shows the best linear behaviour

With a R^2 value of 0.998, the combination of a 150 Ω resistor for the LED and a 33 kΩ resistor for the PT shows the best linear fit. Additionally, the slope i.e. the sensitivity of the sensor is the highest for this combination of resistor. Based on those observations, the combination of a 150 Ω LED resistor and a 33 kΩ PT resistor was chosen. This combination expresses a linear behaviour, from 0.879 µM up to 250 µM, a requirement for accurate recording of the velocity of the reaction. Once the combination of resistors was decided, the device needed to be calibrated. The same test used to perform the characterisation of the sensor was conducted 5 times, with additional, intermediate, concentration of *p*-nitrophenol added to verify the linearity of the sensor, and increase the accuracy. The additional concentrations were: 250 µM, 200 µM, 180 µM, 150 µM, 130 µM, 90 µM and 75 µM. Finally a blank reading was taken, filling the channel with a 500 mM Tris, 10 mM $MgCl_2$ buffer with a pH of 8.0.

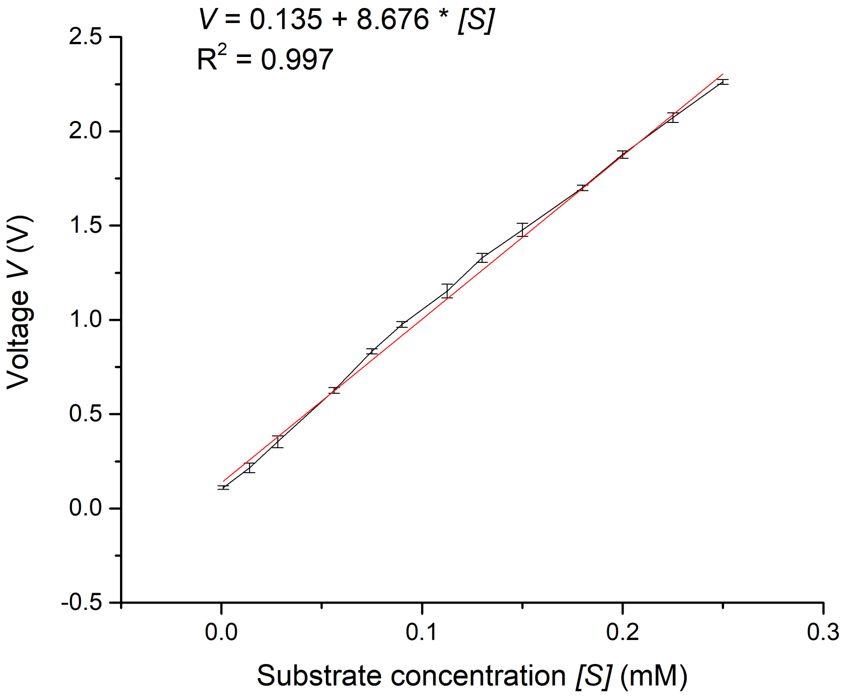

Figure 4.21: Results from photometric sensor showing the voltage changing with the concentration of *p*-nitrophenol. Mean of 5 readings, 1 SD.

Figure 4.21 shows the change of voltage versus the change in concentration of *p*-nitrophenol. The graph shows a clear decrease in voltage when the concentration is reduced. At 250 µM, the voltage is 2.262 V ± 0.013 V when at a 0.879 µM concentration, the voltage is reduced to 0.110 V ± 0.010 V. The sensitivity of the sensor was calculated with Origin via linear fit. This resulted in a sensitivity of 8.68 mV/µmol ± 0.13 mV/µmol with a R^2 of 0.997.

The limit of detection was also calculated:

$$LOD = \overline{x}_b + k\, s_b \tag{4.9}$$

where:

- LOD: Limit of Detection
- $\overline{x}_b$: Mean of blank
- d_b: Standard deviation of blank
- k: coefficient of confidence

The mean blank is $\overline{x}_b = 0.0482$ V with a standard mean blank of d_b 0.00572 V. A coefficient of confidence of 3 is chosen:

$$LOD = \overline{x}_b + k\, s_b = 0.0482 + 3 \times 0.00572 = 0.065V \tag{4.10}$$

The value for the LOD was then fitted against the calibration curve, with a final LOD of 7.5 µM. Therefore, the characteristics of the sensor are:

- Sensitivity of 8.68 mV/µmol ± 0.13 mV/µmol
- LOD of 7.5 µM
- Range of concentration from 7.5 µM to 250 µM

4.7 Summary

This chapter demonstrated the successfully developed 3D functional blocks. Simple but important parts were manufactured and designed, such as a reservoir and ports for easy and reliable connections to external devices. A mixing module was designed and, to improve on the mixing efficiency, a mixer block with six modules was tested, with a vertical arrangement of the mixing modules. Turbulent flow was observed in the mixer block via CFD simulations. The next 3D functional block to be designed was a proportional pneumatic valve. By changing the pressure inside two chambers surrounding a fluidic channel, the flow could be successfully controlled, offering a wide range of flow rates as well as being able to completely stop a flow of water with 100 mbar of head pressure. The last block was a photometric sensor, designed for the study of Michaelis–Menten enzyme kinetics. A UV LED and a UV sensitive PT were placed on opposing sides of an analysis chamber. The components were wrapped in heat-shrink and embedded in dyed PDMS, protecting the sensor from ambient light and ensuring that the only light received by the PT would travel through the analysis chamber. The sensor was characterised and calibrated to ensure maximum range and sensitivity when analysing the concentration of p-nitrophenol. p-nitrophenol is the yellow coloured product of the hydrolysation of the colourless substrate p-nitrophenyl phosphate. Therefore, as the the reaction occurs, the solution gradually changed colour and absorbance. This change in absorbance was used to study the reaction and determine the reaction velocity. By varying the concentration of substrate, the reaction velocity will change, and the enzyme kinetics can be calculated. The sensor was tested with an array of different configurations of resistor for both the PT, varying the voltage drop across the resistor, and the LED, varying the light intensity. The combination of a 150 Ω resistor for the LED and a 33 kΩ resistor for the PT provided the most suitable combination. With this combination, the sensor showed a linear behaviour for concentration of *p*-nitrophenol ranging between 250 mM and 0.88 mM. Additionally, this combination offered a high sensitivity. The photometric sensor was found to have a sensitivity of 8.68 mV/µmol ± 0.13 mV/µmol, with a a *LOD* of 7.5 µM and a range concentration from 7.5 µM to 250 µM. This design is therefore suited to Michaelis–Menten enzyme kinetics.

Chapter 5

Integrated 3D Fluidic Device Case study: Michaelis–Menten Enzyme Kinetics Analysis

5.1 Introduction

This chapter presents the design and fabrication of an integrated fluidic device designed for Michaelis–Menten enzyme kinetics analysis. The fluidic device is designed by the assembly of functional blocks developed in Chapter 4. Each functional blocks is simplified to a schematic form, whereas they are only represented in the form of a basic shape. This is used to simplify the design of complex devices. Only when the design is finalised that the CAD model is produced. Based on the requirement of the system, the suitable functional blocks are chosen and assembled in a schematic design of the fluidic device. This abstract design forms the base of the CAD design. To control the system, an electronic circuit board is designed. The board aims to control the fluidic device by controlling: (1) the flow of liquids through the fluidic layer; (2) the pressure in the proportional valves; (3) operate the photometric sensor and (4) communicate with a host computer for data logging. The Michaelis–Menten enzyme kinetics analysis is performed thorough a Matlab GUI to simplify the process for the user. The performance of the integrated device is then compared to that of a commercial system.

5.2 Design and manufacture of the integrated fluidic device

5.2.1 System requirements

The design of the device for Michaelis–Menten enzyme kinetics analysis should meet the following requirements:

- Use the functional blocks developed in Chapter 4, to reduce the time spent on designing and manufacturing the device.
- The device should be compact, portable and autonomous. This allows the device to be used in any location deemed necessary, without being restricted to a lab where the equipment is located and therefore operate on any fluidic device.
- The device should be low cost, to compete favourably with commercial analysis machines.
- The device should be fully integrated. All the components required to operate the device should be assembled in a single package.
- The device should have an accuracy comparable to that of commercial machines.

5.2.2 Fluidic device design

Figure 5.1 b) shows a schematic view of the design of the fluidic device. The design is using functional blocks, see Figure 5.1 a), developed in Chapter 4.

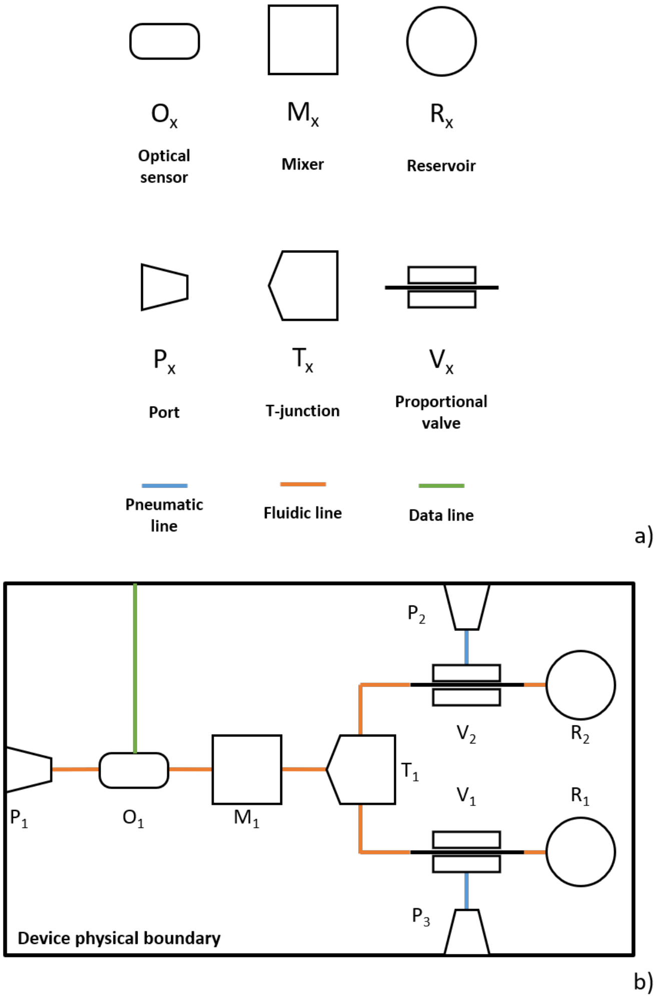

Figure 5.1: Schematic layer of the fluidic device design. a) shows the functional blocks available to deign the fluidic device. b) shows the configuration retained for the fluidic device

The fluidic device consists of: (1) Two reservoirs, used to store the enzyme solution and the substrate solution. (2) Two proportional valves. The valves are used to change the flow rate from the reservoirs, enabling the mixing of the two solution present in the reservoirs with different ratios. (3) A T-junction, where the channels coming from the proportional valves merge. (4) A mixer, ensuring that the two fluids are thoroughly mixed. (5) A photometric sensor, where the enzyme kinetic analysis takes place. (6) An output port where the samples are evacuated out of the fluidic device. (7) Two ports, one for each promotional valve, for the control of the pressure inside the valves' chambers. The port of the fluidic device are connected to the outer components of the system via three 4 mm OD silicone tubes. Figure 5.2 shows a CAD view of the resulting design.

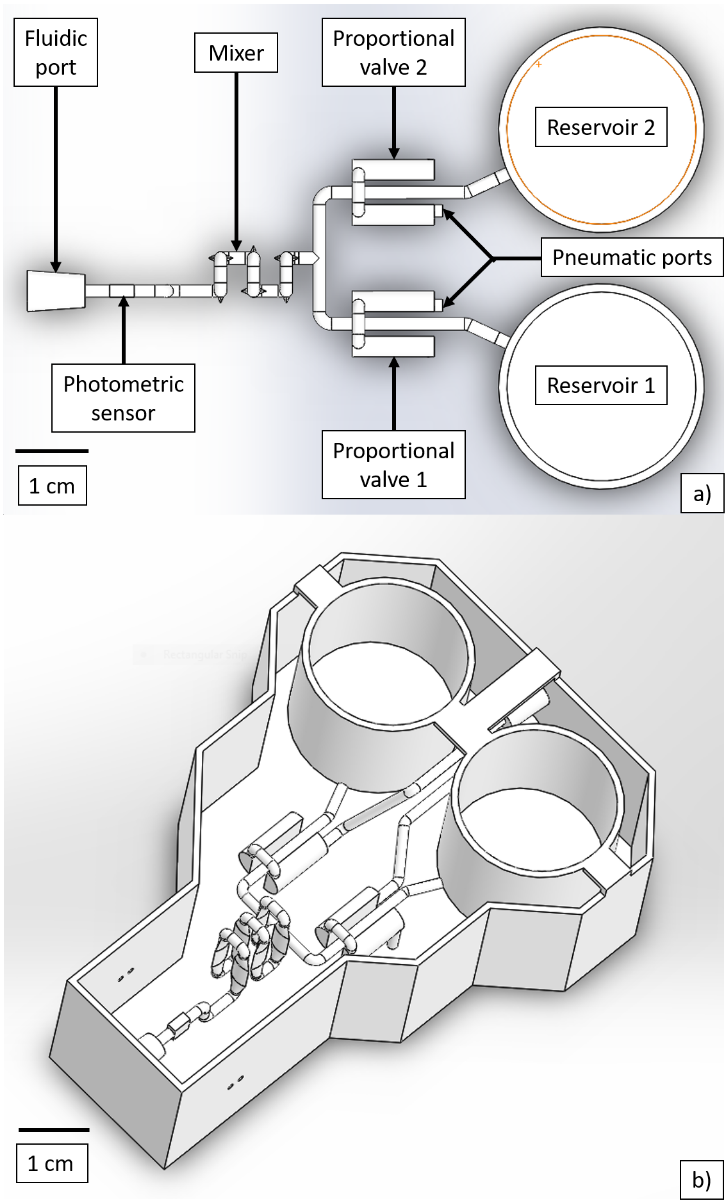

Figure 5.2: CAD of the negative mould for the final iteration of the device. a) Top view where each functional block are labelled. b) General view of the negative mould. The overall dimensions of the mould are $l = 88$ mm, $w = 65$ mm and $h = 27$ mm

The fluidic device is manufactured following the process developed in Chapter 3, with a ratio of monomer:curing agent of 25:1. Figure 5.3 shows the finished fluidic device, ready to by integrated to the enzyme kinetics analysis system.

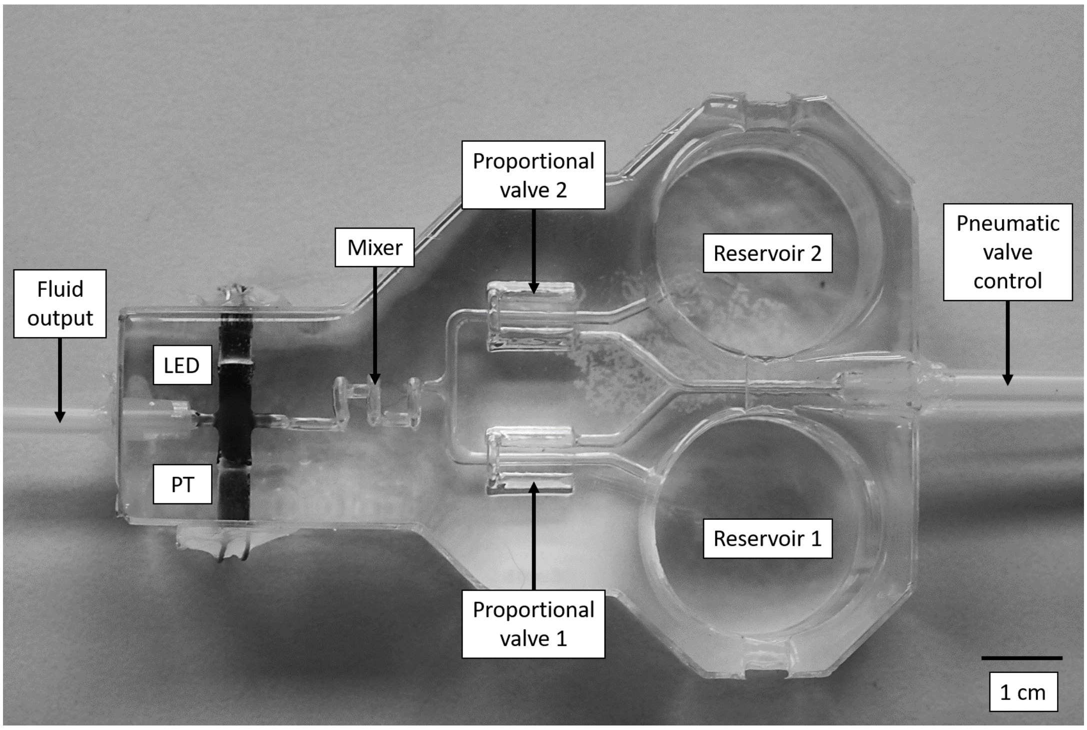

Figure 5.3: Final microfluidic device

5.2.3 System configuration

Figure 5.4 shows a schematic view of the system configuration. The purpose of the solenoid valve was, with the pressure sensor, to regulate the pressure in each proportional valves. Two valves were used to seal the chambers of the proportional valves from the atmosphere. The third solenoid valves was used to vent the pneumatic circuit. The fourth solenoid valve had the same function, but a restriction was added to greatly reduce the flow, allowing for fine control of the pressure. The proportional valves were pressurised with a piston air pump. A peristaltic pump was used to move and mix the fluids from the reservoirs to the photometric sensor and out of the fluidic device.

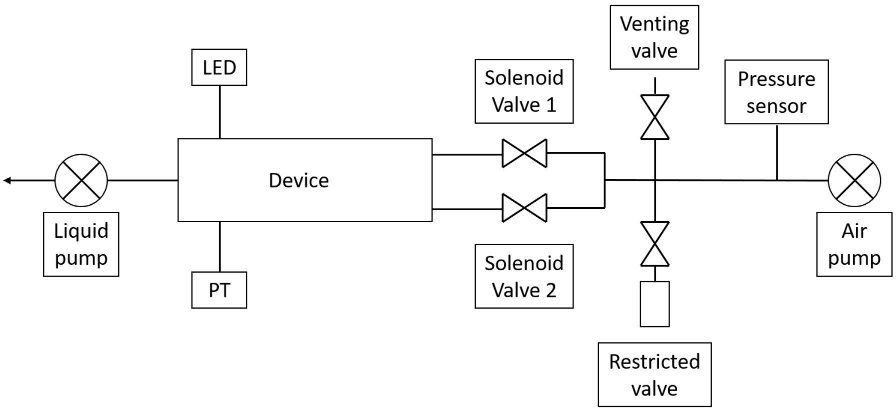

Figure 5.4: Schematics of the configuration of the integrated system

5.2.3.1 Printed Circuit Board

To create a fully integrate system for enzyme kinetics analysis, an electronic control system is necessary. The requirements for such a system are:

- Supply power to the photometric sensor (LED and PT)
- Operate the pressure sensor (power and data)
- Drive pumps and solenoid valves to operate the device (move fluid along the path of the fluidic network, regulate the pressure of the pneumatic valves)
- Provide a surface on which the device can be placed and secured
- Interaction with Matlab for GUI (USB connection)

Figure 5.5 shows a schematics of the electrical circuit.

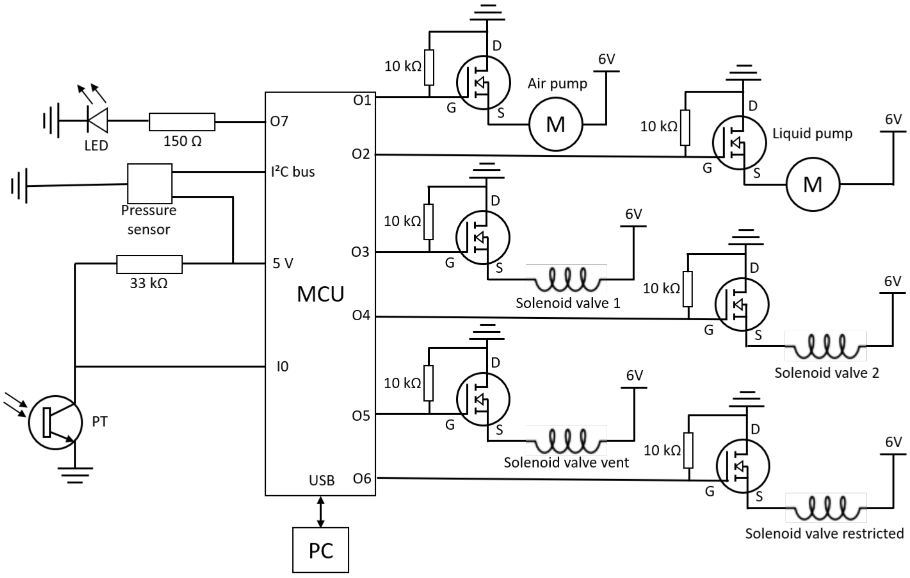

Figure 5.5: Final microfluidic device

The electronic system is composed of: (1) A MCU, or Micro-controller. The purpose of the micro-controller is to receive and send data from a computer via USB and operate the components connected to the PCB. (2) The resistors required for the photometric sensor, as well as connection of the LED and PT embedded in the fluidic device. (3) A pressure sensor, used to measure the pressure inside the proportional valve's chambers (4) Six MOSFETs used to control the array of solenoid valves and pumps.

The PCB is designed for Surface-Mount Technology (SMT) components, with only the pressure sensor, the DC plug and the PCB connectors being through hole components, as seen in Figure 5.6. The primary components of the PCB include:

- An ATmega328p microcontroller [119], to read voltage from photometric sensor and operate the pumps and solenoid valves.
- A FTDI RS232RL USB to serial chip [120], for communication between the PC, via a micro USB, and the micro-controller.

- Six N-channel MOSFETs, controlling 1 air pump, 1 liquid peristaltic pump and four solenoid valves.
- One 5 Psi digital gauge pressure sensor.

The manufacturing of a complete PCB goes as follow:

1. The circuit is developed and tested on a breadboard.
2. Once the circuit design is finalised, the PCB is designed using EAGLE [121]. An outline of the fluidic device is added to ensure the PCB connectors are placed correctly and link with the fluidic device.
3. The EAGLE design is converted to compatible files to be manufactured with a LPKF S63 circuit board plotter [122]. The PCB is manufactured using 1.3 mm double sided board, with a copper thickness of 30 μm.
4. A self adhesive vinyl sheet is placed on the bare PCB. The vinyl layer is then etched with a Fusion 32 laser cutter [123] to expose the PCB, leaving only the solder pads covered and protected. A black acrylic paint is sprayed on the PCB and after allowing for drying, the remaining vinyl is removed. The process ensures the PCB is protected from oxidation and is electrically insulated. The process is repeated on the other side of the PCB.
5. A solder mask is cut in vinyl with the laser cutter (using mask files from EAGLE), then aligned and carefully applied on the painted PCB. Solder paste is thoroughly deposited over the solder mask, ensuring that every pads are covered. The solder mask is then gently removed and the electronic components placed according to the the EAGLE schematics. The PCB is then placed in an oven at 180°C for 5 mins

then the temperatures increased to 230°C for 1 min, allowing for the soldering of the components. The oven is then turned off and the PCB allowed to cool down inside the oven.

6. Finally, the through hole components are placed and soldered.

Figure 5.6 shows the manufactured PCB. The cost for the fully populated PCB is £52.16, placing the total cost of the system at around £70 when all the material used are considered (ABS, PDMS, etc.). A bill of material for the PCB is available in Appendix D2

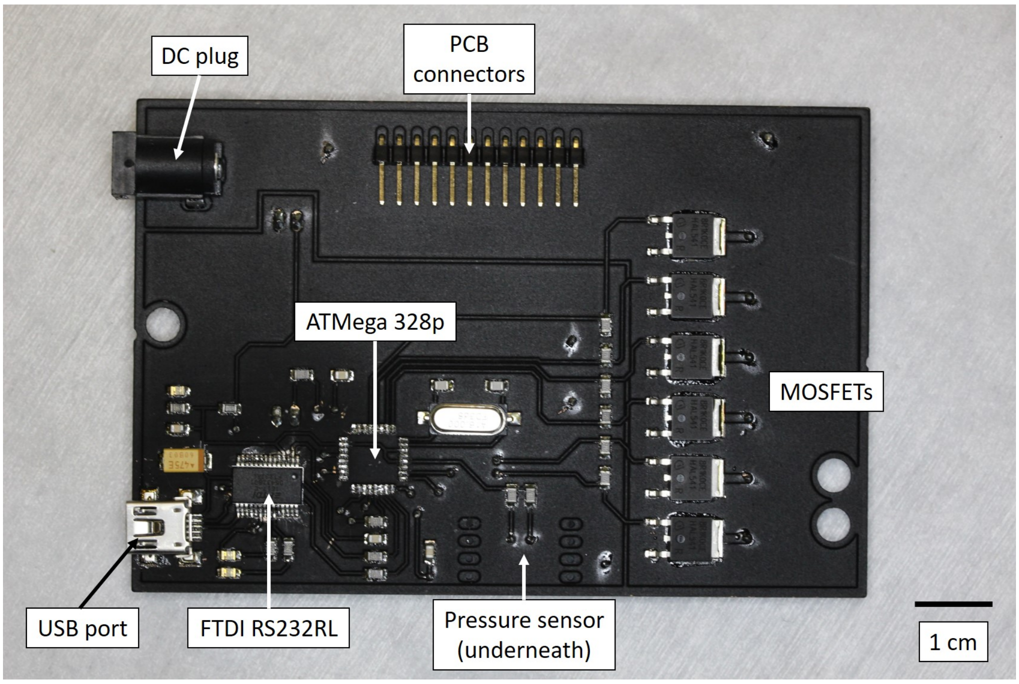

Figure 5.6: PCB designed to operate the fluidic device. Each components are visible, including the micro-controller, MOSFETs, USB connection, etc. The only noticeable components not visible is the pressure sensor as it is located on the opposite side of the PCB

5.2.3.2 Pressure sensor behaviour

The 5 Psi gauge pressure sensor sends the measured data as a percentage of its range. Therefore, according to the data sheet, a reading of 10 % is equivalent to atmospheric pressure and a reading of 90 % is equivalent to 5 Psi. Unfortunately that is not how it behaves, as early testing showed a reading of 6 % at atmospheric pressure, double the error advertised. This could potentially mean that if a pressure of 5 Psi is applied to the sensor, it could send a reading different from the 90 % as advertised. Fortunately, this characteristic does not affect the device, as it works with relative pressures.

5.2.4 User control and data analysis

Two different GUI (Graphical User Interface) are designed with Matlab 2016b [124]. The first GUI is designed for the characterisation of the proportional valves. The second GUI is designed to operate the device, interact with the user of the system and perform the enzyme kinetics analysis. The full codes are available in the supplement CD.

5.2.4.1 Proportional valve analysis tool

Characterisation of the proportional valves within the fluidic device is required. The purpose is to establish if the functional block approach is valid for the design of fluidic devices. For that, a GUI is designed:

1. The code scans for connected devices before the GUI appears on screen and lists them.
2. The GUI has multiple user parameters available. COM port selection, minimum and maximum pressures to apply to the valves, as well as the interval between each pressure, and a choice between which proportional valve is to be calibrated.

3. When “Start” is pressed, the code closes both proportional valves, and asks the user to fill the reservoirs with *p*-nitrophenol solution on reservoir one and 500 mM Tris, 10 mM $MgCl_2$ buffer in reservoir two. The code then empties the fluidic channels of air by pumping a small quantity of liquid from both reservoirs, one after the other.

4. In a loop, the code then tries to match the pressure inside the proportional valve with the first pressure setting to be tested (reference pressure). If the pressure is too high, the restricted solenoid valve is open for 0.1 s. If the pressure is too low, the air pump is activated for 0.01 s (if the reference pressure is higher than 25 %, the air pump is activated for 0.3 s). The loop runs until the pressure inside the proportional valve matches the reference pressure, or until the loop count reaches 100. The loop is repeated for each pressure present in the list. If the code cannot match the reference pressure within the length of the loop, the final pressure would is displayed in the summary table.

5. The next step is to read the voltage from the photometric sensor for 30 s, every 100 ms. The mean of the values is then calculated and stored in a matrix with the corresponding pressure. Additionally, the mean voltages and pressures are plotted on the GUI for the user to follow the progress of the experiment.

6. When the characterisation test is finished, all the collected data are displayed in a summary table for the user to analyse.

7. Finally, after the characterisation is finished, the “Clean” button is trigger by the user. The script is deigned to clean the fluidic device by asking the user to fill the reservoirs with Isopropyl alcohol, which is then be pumped through the fluidic device. The flushing is repeated three times.

Figure 5.7 shows the GUI for the proportional valve characterisation tool. The full code is available in the supplement CD.

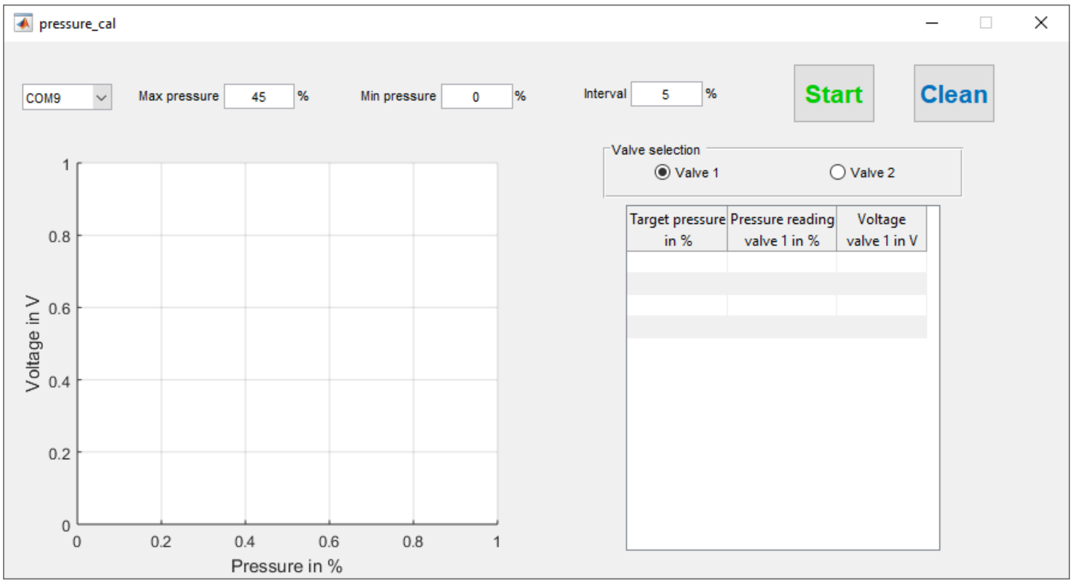

COM9

Max pressure 45 %

Min pressure 0 %

Interval 5 %

Valve selection

● Valve 1 ○ Valve 2

Target pressure in %	Pressure reading valve 1 in %	Voltage valve 1 in V

Figure 5.7: GUI used to characterise the proportional valves. At the top of the GUI are user inputs, use for experimental setup. On the left is a window displaying the data from the pressure sensor. On the right is a selector, to choose which valve to characterise. Underneath is where the results from the characterisation are stored

5.2.4.2 Enzyme kinetics analysis tool

A matlab GUI is designed to operate the fluidic device for Michaelis–Menten enzyme kinetics analysis and consists of two parts. The first part, designed to prime the fluidic device, proceeds as following:

1. Before the GUI appeared on screen, the code scans for available COM ports.
2. The user selects the COM port associated with the system and then presses “Fill wells”.
3. Solenoid valves 1 and 2 are opened and then the air pump is activated for 1.5 s, closing both proportional valves.

4. The solenoid valve 2 is closed and the venting solenoid valve is opened, fully opening the proportional valve 1.
5. The liquid pump is activated for 0.25 s to fill up the fluidic network of the solution contained in reservoir 1.
6. The venting solenoid is closed and the air pump activated for 0.75 s, closing the proportional valve 1.
7. The solenoid valve one is closed.
8. The procedure is repeated for the proportional valve 2 and reservoir 2, thus ensuring no gas is present in the fluidic network.
9. A pop-up window confirms that the fluidic device is primed.

The second part, designed to collect the data necessary for the enzyme kinetic analysis, proceeds as following:

1. The user enters the desired ratios between the enzyme and substrate (i.e. difference concentrations) necessary for the analysis as well as the length of the experiment and the delay, if necessary.
2. The user then presses the "Start" button. The Matlab code calculates the pressures necessary in each proportional valves according to the each user's defined ratios based on the photometric sensor calibration curve and the proportional valves calibration curve.
3. The Matlab code then starts with the first analysis by adjusting the air pressure in one of the proportional valve, according to the first ratio studied. Once the pressure is correct, the device runs the liquid pump for 0.25 s.

4. After the enzyme and substrate are mixed, the photometric analysis commences. The code takes a voltage reading of the photometric sensor every 100 ms for the duration set by the user, and saves the data in a storage matrix.

5. The analysis is repeated for every user defined ratios. One finished, the data is exported as a .csv file.

6. After the analysis is completed, the user can choose to flush and clean the fluidic device.

Figure 5.7 shows the GUI while an experiment takes place.

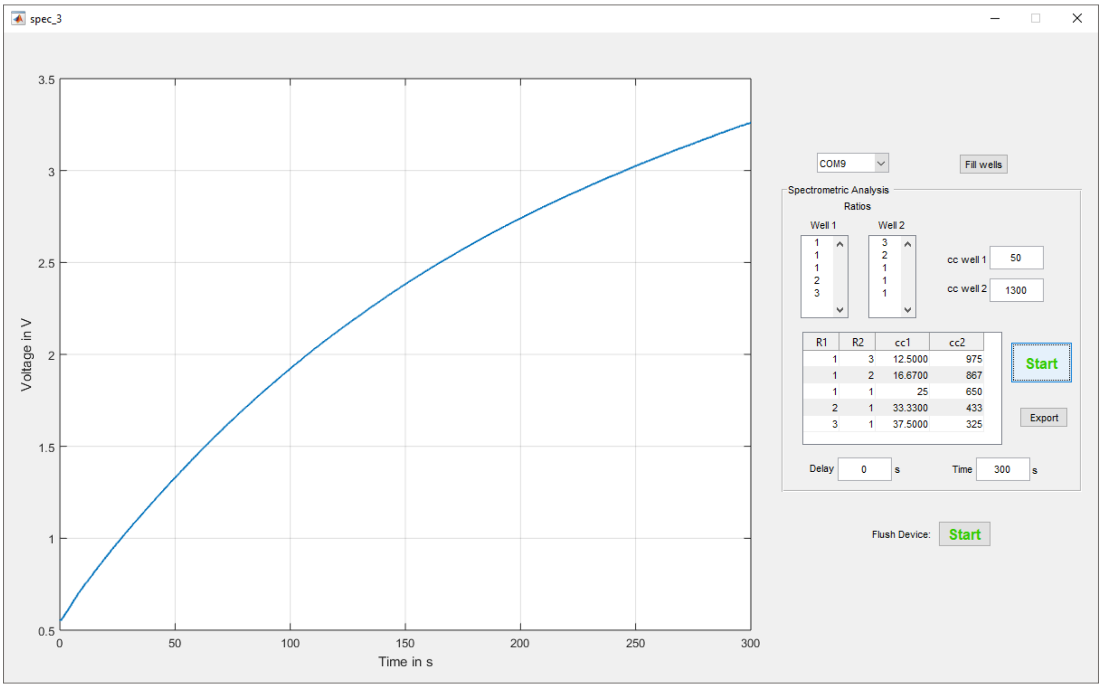

COM9

Well 1: 1, 1, 1, 2, 3

Well 2: 3, 2, 1, 1, 1

cc well 1: 50

cc well 2: 1300

R1	R2	cc1	cc2
1	3	12.5000	975
1	2	16.6700	867
1	1	25	650
2	1	33.3300	433
3	1	37.5000	325

Delay 0 s

Time 300 s

Figure 5.8: GUI used to operate the fluidic device. On the left is a large window shows the data from the photometric sensor in real time. On the right are multiple user input boxes, used to determine the parameters of the experiment. Those include the COM port selection, to connect to the board, inputs for ratios between the two wells and the concentration of the products they store. Additional inputs include a delay, if the reaction takes time to start and a time setting to determine the duration of the experiment

5.3 Characterisation of the fluidic device

To validate the approach of using functional block to design fluidic device, the photometric sensor and the valves need to be characterised to be compared with the data from Chapter 4.

5.3.1 Photometric sensor

To verify that the sensor embedded in the fluidic device behaves the same as the functional block tested in Section 4.6, a characterisation experiment is performed, using the same parameters. A *p*-nitrophenol solution is pipetted inside the analysis chamber, with successive concentration varying from 250 µM to 0.89 µM via double dilution, with concentrations of 200 µM, 180 µM, 160 µM, 133 µM, 100 µM and 80 µM added for a better spread of the concentrations. The voltage is recorded with an Arduino Uno combined with the Matlab GUI described in Section 5.2.3. A voltage reading is taken every 100 ms for 30 s (3000 data points total). The mean value is then calculated by the Matlab code and displayed to the user, who enters the data in a spread sheet. Figure 5.9 shows the results from the calibration done on the photometric sensor developed in chapter 4. Also on the graph are present the results from the voltage readings performed on the photometric sensor embedded in the fluidic device. Both curves behave similarly, within the SD, confirming the quality and consistency of the sensor across the two different fluidic devices.

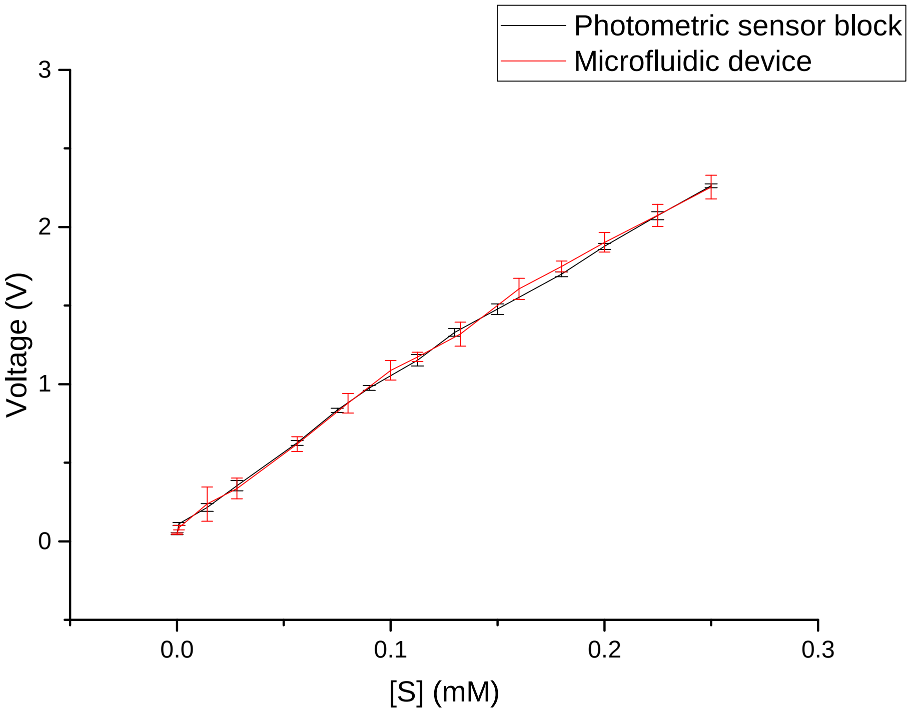

Figure 5.9: Calibration curve for the photometric sensor block and the photometric sensor embedded in the microfluidic device, mean of 5 reading and 1 SD

5.3.2 Proportional valves

The proportional valves are characterised, using the GUI described in Section 5.2.4.1, to determine how the pressure is affecting the flow and calculate the ratios between both valves. Reservoir 1 is filled with a 300 µM *p*-nitrophenol solution and reservoir 2 is filled with a 500 mM Tris, 10 mM $MgCl_2$ buffer with a pH of 8.0. The range of pressure is 0 - 45 % with 5 % steps, or 0 - 155 mbar with 17 mbar steps. Higher pressures were not studied as the flow is greatly reduced (see Section 4.5), thus generating high errors of mixing ratio and making the kinetics analysis unreliable. The experiment was repeated 3 times and the mean values displayed in Figure 5.10.

From 0 % to 10 %, the mean voltage remains similar for both valves, indicating that the flow is seeing very little constraint from the proportional valves, similar to the results obtained during the calibration of the proportional valve block developed in Chapter 4. Because the photometric sensor has a linear behaviour, the voltage at 0 % pressure should be half of the range, Δ_V. The maximum mean voltage, for proportional valve 2 at 40 %, was 2.301 while the minimum voltage, for proportional valve 1 at 40 %, was 0.193 V. Therefore $\Delta_V = 2.108$ V. At 0 % pressure, the mean voltage was 1.396 V. Compared to half Δ_V, 1.054 V, the difference indicates that the ratio between the proportional valves is not 1:1, when they are both fully open, but close to 2:1 (valve 1 to valve 2 ratio).

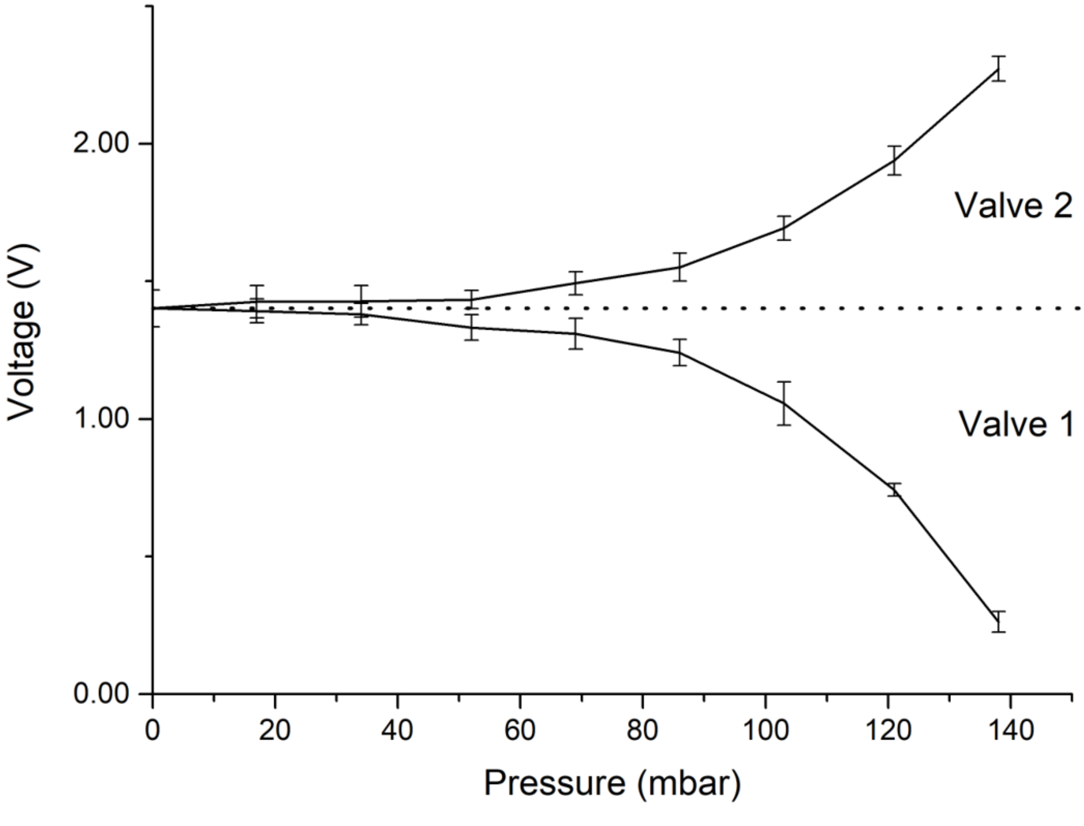

Figure 5.10: Calibration curve for the 2 proportional valves, mean of 5 reading and 1 SD

Those results, combined with the photometric sensor calibration curve, allows the Matlab code to operate the proportional valves according to the user input.

5.3.3 Peristaltic pump

A peristaltic pump was used to generate the flow of liquids inside the fluidic device. The liquid pump had a 20-60 ml/min flow rate according to the seller [125]. To reduce the amount of liquid used by the fluidic device, and therefore increasing the number of experiments out of the volume contained in the two reservoirs, an accurate measurement of the flow rate of the liquid pump was necessary. As defined by the Matlab code seen in section 5.2.4.2, the length of time the liquid pump was operated was 0.25 s. This value is likely to be more that the actual time the pump runs, due to inertia. Therefore a simple experiment was conducted. The liquid pump was operated for 0.25 s, moving water through the fluidic device (the device was primed before hand). After a pause of 2 s, the liquid pump was operated for 0.25 s again. This was repeated 20 times, due to the small volume of water being pumped each time. The water was collected in a reservoir and the weight measured. The flow rate was calculated by dividing the mass of water collected by 20. The calculated flow rate was 4.67 mg/s. This value was used to calculate the Reynolds number in Section 4.4.

Figure 5.11 shows the integrated fluidic device. The fluidic device is connected to the PCB and the solenoids and pumps, located inside the container closed by the PCB. Blue food colouring in water is used to highlight the fluidic network.

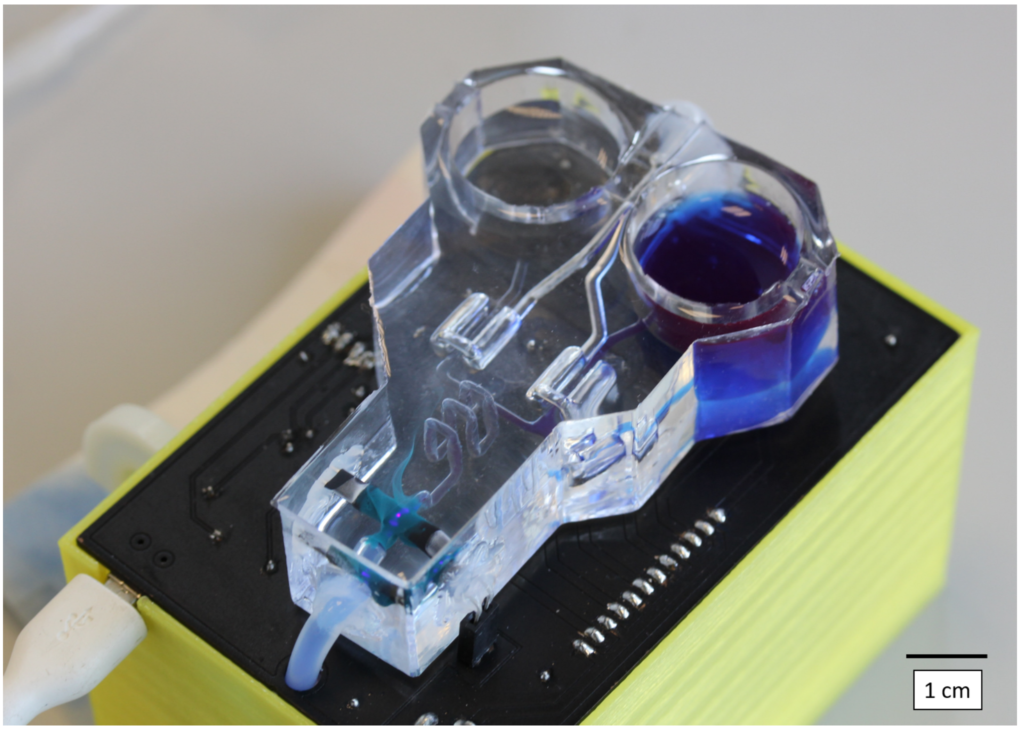

Figure 5.11: Integrated fluidic device. The fluidic device is placed on-top of the control PCB, and connected to the solenoids and pumps, via through holes, located in the container closed by the PCB. Dyed water is used to highlight the fluidic network.

5.4 Enzyme kinetics analysis

A single substrate-enzyme reaction can be simplified as a two step mechanism which occurs as follows:

$$E + S \Leftrightarrow ES \Leftrightarrow E + P \tag{5.1}$$

where:

- E is the enzyme
- S is the substrate
- P is the product

K_m, or the Michealis-Menten constant, is defined as the concentration necessary to achieve half of the maximum velocity for a given concentration of enzyme. To determine the maximum velocity, v_{max}, an experiment is done over a varying concentration of substrate.

$$v = \frac{v_{max}\,[S]}{K_m + [S]} \tag{5.2}$$

where:

- v : reaction velocity
- v_{max} : maximum reaction velocity
- *[S]* : substrate concentration
- K_m : Michaelis-Menten constant

During the reaction of the colourless *p*-nitrophenyl phosphate (substrate) with an alkaline phosphatase (enzyme), the the production of the yellow coloured by-product *p*-nitrophenol, is used to demonstrate the integrated fluidic device. The reason for choosing this particular reaction is the speed at which it happens, typically within minutes [113,114], making the development of the sensor described in Section 4.6 easier. The data analysis for the Michealis-Menten enzyme kinetics is performed using Origin. The initial velocity of each reading is determined by linear fit over the first 25 seconds of data collection.

5.4.1 Commercial equipment

A Synergy HTX Multi-Mode Reader [126] was used to perform the enzyme kinetics analysis for comparison to the system developed in this thesis. The *p*-nitrophenyl phosphate substrate concentration was 1.39 mM and was reduced to 0.04 mM, via double dilution, which gave 7 different concentration for analysis. The alkaline phosphatase enzyme solution had a concentration of 50 µg/ml. The solutions were mixed with a 1:1 ration in a 96 wells plate and placed in the reader for analysis, with a sample rate of 10 s. The machine had only one sensor, therefore the measurement of absorbance for each solution was done for one well after the other, reducing the time resolution. Additionally, the mixing of enzyme and substrate was done outside the machine, and by the time the reading starts, the reaction was under way and valuable data was not recoded (Michaelis–Menten enzyme kinetics analysis relies on the initial velocity of the reaction). Figure 5.12 shows the 96 wells plate with the *p*-nitrophenol solution after the reaction had occurred. Three analyses were performed at the same time, for accuracy.

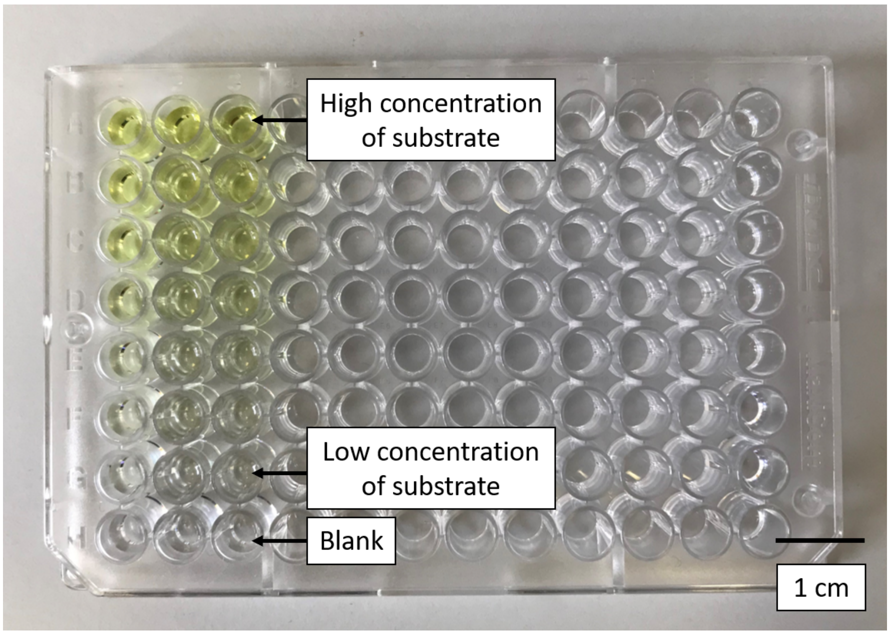

Figure 5.12: 96 wells plate used for the enzyme kinetics analysis done with the multi-mode reader

Figure 5.13 shows the results of the experiment. Via the built-in Michaelis–Menten enzyme kinetics analysis curve fitting in Origin, the calculated value of K_m is 0.085 mM ± 0.032 mM, close to the value of 0.06 reported in literature [113,114]. The fitting of the curve is not ideal. This shows the limitations of the commercial equipment used for this experiment. The reaction obeys the Michaelis–Menten equation (see Eq. 5.1), therefore if the curve does not fit, it shows that either the mixing was not done properly or that the time resolution of the machine is not adequate.

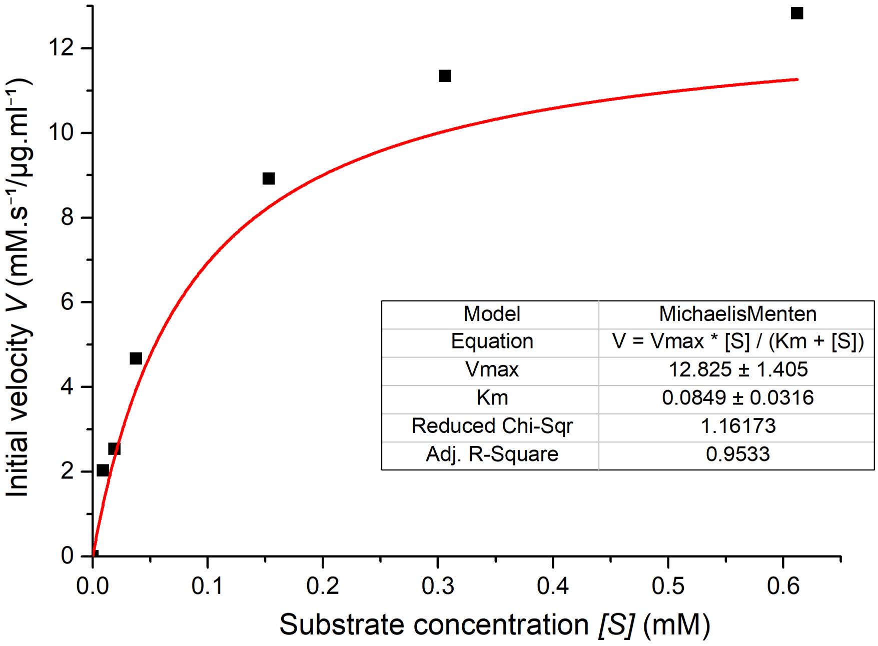

Model	MichaelisMenten
Equation	V = Vmax * [S] / (Km + [S])
Vmax	12.825 ± 1.405
Km	0.0849 ± 0.0316
Reduced Chi-Sqr	1.16173
Adj. R-Square	0.9533

Figure 5.13: Michaelis–Menten saturation curve for *p*-nitrophenol for the multi-plate reader. Error bars not visible

5.4.2 Fully integrated fluidic device

For this experiment, solutions with varying concentration of substrate were prepared beforehand. The substrate and enzyme solution were then placed in the reservoirs and mixed through the fluidic device with a 1:1 ratio, by adjusting the proportional valves accordingly, through the GUI. This experiment performed for direct comparison with the commercial equipment. Figure 5.14 shows the the voltage evolution as the hydrolysis of p-nitrophenyl phosphate by alkaline phosphatase at pH 8.0 occurs, changing the absorbance of the solution. The experiment length was 5 minutes with no delay.

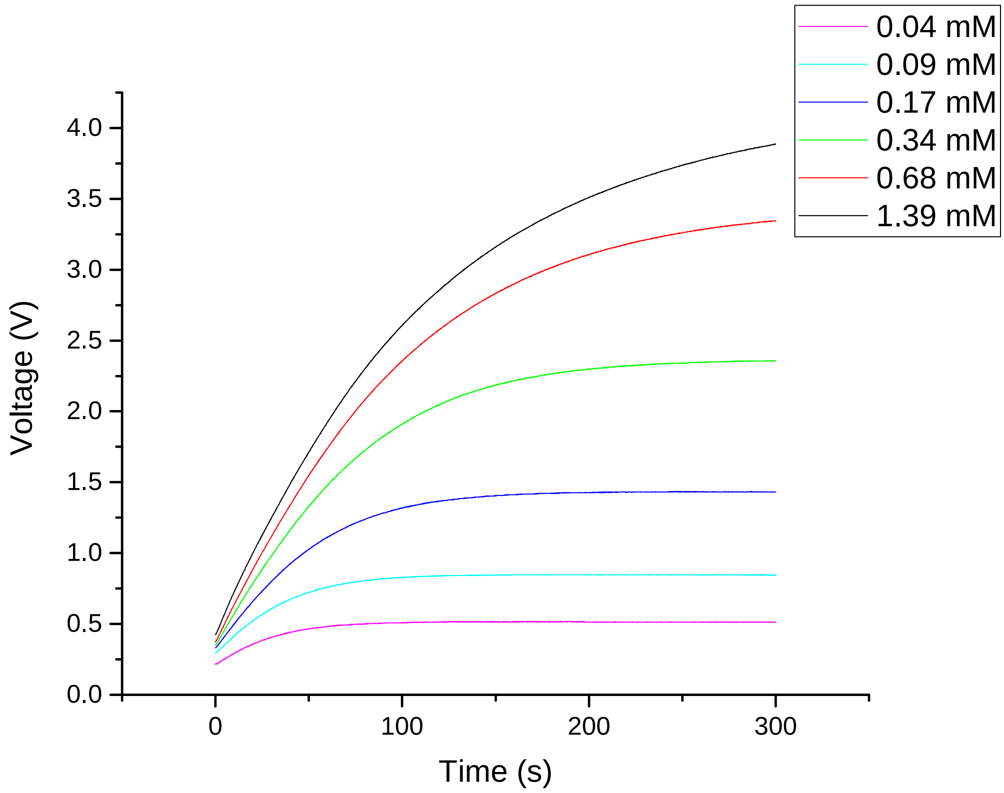

Figure 5.14: Change in sensor voltage as the hydrolysis of p-nitrophenyl phosphate by alkaline phosphatase at pH 8.0 occurs. The data for each concentrations are a mean value of 3 runs.

From those data, the initial velocity was calculated. First a linear fit was done for the first 25 seconds of the reaction occurring, which gave a value expressed in terms of voltage per second. All the initial velocity values were fitted against the sensor calibration curve and converted to millimoles per second. Then the values were divided by the alkaline phosphatase enzyme concentration, 25 µg/ml (half of the value given earlier, as the enzyme was mixed with the substrate with a 1:1 ratio). Table 5.1 summarises the initial velocities for each substrate concentration. Finally, the results are plotted in Origin and K_m is calculated Via the built-inMichaelis–Menten enzyme kinetics analysis curve fitting:

Table 5.1: Table of mean value of initial velocities for each substrate concentrations and 1 SD

[S] (mM)	Initial velocity (mmol $\mathrm{s^{-1}\,\mu g^{-1}\,ml^{-1}}$)	SD
0.02	2.401466	0.038336
0.045	3.762666	0.069111
0.085	5.267733	0.019168
0.17	7.126933	0.019168
0.34	7.956933	0.069111
0.695	8.388533	0.101428

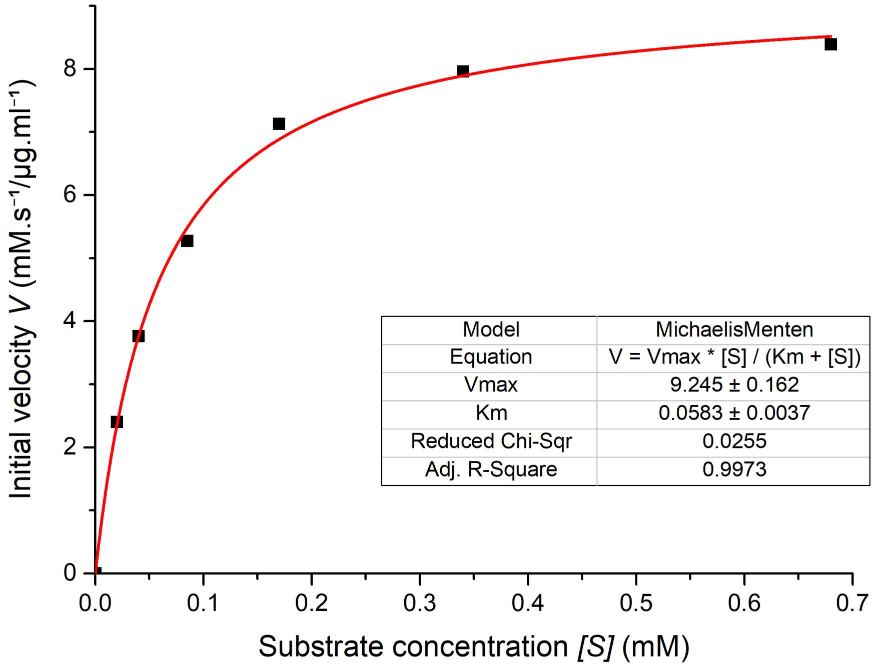

Model	MichaelisMenten
Equation	V = Vmax * [S] / (Km + [S])
Vmax	9.245 ± 0.162
Km	0.0583 ± 0.0037
Reduced Chi-Sqr	0.0255
Adj. R-Square	0.9973

Figure 5.15: Michaelis–Menten saturation curve for *p*-nitrophenol for the fluidic device. Error bars not visible

The calculated value of K_m is 0.0583 mM ± 0.004 mM, consistent to the value of 0.06 mM reported in literature [113, 114]. This confirmed that the integrated fluidic device performed as expected, being able to be used as a tool for enzyme kinetics analysis. More importantly, it was closer than the value reported by the commercial equipment, showing the reliability and accuracy of the fluidic device.

5.4.3 Additional testing

The aim of the integrated fluidic device was to create a completely autonomous system that performs the dilution of the substrate for the enzyme kinetics analysis. Therefore a second experiment with the fluidic device was performed. Reservoir 1 was filled with a *p*-nitrophenyl phosphate with a concentration of 0.68 mM and reservoir 2 was filled with an enzyme solution with a concentration of 50 µg/ml. 5 ratios were entered in the GUI: 3:1, 2:1, 1:1 1:2 and 1:3.

Table 5.2: Concentration of enzyme and substrate for reach ratio

Ratio	3:1	2:1	1:1	1:2	1:3
Substrate concentration (mM)	0.51	0.45	0.34	0.23	0.17
Enzyme concentration ($\mu g/ml$)	12.5	16.7	25	33.3	37.5

Table 5.2 shows the concentration of enzyme and substrate in the solution for each ratio. The length of the experiment for each ratio was set to 5 minutes with no delay. Figure 5.16 shows the Michaelis–Menten saturation curve.

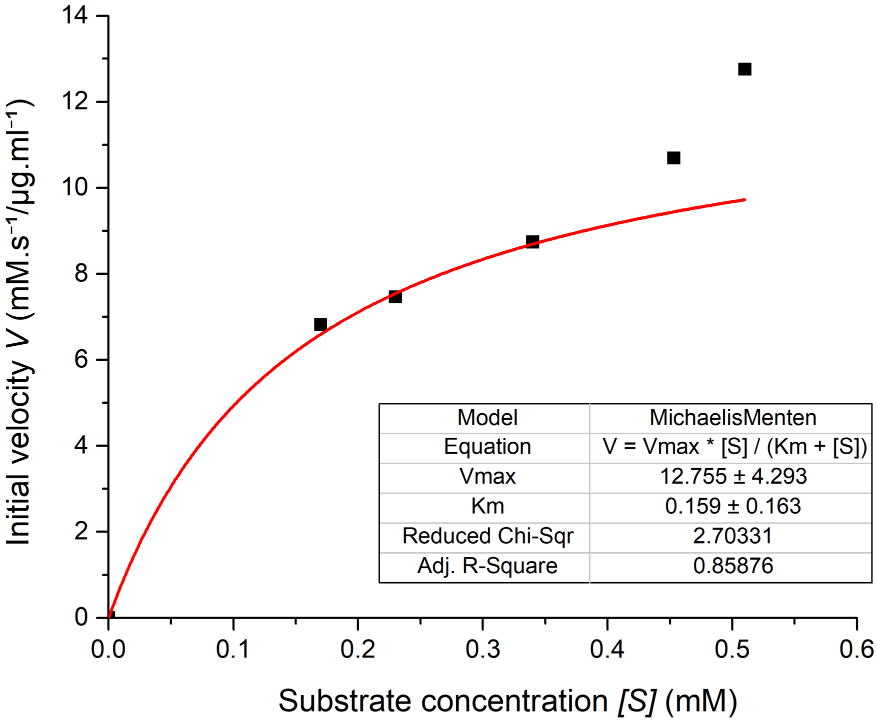

Figure 5.16: Michaelis–Menten saturation curve for *p*-nitrophenol for the additional experiment. Error bars not visible

This experiment did not proceed as expected. An increase in initial velocity with increased substrate concentration was still present, but the calculated K_m is not the value that was to be expected for *p*-nitrophenyl phosphate. Via the built-in Michaelis–Menten enzyme kinetics analysis curve fitting in Origin, the calculated value of K_m was 0.15 mM ± 0.16 mM.

5.5 Summary

The aim of this chapter was to design an integrated fluidic device for Michaelis–Menten enzyme kinetics analysis, based on functional block developed in Chapter 4. The fuidic device was manufactured using PDMS prepared with a ratio of 25:1, resulting in reduced air pressures necessary to close the proportional vales. To operate the microfluidic device, a control system was necessary. The device was controlled via a custom PCB, which contained a RS232 serial to USB chip to communicate with a PC and a microcontroller to operate the various solenoid valves and pumps required to control the fluidic device. A GUI was created using Matlab to interface with the PCB and control the device to perform Michaelis–Menten enzyme kinetics analysis. Finally, the fluidic device was tested against a commercial multi-plate reader. Michaelis–Menten enzyme kinetics analysis of $p$nitrophenol phosphate hydrolysis by alkaline phosphatase at pH 8.0 was performed. When the integrated fluidic device and the multi-plate reader were evaluated with similar substrate concentrations, the integrated fluidic device showed more consistent K_m value than the commercial equipment when compared to literature. The results where less conclusive when the device was performing the the kinetic analysis based on ratios entered in the GUI, possibly due to the more restricted range of concentrations chosen for the experiment.

Chapter 6

Discussion and Future Work

Manufacturing process:

By combining the lost core method and 3D printing technology with the properties of PDMS in solvents, a new manufacturing process was developed. Following simple guidelines, a complex 3D fluidic device could be manufactured. The manufacturing process had 6 steps: (1) a negative mould of the fluidic device was designed and 3D printed with ABS; (2) the surface of the mould was smoothed with acetone. FDM printer create a rough finish, unsuitable for fluidic devices; (3) PDMS was poured in the mould and cured; (4) once cure, the PDMS and embedded mould were placed in an acetone bath. PDMS swells in polar solvent therefore the acetone would gradually reach the embedded ABS, which dissolves in acetone; (5) the liquefied ABS was flushed out of the PDMS, leaving a void which formed the fluidic network; (6) the device was left to rest for the acetone to evaporate.

Compared to soft lithography, this method has a lower cost, as it does not require access to a cleanroom. It also offers a large degree of complexity due to its inherent 3D nature.

On the other hand, the manufacturing process is slower, three to five days, depending on the volume of the device, compared to one day for soft lithography. The minimum feature size is much bigger, 1 mm compared to 50 µm or less for soft lithography. The same observations can be made for micromachining. Cost is higher, although not as high soft lithography, and the minimum feature size is lower, about 200 µm. Manufacturing time is also quicker and a simple piece can be fabricated in 10-15 mins. In terms of complexity, micromachining suffers form the same limitations as soft lithography, due to the 2D nature of the manufacturing technique.

Future work should focus on optimising the manufacturing process. By placing the devices in a vacuum chamber after the acetone bath, the evaporation time could be greatly reduced. Using acetone vapour during the surface smoothing step should be explored. Although it was discarded as a time-saving measure as it would increase the lead time, it would reduce the risk of damaging the moulds and could potentially create more consistent parts by reducing the direct exposure to acetone.

Functional blocks:

Functional blocks, some of which included multiple domains, were designed, manufactured and characterised. The functional blocks included a port, a reservoir, a mixer, a proportional valve and a photometric sensor.

Passive functional blocks included a port, used to connect fluidic devices to pumps and external reservoirs. The port was designed to connect to 4 mm OD silicone tube. A simple reservoir, with a capacity of 9 ml was also designed. Its purpose was to store reagent or waste. Finally, a mixer was designed. The shape of the mixer was conceived to generate turbulent by changing it cross section area. After CFD simulations revealed that it was not working as expected, a mixing block made of six modules was designed. CFD simulations confirmed the turbulent flow generated by the mixer. Turbulent flow is important for this design as it allowed to create a compact mixer and saved material. An active functional block included a pneumatic proportional valve, grouping a fluidic domain and a pneumatic domain in a functional block. A fluidic channel was surrounded by two chambers. When pressurised air was in pumped into the chambers, the fluidic channel located in the middle was pinched, restricting the flow. If the pressure was high enough, the valve closed. For the functional block tested, 190 mbar of air pressure was sufficient to close the valve for a head pressure of 100 mbar in the fluidic channel. Therefore 90 mbar is the pressure necessary to deform the PDMS.

By joining a fluidic domain and a electronic domain, a photometric sensor functional block was designed. The device used an UV LED and a PT to measure the absorbance of light of a solution placed in between in a analysis chamber. The sensor was designed for Michaelis–Menten enzyme kinetics analysis, with an LED peek emittance of 400 nm. The device was characterised with a range of resistors for for the LED and PT. The most suitable combination, showing a linear behaviour for the sensor with a high sensitivity, was 105 Ωof the LED and 33 kΩof the PT.

Future work would look into modifying the photometric sensor. By replacing the LED with an optic fibre, the sensor could be made more flexible as different light sources could be used. Developing additional functional blocks is also important. With an increased number of functional blocks, a wider range of fluidic devices can de designed. Such examples include embedded coils, which could be used for sensing, heating up a solution of moving fluids or embedded components. Another example is a check valve, useful for passive control of the flow. Those examples can be found in Appendix C.3. Future work should focus on the development of additional functional blocks. Appendix C.3 shows a few potential designs.

Enzyme kinetics analysis fluidic device:

An integrated fluidic device was designed using functional blocks from an abstraction layer. The device was designed to perform Michaelis–Menten enzyme kinetics analysis. The fluidic layer included two reservoirs, two proportional vales, a mixer and a photometric sensor. The control layer included an electronic circuit and various pumps and solenoids. It was designed to operate the fluidic device via a GUI.

The characterisation showed that the photometric sensor operated identical to the functional block used in Chapter 4, within error. Unfortunately, it was not the case of the proportional valves. The characterisation revealed that one valve had a higher flow restriction that the over, with a ratio of 2:1. The pressure to shut the valve is the same for both and the behaviour is the same even when the valves are fully open, so the chambers are not the source of the issue. Therefore the problem comes from the fluidic channel. There are two possible options to explain the problem: (1) the manufacturing of the mould was not consistent enough. Some extra material could be present on one of the fluidic channels. During the acetone smoothing, the excess material would dissolve and spread onto to the channel, increasing the the cross section area; (2) the acetone smoothing is not consistent enough to manufacture two valves with similar characteristics. Understanding and correcting this problem is essential to the development of the manufacturing process.

The first test for the integrated device gave very good results. The device showed more accuracy that the plate reader. The calculated K_m was 0.0583 mM ± 0.004 mM compared to 0.085 mM ± 0.032 mM for the plate reader (0.06 mM is the value found in literature review). The results for the autonomous testing were not conclusive. The calculated enzyme kinetic was K_m is 0.15 mM ± 0.16 mM, far from the value expected with a unrealistic error. The unexpected result is most likely due to the limited range of concentration the device can achieve. The previous tests use substrate concentration from 0.695 mM down to 0.02 mM. The device could achieve a substrate concentration going from 0.51 mM to 0.17 mM. To improve the device, a third well can be added to store the buffer, increasing the range of enzyme concentration that can be studied, especially allowing to mix solutions with lower substrate concentrations.

Future work should develop the design of fluidic device from a schematic level. The approach explored in this thesis should include other manufacturing technologies such as soft lithography, direct 3D printing of the devices and CNC milling. The abstraction level of the design should be increased whereas the choice of manufacturing process is only dictated by the systems requirements. The choice of material and manufacturing process should be a consequence of systems requirement.

Chapter 7

Conclusion

This thesis demonstrated the design and manufacture of a fully integrated fluidic device. Using the lost core method and additive manufacture techniques, a low cost manufacturing process was developed to enable the creation of multi-domain functional block. Such domains include pneumatic, fluidic, electronic and optic. By designing and characterising functional blocks separately, each tailored to perform a simple function, complex fluidic device can be easily designed and no further characterisation is necessary.

Using this approach, an integrated fluidic device was created. The device integrated all the components necessary to perform Michaelis–Menten enzyme kinetics analysis. Such components were divided into two layers. The fluidic layer, including a photometric sensor, proportional valves, a mixer, two reservoirs and various ports to connect to the control layer. The control layer used a PCB, various pumps and solenoids to control the fluidic device, via a GUI. The integrated device perform the analysis with a higher level of accuracy than the commercial equipment, for a fraction of the cost.

The work presented demonstrated a new approach to the design of fluidic devices where the lengthy characterisation process could be removed entirely. It also shows an alternative route away to chip-in-a-lab by reducing the cost and the size and increasing the autonomy and the portability of the system.

Bibliography

[1] L. Michaelis, M. Menten, K. A. Johnson, and R. S. Goody, “The original michaelis constant: Translation of the 1913 Michaelis–Menten paper,” *Biochemistry-us*, vol. 50, no. 39, pp. 8264–9, 2011.

[2] Vishay Intertechnology. Malvern, Pennsylvania, USA.

[3] OSRAM Licht AG. Munich, Germany.

[4] S. J. Trietsch, T. Hankemeier, and H. J. van der Linden, “Lab-on-a-chip technologies for massive parallel data generation in the life sciences: A review,” *Chemometrics and Intelligent Laboratory Systems*, vol. 108, no. 1, pp. 64–75, 2011.

[5] Á. Ríos, M. Zougagh, and M. Avila, “Miniaturization through lab-on-a-chip: Utopia or reality for routine laboratories? A review,” *Analytica Chimica Acta*, vol. 740, pp. 1–11, 2012.

[6] D. C. Duffy, C. J. McDonald, O. J. A. Schueller, and G. M. Whitesides, “Rapid prototyping of microfluidic systems in poly(dimethylsiloxane),” *Analytical chemistry*, vol. 70, no. 23, pp. 4974–4984, 1998.

[7] A. Manz, N. Graber, and H. Widmer, “Miniaturized total chemical analysis systems: A novel concept for chemical sensing,” *Sensors and Actuators B: Chemical*, vol. 1, no. 1, pp. 244 – 248, 1990.

[8] J. Castillo-León and W. E. Svendsen, *Microfluidics and Lab-on-a-Chip Devices: History and Challenges*, pp. 1–15. Cham: Springer International Publishing, 2015.

[9] D. Harrison, K. Fluri, K. Seiler, Z. Fan, C. Effenhauser, and A. Manz, “Micromachining a miniaturized capillary Electrophoresis-Based chemical analysis system on a chip,” *Science*, vol. 261, no. 5123, pp. 895–897, 1993.

[10] Y. Xia and G. M. Whitesides, “Soft Lithography,” *Annual Review of Materials Science*, vol. 28, pp. 153–184, 1998.

[11] Nature. https://www.nature.com/subjects/microfluidics, Last accessed: 24/09/2017.

[12] P. Watts and S. J. Haswell, “Microfluidic combinatorial chemistry,” *Curr Opin Chem Biol*, vol. 7, no. 3, pp. 380–387, 2003.

[13] A. Ali, O. Sandre, and V. Cabuil, “Microfluidics in inorganic chemistry,” *Angewandte Chemie Int Ed*, vol. 49, no. 36, pp. 6268–6286, 2010.

[14] G. Pascali, P. Watts, and P. A. Salvadori, “Microfluidics in radiopharmaceutical chemistry,” *Nucl Med Biol*, vol. 40, no. 6, pp. 776–787, 2013.

[15] T. Davis, S. Athey, M. Vandevender, C. Crihfield, C. E. C. Kolanko, S. Shao, M. Ellington, J. Dicks, J. Carver, and L. Holland, “Electrolysis of water in the secondary school science laboratory with inexpensive microfluidics,” *J Chem Educ*, vol. 92, no. 1, pp. 116–119, 2015.

[16] P. Domachuk, K. Tsioris, F. G. Omenetto, and D. L. Kaplan, “Bio-microfluidics: Biomaterials and biomimetic designs,” *Adv Mater*, vol. 22, no. 2, pp. 249–260, 2010.

[17] I. A. Ges, R. L. Brindley, K. P. Currie, and F. J. Baudenbacher, “A microfluidic platform for chemical stimulation and real time analysis of catecholamine secretion from neuroendocrine cells,” *Lab on a Chip*, vol. 13, no. 23, pp. 4663–4673, 2013.

[18] T. Rodrigues, P. Schneider, and G. Schneider, “Accessing new chemical entities through microfluidic systems,” *Angewandte Chemie Int Ed*, vol. 53, no. 23, pp. 5750–5758, 2014.

[19] Z. Feng, G. Dan, and L. Qiong-Lin, “Advances of microfluidic technologies applied in bio-analytical chemistry,” *Chinese J Anal Chem*, vol. 44, no. 12, pp. 1942–1949, 2016.

[20] A. Khademhosseini, R. Langer, J. Borenstein, and J. P. Vacanti, “Microscale technologies for tissue engineering and biology,” *Proceedings of the National Academy of Sciences of the United States of America*, vol. 103, no. 8, pp. 2480–2487, 2006.

[21] M. Abkarian, M. Faivre, and H. A. Stone, “High-speed microfluidic differential manometer for cellular-scale hydrodynamics,” *Proceedings of the National Academy of Sciences of the United States of America*, vol. 103, no. 3, pp. 538–542, 2006.

[22] N. N. Barvitenko, M. Aslam, J. Filosa, E. Matteucci, M. Nikinmaa, A. Pantaleo, C. Saldanha, and O. K. Baskurt, “Tissue oxygen demand in regulation of the

behavior of the cells in the vasculature.," *Microcirculation*, vol. 20, no. 6, pp. 484–501, 2013.

[23] Q. Smith and S. Gerecht, "Going with the flow: microfluidic platforms in vascular tissue engineering," *Current Opinion in Chemical Engineering*, vol. 3, pp. 42–50, 2014.

[24] R. Blazej, B. Paegel, C. Emrich, and R. Mathies, *Microfabricated capillary array electrophoresis Implementation and applications.* sciencedirect, 2003.

[25] J. D. Harrison, R. D. Oleschuk, and P. Thibault, *Microfluidic systems for analysis of the proteome with mass spectrometry.* sciencedirect, 2003.

[26] Y. Zhao, D. Chen, H. Yue, J. B. French, J. Rufo, S. J. Benkovic, and T. Huang, "Lab-on-a-chip technologies for single-molecule studies," *Lab Chip*, vol. 13, no. 12, pp. 2183–2198, 2013.

[27] P. C. Chen, C. W. Pan, W. C. Lee, and K. M. Li, "Optimization of micromilling microchannels on a polycarbonate substrate," *International Journal of Precision Engineering and Manufacturing*, vol. 15, no. 1, pp. 149–154, 2014.

[28] D. P. Yen, Y. Ando, and K. Shen, "A cost-effective micromilling platform for rapid prototyping of microdevices," *Technology*, vol. 04, no. 04, pp. 234–239, 2016.

[29] A. Lashkaripour, R. Silva, and D. Densmore, "Desktop micromilled microfluidics," *Microfluidics and Nanofluidics*, vol. 22, no. 3, pp. 1–13, 2018.

[30] E. Carrilho, A. W. Martinez, and G. M. Whitesides, "Wax Printing – a Simple Micropatterning Process for Paper-based Microfluidics," *Analytical Chemistry*, vol. 81, no. 16, pp. 1–5, 2009.

[31] D. M. Cate, J. A. Adkins, J. Mettakoonpitak, and C. S. Henry, "Recent developments in paper-based microfluidic devices," *Analytical Chemistry*, vol. 87, no. 1, pp. 19–41, 2015.

[32] G. Xu, D. Nolder, J. Reboud, M. C. Oguike, D. A. van Schalkwyk, C. J. Sutherland, and J. M. Cooper, "Paper-Origami-Based Multiplexed Malaria Diagnostics from Whole Blood," *Angewandte Chemie - International Edition*, vol. 55, no. 49, pp. 15250–15253, 2016.

[33] A. W. Martinez, S. T. Phillips, and G. M. Whitesides, "Three-dimensional microfluidic devices fabricated in layered paper and tape," *Proceedings of the National Academy of Sciences*, vol. 105, no. 50, pp. 19606–19611, 2008.

[34] P. J. Kitson, M. H. Rosnes, V. Sans, V. Dragone, and L. Cronin, "Configurable 3D-Printed millifluidic and microfluidic 'lab on a chip' reactionware devices," *Lab on a Chip*, vol. 12, no. 18, pp. 1–6, 2012.

[35] K. B. Anderson, S. Y. Lockwood, S. R. Martin, and D. M. Spence, "A 3D printed fluidic device that enables integrated features," vol. 85, no. 12, pp. 5622–5626, 2013.

[36] A. I. Shallan, P. Smejkal, M. Corban, R. M. Guijt, and M. C. Breadmore, "Cost-effective three-dimensional printing of visibly transparent microchips within minutes," *Analytical Chemistry*, vol. 86, no. 6, pp. 3124–3130, 2014.

[37] L. M. Bellan, S. P. Singh, P. W. Henderson, T. J. Porri, H. G. Craighead, and J. A. Spector, "Fabrication of an artificial 3-dimensional vascular network using sacrificial sugar structures," *Soft Matter*, vol. 5, no. 7, pp. 1354–1357, 2009.

[38] D. Therriault, S. R. White, and J. A. Lewis, “Chaotic mixing in three-dimensional microvascular networks fabricated by direct-write assembly,” *Nature Materials*, vol. 2, no. 4, pp. 265–271, 2003.

[39] F. Burgoyne, “Rapid prototyping of branched microfluidics in PDMS using capillaries,” 2017.

[40] P. Geoghegan, N. Buchmann, C. Spence, S. Moore, and M. Jermy, “Fabrication of rigid and flexible refractive-index-matched flow phantoms for flow visualisation and optical flow measurements,” *Experiments in Fluids*, vol. 52, no. 5, pp. 1331–1347, 2012.

[41] A. E. Kamholz and P. Yager, “Theoretical analysis of molecular diffusion in pressure-driven laminar flow in microfluidic channels,” *Biophysical Journal*, vol. 80, no. 1, pp. 155–160, 2001.

[42] D. Gobby, P. Angeli, and A. Gavriilidis, “Mixing characteristics of T-type microfluidic mixers,” *Journal of Micromechanics and Microengineering*, vol. 11, no. 126, 2001.

[43] C. C. Hong, J. W. Choi, and C. H. Ahn, “A novel in-plane passive microfluidic mixer with modified Tesla structures,” *Lab on a Chip*, vol. 4, no. 2, pp. 109–113, 2004.

[44] D. Ahmed, X. Mao, B. K. Juluri, and T. J. Huang, “A fast microfluidic mixer based on acoustically driven sidewall-trapped microbubbles,” *Microfluidics and Nanofluidics*, vol. 7, no. 5, pp. 727–731, 2009.

[45] M. A. Unger, H.-p. Chou, T. Thorsen, A. Scherer, S. R. Quake, M. A. Unger, H.-p. Chou, T. Thorsen, A. Scherer, and S. R. Quake, “Monolithic Microfabricated

Valves and Pumps by Multilayer Soft Lithography," *Science*, vol. 288, no. 5463, pp. 113–116, 2000.

[46] D. E. Furst, R. Fleischmann, E. Kopp, M. Schiff, C. K. Edwards, A. Solinger, and M. Macri, "A phase 2 dose-finding study of pegylated recombinant methionyl human soluble tumor necrosis factor type I in patients with rheumatoid arthritis," *Journal of Rheumatology*, vol. 32, no. 12, pp. 2303–2310, 2005.

[47] G. C. Biswas, T. Watanabe, E. T. Carlen, M. Yokokawa, and H. Suzuki, "Switchable Hydrophobic Valve for Controlled Microfluidic Processing," *ChemPhysChem*, vol. 17, no. 6, pp. 817–821, 2016.

[48] S. M. Mitrovski and R. G. Nuzzo, "An electrochemically driven poly(dimethylsiloxane) microfluidic actuator: Oxygen sensing and programmable flows and pH gradients," *Lab on a Chip*, vol. 5, no. 6, pp. 634–645, 2005.

[49] Z. M. Redha, S. J. Baldock, P. R. Fielden, N. J. Goddard, B. J. Brown, B. G. Haggett, R. Andres, and B. J. Birch, "Hybrid microfluidic sensors fabricated by screen printing and injection molding for electrochemical and electrochemiluminescence detection," *Electroanalysis*, vol. 21, no. 3-5, pp. 422–430, 2009.

[50] J. L. Delaney, C. F. Hogan, J. Tian, and W. Shen, "Electrogenerated chemiluminescence detection in paper-based microfluidic sensors," *Analytical Chemistry*, vol. 83, no. 4, pp. 1300–1306, 2011.

[51] N. Levy, "The use of animal as models: Ethical considerations," *International Journal of Stroke*, vol. 7, no. 5, pp. 440–442, 2012.

[52] A. R. Perestrelo, A. C. Águas, A. Rainer, and G. Forte, “Microfluidic organ/body-on-a-chip devices at the convergence of biology and microengineering,” *Sensors (Switzerland)*, vol. 15, no. 12, pp. 31142–31170, 2015.

[53] J. B. Lee and J. H. Sung, “Organ-on-a-chip technology and microfluidic whole-body models for pharmacokinetic drug toxicity screening,” *Biotechnology Journal*, vol. 8, no. 11, pp. 1258–1266, 2013.

[54] H. Kimura, Y. Sakai, and T. Fujii, “Organ/body-on-a-chip based on microfluidic technology for drug discovery,” *Drug Metabolism and Pharmacokinetics*, vol. 33, no. 1, pp. 43–48, 2018.

[55] A. M. M. M.-Z. Dongeun Huh, Benjamin D. Matthews and D. E. I. Hong Yuan Hsin, “Reconstituting Organ-Level Lung,” *Science*, vol. 328, no. June, pp. 1662–1669, 2010.

[56] B. Zhang, M. Montgomery, M. D. Chamberlain, S. Ogawa, A. Korolj, A. Pahnke, L. A. Wells, S. Masse, J. Kim, L. Reis, A. Momen, S. S. Nunes, A. R. Wheeler, K. Nanthakumar, G. Keller, M. V. Sefton, and M. Radisic, “Biodegradable scaffold with built-in vasculature for organ-on-a-chip engineering and direct surgical anastomosis,” *Nature Materials*, vol. 15, no. 6, pp. 669–678, 2016.

[57] J. Sutton and J. Sutton, *Enzymes.* springer, 1998.

[58] A. Liljas, L. Liljas, M. Ash, G. Lindblom, P. Nissen, and M. Kjeldgaard, *Enzymes.* worldscientific, 2016.

[59] P. C. Engel and P. C. Engel, *Inhibitors, activators and inactivators.* springer, 1981.

[60] A. R. Schulz and A. R. Schulz, *Preface.* cambridge, 1994.

[61] H. Bisswanger, *Introduction.* wiley, 2005.

[62] D. Liu and C. Walden, “A spectrophotometric assay for cellobiase,” *Anal Biochem*, vol. 31, no. 1, pp. 211–217, 1969.

[63] F. Heinz, S. Reckel, and J. R. Kalden, “A new spectrophotometric assay for enzymes of purine metabolism,” *Enzyme*, vol. 24, no. 4, pp. 247–254, 1979.

[64] P. C. Jocelyn, *Spectrophotometric assay of thiols*, vol. 143. sciencedirect, 1987.

[65] D. G. Fatkins and W. Zheng, “A spectrophotometric assay for histone deacetylase 8,” *Anal Biochem*, vol. 372, no. 1, pp. 82–88, 2008.

[66] S. Elavarthi and B. Martin, *Spectrophotometric Assays for Antioxidant Enzymes in Plants*, vol. 639. springer, 2010.

[67] B. Chance, *Spectrophotometric Assays.* sciencedirect, 2013.

[68] H. Song and R. F. Ismagilov, “Millisecond Kinetics on a Microfluidic Chip Using Nanoliters of Reagents,” *Journal of the American Chemical Society*, vol. 125, no. 47, pp. 14613–14619, 2003.

[69] Z. Han, W. Li, Y. Huang, and B. Zheng, “Measuring Rapid Enzymatic Kinetics By Amperometric Method in Droplet-Based and Pneumatic Valves Controlled,” *Advanced Materials*, vol. 81, no. 14, pp. 2–4, 2009.

[70] R. N. Palchesko, L. Zhang, Y. Sun, and A. W. Feinberg, “Development of polydimethylsiloxane substrates with tunable elastic modulus to study cell mechanobiology in muscle and nerve,” *Plos ONE*, vol. 7, no. 12, p. e51499, 2012.

[71] J. Choi, D. Park, and T. Oh, “Variation of elastic stiffness of polydimethylsiloxane (PDMS) stretchable substrates for wearable packaging applications,” *J Microelectron Packag Soc*, vol. 21, no. 4, pp. 125–131, 2014.

[72] I. Johnston, M. DK, C. Tan, and M. Tracey, “Mechanical characterization of bulk sylgard 184 for microfluidics and microengineering,” *J Micromech Microeng*, vol. 24, no. 3, p. 035017, 2014.

[73] E. Yim, R. M. Reano, S. W. Pang, A. F. Yee, C. S. Chen, and K. W. Leong, “Nanopattern-induced changes in morphology and motility of smooth muscle cells,” *Biomaterials*, vol. 26, no. 26, pp. 5405–5413, 2005.

[74] G. K. Toworfe, R. J. Composto, C. S. Adams, I. M. Shapiro, and P. Ducheyne, “Fibronectin adsorption on surface-activated poly(dimethylsiloxane) and its effect on cellular function,” *J Biomed Mater Res A*, vol. 71A, no. 3, pp. 449–461, 2004.

[75] D. Fuard, T. T, S. Decossas, P. Tracqui, and P. Schiavone, “Optimization of poly-di-methyl-siloxane (PDMS) substrates for studying cellular adhesion and motility,” *Microelectronic Engineering*, vol. 85, no. 5-6, pp. 1289–1293, 2008.

[76] W. Bae, K. Kim, S. Kim, H. Cho, S. Hong, J. Lee, T. Hwang, and S. Kim, “AB222. comparison of biocompatibility between PDMS and PMMA as packaging materials for the intravesical implantable device: changes of macrophage and macrophage migratory inhibitory factor,” *Transl Androl Urology*, vol. 3, no. Suppl 1, p. AB222, 2014.

[77] T. Matsumoto, Y. Koinuma, K. Waki, A. Kishida, T. Furuzono, I. Maruyama, and M. Akashi, “Novel functional polymers: Poly(dimethylsiloxane)–polyamide

multiblock copolymer. IV. gas permeability and thermomechanical properties of aramid–silicone resins," *J Appl Polym Sci*, vol. 59, no. 7, pp. 1067–1071, 1996.

[78] J. Chen, D. Chen, Y. Xie, X. Chen, K. Wang, D. Cui, H. Du, and Z. Wang, "Bubble generation and mechanism in polydimethylsiloxane based polymerase chain reaction chip," *Appl Phys Lett*, vol. 106, no. 5, p. 053507, 2015.

[79] X. Ren, H. Lu, J. G. Zhou, P. Chong, W. Yuan, and M. Noh, "Porous polydimethylsiloxane as a Gas–Liquid interface for microfluidic applications," *J Microelectromech S*, vol. 26, no. 1, pp. 120–126, 2017.

[80] L. Zhao, J. Lee, and P. N. Sen, "Long-term retention of hydrophilic behavior of plasma treated polydimethylsiloxane (PDMS) surfaces stored under water and Luria-Bertani broth," *Sensors and Actuators*, vol. 181, pp. 33–42, 2012.

[81] Y. Chen, W. Pei, R. Tang, S. Chen, and H. Chen, "Conformal coating of parylene for surface anti-adhesion in polydimethylsiloxane (PDMS) double casting technique," *Sensors Actuators Phys*, vol. 189, pp. 143–150, 2013.

[82] B. Larson, S. Gillmor, J. Braun, C. LE, D. Savage, F. Denes, and M. Lagally, "Long-Term reduction in poly(dimethylsiloxane) surface hydrophobicity via Cold-Plasma treatments," *Langmuir*, vol. 29, no. 42, pp. 12990–12996, 2013.

[83] M. Yao and J. Fang, "Hydrophilic PEO-PDMS for microfluidic applications," *Journal of Micromechanics and Microengineering*, vol. 22, no. 2, p. 025012, 2012.

[84] S. Bashir, J. M. Rees, and W. B. Zimmerman, "Simulations of microfluidic droplet formation using the two-phase level set method," *Chem Eng Sci*, vol. 66, no. 20, pp. 4733–4741, 2011.

[85] S. Bashir, X. Solvas, M. Bashir, J. Rees, and W. Zimmerman, "Dynamic wetting in microfluidic droplet formation," *Biochip J*, vol. 8, no. 2, pp. 122–128, 2014.

[86] DowDuPont, Inc. Midlan, Michigan, USA.

[87] C. J. McDonald, D. Duffy, J. Anderson, D. Chiu, H. Wu, O. Schueller, and G. Whitesides, "Fabrication of microfluidic systems in poly(dimethylsiloxane)," *Electrophoresis*, vol. 21, no. 1, pp. 27–40, 2000.

[88] C. J. McDonald and G. M. Whitesides, "Poly(dimethylsiloxane) as a material for fabricating microfluidic devices," *Accounts of Chemical Research*, vol. 35, no. 7, pp. 491–499, 2002.

[89] H. B. Jo, V. L. Lerberghe, K. Motsegood, and D. Beebe, "Three-dimensional micro-channel fabrication in polydimethylsiloxane (PDMS) elastomer," *Journal of Microelectromechanical Systems*, vol. 9, no. 1, pp. 76–81, 2000.

[90] J. Lee, C. Park, and G. M. Whitesides, "Solvent compatibility of Poly(dimethylsiloxane)-Based microfluidic devices," *Langmuir : the ACS journal of surfaces and colloids*, vol. 75, no. 23, pp. 6544–6554, 2003.

[91] R. Dangla, F. Gallaire, and C. N. Baroud, "Microchannel deformations due to solvent-induced PDMS swelling," *Lab on a Chip*, vol. 10, no. 21, pp. 2972–2978, 2010.

[92] T. J. Renckens, D. Janeliunas, H. van Vliet, J. H. van Esch, G. Mul, and M. T. Kreutzer, "Micromolding of solvent resistant microfluidic devices," *Lab on a Chip*, vol. 11, no. 12, pp. 2035–2038, 2011.

[93] B. Kim, L. Hong, Y. Chung, D. Kim, and C. Lee, "Solvent-Resistant PDMS microfluidic devices with hybrid Inorganic/Organic polymer coatings," *Advanced Functional Material*, vol. 19, no. 23, pp. 3796–3803, 2009.

[94] J. Lee, J. M. Kim, and H. H. Lee, "Surface modification of poly(dimethylsiloxane) for retarding swelling in organic solvents.," *Langmuir Acs J Surfaces Colloids*, vol. 22, no. 5, pp. 2090–5, 2006.

[95] A. R. Abate, D. Lee, T. Do, C. Holtze, and D. A. Weitz, "Glass coating for PDMS microfluidic channels by sol–gel methods," vol. 8, no. 4, pp. 516–518, 2008.

[96] R. L. Mays, M. D. Dickey, and J. Genzer, "Microfluidic channels fabricated from poly(vinylmethylsiloxane) networks that resist swelling by organic solvents," vol. 13, no. 22, pp. 4317–4320, 2013.

[97] A. Arostegui, M. Sarrionandia, J. Aurrekoetxea, and I. Urrutibeascoa, "Effect of dissolution-based recycling on the degradation and the mechanical properties of acrylonitrile–butadiene–styrene copolymer," *Polym Degrad Stabil*, vol. 91, no. 11, pp. 2768–2774, 2006.

[98] E. J. McCullough and V. K. Yadavalli, "Surface modification of fused deposition modeling ABS to enable rapid prototyping of biomedical microdevices," *Journal of Materials Processing Technology*, vol. 213, pp. 947–954, jun 2013.

[99] H. Gao, D. V. Kaweesa, J. Moore, and N. A. Meisel, "Investigating the Impact of Acetone Vapor Smoothing on the Strength and Elongation of Printed ABS Parts," *JOM*, vol. 69, pp. 580–585, mar 2017.

[100] S. Ahn, M. Montero, D. Odell, S. Roundy, and P. K. Wright, “Anisotropic material properties of fused deposition modeling ABS,” *Rapid Prototyping J*, vol. Volume 8, no. Issue 4, pp. 248–257, 2002.

[101] S. Raut, V. S. Jatti, N. K. Khedkar, and T. Singh, “Investigation of the effect of built orientation on mechanical properties and total cost of FDM parts,” *Procedia Mater Sci*, vol. 6, pp. 1625–1630, 2014.

[102] S. Ziemian, M. Okwara, and C. Ziemian, “Tensile and fatigue behavior of layered acrylonitrile butadiene styrene,” *Rapid Prototyping J*, vol. Volume 21, no. Issue 3, pp. 270–278, 2015.

[103] J. Lee and A. Huang, “Fatigue analysis of FDM materials,” *Rapid Prototyping J*, vol. Volume 19, no. Issue 4, pp. 291–299, 2013.

[104] SolidWorks 2015. Dassault Systèmes SE, Vélizy-Villacoublay, France.

[105] Stratasys Ltd. Eden Prairie, Minnesota, USA.

[106] Stratasys, SR-30 Soluble Support Material. http://www.stratasys.com/materials/material-safety-data-sheets/fdm/other-items.

[107] Stratasys, Ecoworks tablets. http://www.stratasys.com/materials/material-safety-data-sheets/fdm/support-materials.

[108] Laboratoires Servier. http://sevierlab.vet.cornell.edu/resources/Chemical-Resistance-Chart-Detail.pdf, Last accessed: 25/09/2017.

[109] Thermo Fisher Scientific. https://tools.thermofisher.com/content/sfs/brochures/D20480.pdf.

[110] Instron. Illinois Tool Works, Glenview, Illinois, USA.

[111] MARK-10. Copiague, New Yrok, USA.

[112] Smooth-On. Macungie, Pennsylvania, USA.

[113] R. L. Dean, “Kinetic studies with alkaline phosphatase in the presence and absence of inhibitors and divalent cations,” *Biochem Mol Biol Edu*, vol. 30, no. 6, pp. 401–407, 2002.

[114] G. Chaudhuri, S. Chatterjee, K. Ramasamy, and W. R. Thilagaraj, “Kinetic behaviour of calf intestinal alkaline phosphatase with p NPP,” vol. 50, no. February, pp. 64–71, 2013.

[115] J. Campbell, *Chapter 5 Phototransistors for Lightwave Communications*, vol. 22. sciencedirect, 1985.

[116] R. Kraus and D. Ryan, “Advances in heat-shrink technology,” *Ieee Electr Insul M*, vol. 4, no. 3, pp. 31–34, 2017.

[117] Smooth-On. Macungie, Pennsylvania, USA.

[118] A. I. Biggs, “A Spectrophotometric Determination of the Dissociation Constants of p-nitrophenol,” pp. 800–802, 1954.

[119] Microchip Technology Inc. Chandler, Arizona, USA.

[120] Future Technology Devices International Ltd. Glasgow, Scotland, UK.

[121] Eagle 8.2.2. Autodesk, Inc., Mill Valley, California, USA.

[122] LPKF Laser & Electronics AG. Garbsen, Germany.

[123] Epilog Laser. Golden, Colorado, US.

[124] Matlab 2016b. MathWorks, Inc., Natic, Massachusetts, USA.

[125] ZJchao Peristaltic pmup. https://www.amazon.co.uk/, Last accessed: 29/09/2017.

[126] BioTek Instruments, Inc. Winooski, Vermont, USA.

[127] Thermo Fisher Scientific. Waltham, Massachusetts, USA.

[128] TAL Technologies Inc. Philadelphia, Pennsylvania, USA.

[129] Microsoft. Redmond, Washington, USA.

[130] T. Sherman, "On connecting large vessels to small. the meaning of murray's law.," *The Journal of General Physiology*, vol. 78, pp. 431–453, 1981.

[131] P. R. Painter, P. Edén, and H. Bengtsson, "Pulsatile blood flow, shear force, energy dissipation and murray's law," *Theoretical Biology and Medical Modelling*, vol. 3, no. 1, pp. 1–10, 2006.

Appendices

Appendix A

Publications

- A. Buchoux, P. valluri, S. Smith, A.A. Stokes, P.H. Hoskins, V. Sboros, "Manufacturing of microcirculation phantoms using rapid prototyping technologies", *IEEE EMBC*, Milan, 2015.
- A. Buchoux, S. Smith, D.J. Clarke, A.A. Stokes "Development of a 3D microfluidic Lab on a Chip for light spectrometry analysis of enzyme kinetics", *IEEE NIHPOC*, Cancun, 2016.
- A. Buchoux, E.O. Blair, A. Tsiamis, J.R.K. Marland, S. Smith, "A Low Cost Patternable Packaging Technology for Biosensors", *IEEE DTIP*, Bordeaux, 2017.

Appendix B

Chapter 3: Additional characterisation and process demonstration

B.1 Rate of evaporation of acetone at room conditions

Although the manufacturing process requires little labour time, waiting for the acetone to evaporate can be time consuming and knowing when the device is ready is difficult and mostly based on experience. As part of the manufacturing process, it is therefore important to be able to predict when the device is be ready, based on the dimensions of the fluidic device.

The experiment is designed to study the time it takes for the acetone to evaporate from the PDMS at room conditions. Two tests are performed. First the rate of evaporation from five cubes of PDMS is measured. The length a of the cubes ranges from $a =$

10 mm to $a = 30$ mm by increments of 5 mm. The objective is to see the relation between the rate of evaporation and a decreasing surface to volume ratio. The second test records the rate of evaporation of cuboids of increasing thickness h. The thickness of the samples are 5, 10, 15 and 20 mm with a square base of 20 mm. This second test is important to measure the relation between the thickness of the material and the rate of evaporation. To measure the evaporation time, the acetone loss is recorded by measuring the weight of the PDMS samples over time using a digital scale. All the samples are left in acetone for 48 h before the experiment. The first mass reading is done when the samples are removed from the bath after being wiped. Then a measurement of the mass is taken every 30 s and logged into a spreadshseet until the weight is stable. The measure is taken with a PAS214C scale from Fisher Scientific [127] (resolution of 0.1 mg), via a RS232 serial interface and sent to a PC every 30 s. Each measurement is read by a data collection software, BC-Wedge [128], and automatically logged into Excel [129]. Dimensions as well as weight and swelling by weight are summarized in Table B.1 for the cubic samples and Table B.2 for the cuboid samples. When the weight of the samples reaches 1 % of their final weight, the time is recorded. This is to avoid errors due to environment disturbances such as vibrations from nearby lab user or the equipment. The mean swelling of PDMS in acetone for all the samples is 39.5 % (2.0

Table B.1: Characteristics of the cubic samples

Sample (a)	10	15	20	25	30
Samples before acetone bath					
x (mm)	9.6	14.4	19.3	24.3	29.2
y(mm)	9.6	14.6	19.3	24.3	29.1
z (mm)	10.5	14.6	20.2	24.9	30.3
Surface (mm^2)	588	1256	2304	3601	5267
Volume (mm^3)	970	3070	7520	14700	25750
Ratio V:S (mm)	0.606	0.410	0.306	0.245	0.204
Weight (g)	0.97	3.12	7.70	14.78	25.94
Samples after acetone bath					
x (mm)	10.8	16.0	21.6	27.0	32.4
y (mm)	10.8	16.0	21.6	27.0	32.2
x (mm)	11.7	16.5	22.7	27.7	33.7
Surface (mm^2)	719	1552	2847	4374	6441
Volume (mm^3)	1365	4224	10591	20193	35159
Weight (g)	1.28	4.10	10.15	19.39	32.98
Weight of acetone (g)	0.29	0.96	2.44	4.63	8.05
Swelling by volume (%)	40.2	37.5	40.8	37.3	36.5
Evaporation time (min)	618.5	1450	2680.5	4013.5	5808.5

Table B.2: Characteristics of the cuboid samples

Sample (h)	5	10	15	20
Samples before the acetone bath				
x (mm)	19.3	19.3	19.2	19.3
y (mm)	19.2	19.3	19.2	19.3
z (mm)	5.3	10.8	15.6	20.2
Surface (mm^2)	1149	1579	1935	2304
Volume (mm^3)	1960	4020	5750	7520
Ratio V:S (mm)	0.586	0.393	0.337	0.306
Weight (g)	1.98	4.08	5.88	7.70
Samples after acetone bath				
x (mm)	21.5	21.5	21.5	21.6
y (mm)	21.5	21.5	21.5	21.6
z (mm)	6.0	12.3	17.5	22.7
Surface (mm^2)	1978	2113	2225	2847
Volume (mm^3)	2774	5686	8089	10591
Weight (g)	2.58	5.35	7.69	10.15
Weight of acetone (g)	0.60	1.28	1.77	2.44
40.2 Swelling by volume (%)	41.3	41.5	40.7	40.8
Evaporation time (min)	474	1487.5	2098.5	2680.5

% SD), by weight. Figure B.1 shows a graph of the evaporation time with regard to the Volume:Surface ratio. The results show a correlation between the ratio and the evaporation time for cubes and cuboids. As the ratio Volume:Surface increases, the evaporation time reduces, regardless of the shape of the block of PDMS.

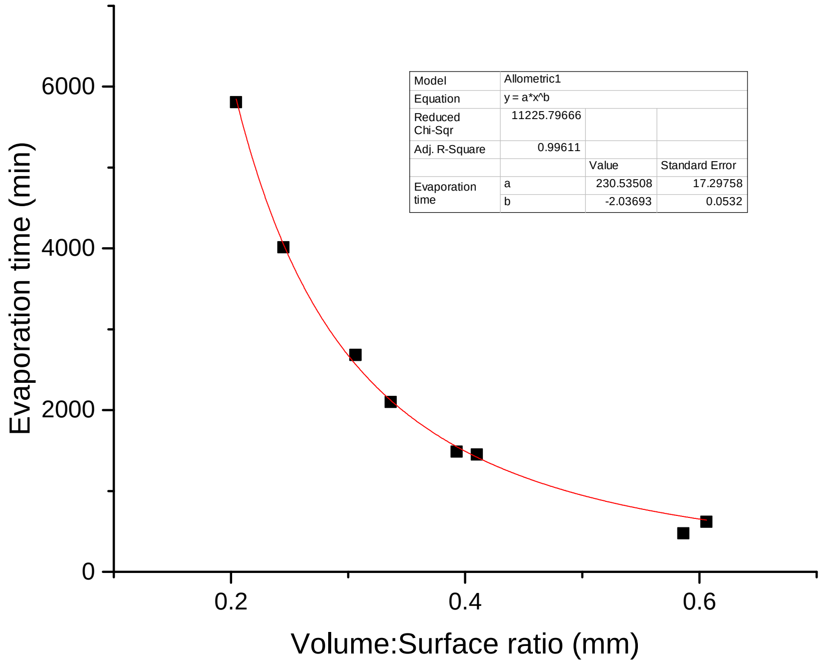

Figure B.1: Graph showing the correlation between the evaporation time and the ratio Volume:Surface ratio, irrespective of the shape of the samples

B.2 Circulatory flow phantom

B.2.1 Introduction

A circulatory flow phantom was manufactured as a practical example using the manufacturing process. Microcirculation networks consist of vessels with a diameter less than 100 µm, including arterioles, capillaries and venules. There is considerable interest in understanding the role of microcirculation in terms of hemodynamics and in the development of techniques to measure perfusion. Phantoms mimic the geometry and physical properties of the tissues, allowing comparison of properties measured using imaging with known properties in the phantom. These are widely used in medical imaging. Optically transparent phantoms may be used with optical measurement techniques to explore the local hemodynamics in detail. Optical measurement techniques include particle image velocimetry, laser Doppler anemometry and video imaging.

B.2.2 Design of the phantom

The phantom, at a scale of 150:1, consists of an inlet arteriole 3 mm in diameter, down to a capillary bed, made of channels of 1.5 mm diameter. The network is then mirrored to an outlet venule of 3 mm in diameter. The dimensions of the phantom are 154 mm long, 54 mm wide and 33 mm thick. The branching of the network is designed following Murray's law [130], see Eq. B.1, which describes the radius of daughter channels in relation to the radius of a mother channel. Murray's law is defined by the minimum cost necessary for the blood to move through the cardiovascular system, excluding main arteries [131]. Figure B.2 shows a simple diagram representing Murray's law.

$$r_m^3 = r_{d1}^3 + r_{d2}^3 + ... + r_{dn}^3 \tag{B.1}$$

Where:

r_m^3 : radius of the mother channel

r_{d1}^3 : radius of the daughter channel 1

r_{d2}^3 : radius of the daughter channel 2

r_{dn}^3 : radius of the daughter channel n

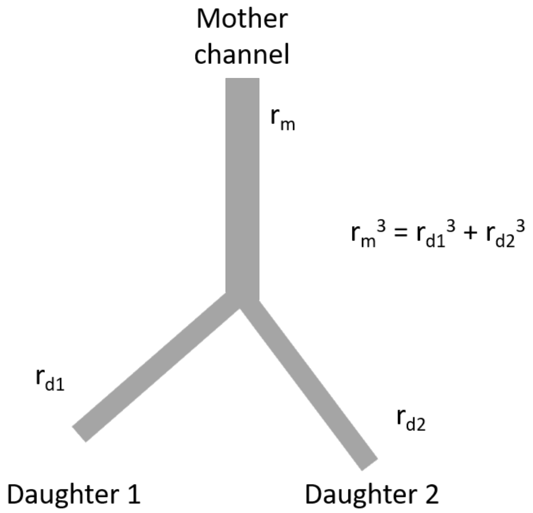

Figure B.2: Illustration of Murray's law

Figure B.3 shows a CAD view of the network without the casing. The device is manufactured using Sylgard 184 [86] with a 10:1 ratio, and cured at 60 °C for two hours. The device was left in acetone for 48 hours before the liquefied ABS was flushed. It took a further 48 hours for the acetone to evaporate. Water droplets, representing the red blood cells, in sunflower oil is used to demonstrate the flow pattern in the phantom.

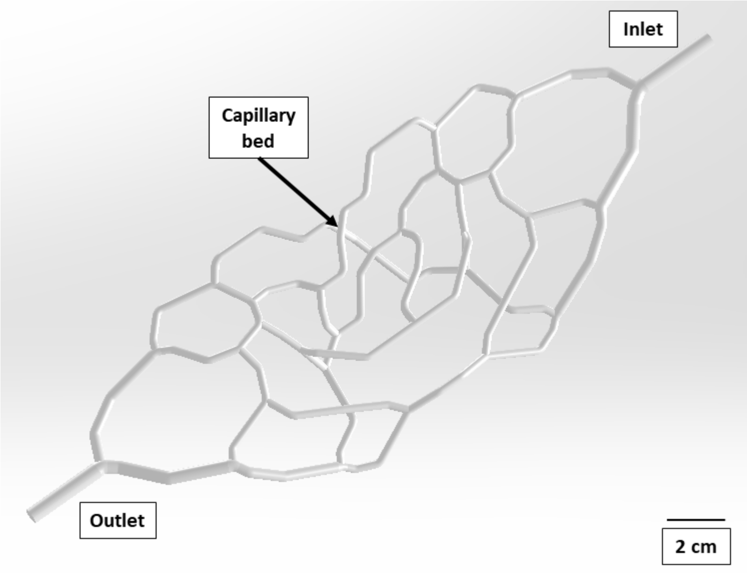

Figure B.3: CAD representation of the blood flow phantom

Figure B.4 shows a schematic of the experimental setup. It consists of two centrifugal pumps, one for the oil at 0.6 ml/s and one for the dyed water at 0.3 ml/s, the phantom and a reservoir where the oil and water are contained, separated by specific gravity. The pump inputs are placed at different depths in the reservoir, making sure they pump the intended fluid only. A unique return pipe is placed at the bottom of the reservoir, opposite to the intakes.

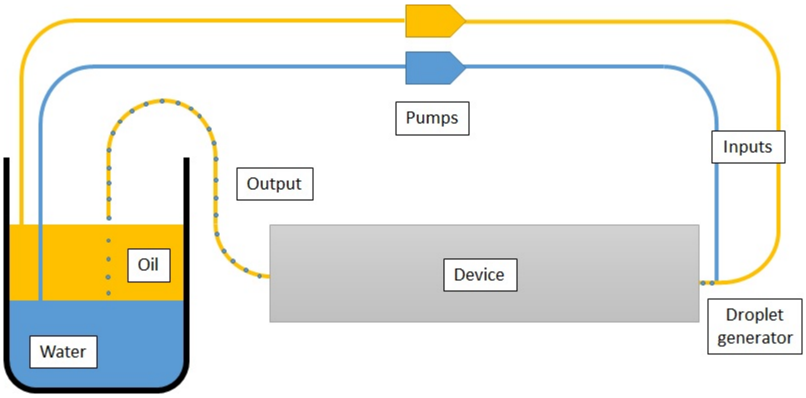

Figure B.4: Experimental setup of the blood flow phantom

B.2.3 Discussion

Figure B.5 a) shows a wide view of the phantom. Videos from iPhone 6, recording at 120 frames per second, were used to study the flow (video can be found in supplemental CD). The influence of the bifurcation angle on the flow rate of the daughter channels is observed. The flow is faster and contains a higher number of droplets when the bifurcation angle is reduced. The flow appears significantly slower and the number of droplets significantly scarcer in daughter channels with a bifurcation angle near 90°. From a close up view of the capillary bed, capillaries closer to main arterioles look as if the flow rate is higher than in channels further away, see Figure B.5 b). Further observations form Figure B.5 a) reveals a droplet breaking apart at the first bifurcation, suggesting the design of the droplet generator is not suited for the device. Droplets further down the network appear to be smaller that the droplet observed directly after the first bifurcation.

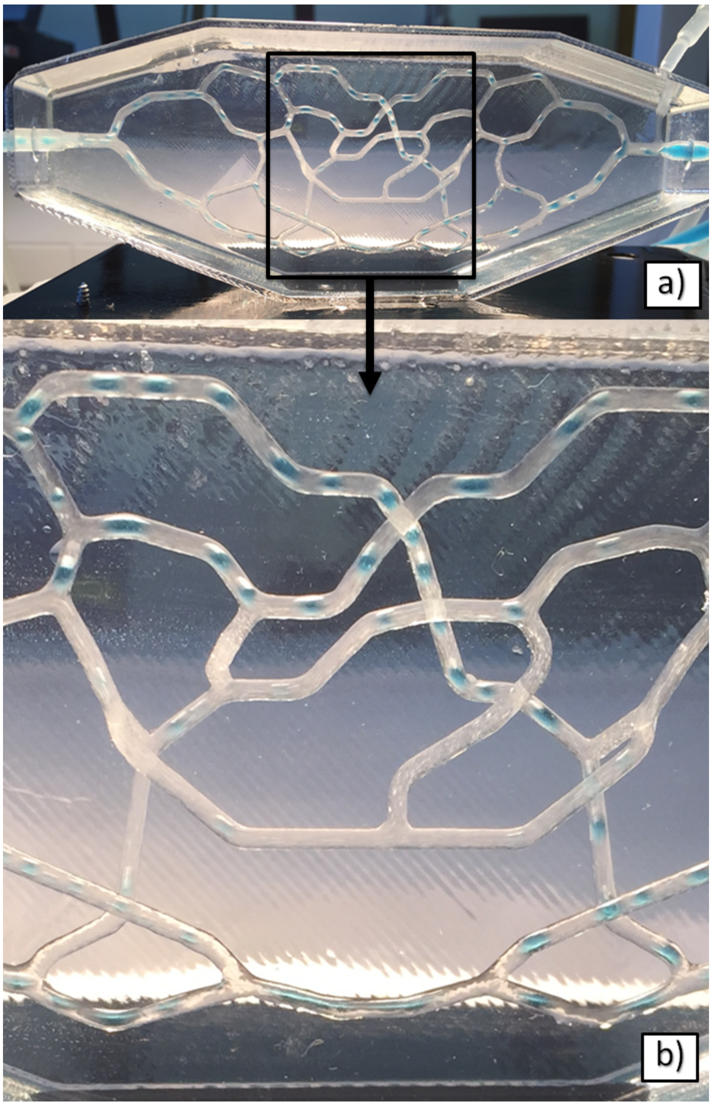

Figure B.5: a) General view of the vascular network showing the flow of blue dyed water droplets (RBC analogue) in sunflower oil (plasma analogue). b) Detailed view of the capillary bed

This work shows an application to the lost core manufacturing method for complex 3D fluidic device. The phantom can potentially be used for the study of hemodynamics. The design of the network could be based on data from biomedical imaging, reflecting a more accurate flow. Such a device would be suitable for patient specific study. Additionally, the droplet generator needs to be improved, to create smaller, more regularly sized droplets.

Appendix C

Chapter 4: Additional Work and Raw Data

C.1 Proportional valve

Table C.1: Data from the pneumatic valve characterisation

Pressure (mBar)	#1 (g/s)	#2 (g/s)	#3 (g/s)	Mean (g/s)	SD
0	4.609	4.785	4.768	4.721	0.097
17	4.621	4.773	4.787	4.727	0.092
34	3.666	3.744	3.631	3.680	0.058
52	2.158	2.385	2.489	2.344	0.169
69	1.317	1.184	1.371	1.291	0.096
86	0.980	0.791	0.789	0.853	0.110
103	0.486	0.525	0.583	0.531	0.049
121	0.325	0.347	0.299	0.324	0.024
138	0.150	0.166	0.176	0.164	0.013
155	0.051	0.023	0.034	0.036	0.014
172	0.016	0.001	0.014	0.010	0.008
190	0	0	0	0	0

C.2 Photometric sensor

C.2.1 Electronics

- UV LED: Bivar LED3-UV-400-30, 400 nm peak emissivity.
- UV PT: Visahy TEPT4400, 570 nm peak sensitivity (0.30 sensitivity at 400 nm).

C.2.2 Photometric sensor calibration data

Table C.2: Photometric sensor voltage reading for a resistor of 10 kΩ on the PT

[S] (mM)	68 Ω	150 Ω	220 Ω	330 Ω	390 Ω
0.225	2.981	3.379	3.515	3.685	3.741
0.1125	2.326	2.947	3.19	3.415	3.503
0.05625	1.855	2.623	2.933	3.224	3.329
0.028125	1.543	2.417	2.787	3.101	3.225
0.000879	1.326	2.185	2.569	2.939	3.092

Table C.3: Photometric sensor voltage reading for a resistor of 22 kΩ on the PT

[S] (mM)	68 Ω	150 Ω	220 Ω	330 Ω	390 Ω
0.225	1.991	2.740	3.034	3.307	3.532
0.1125	0.980	1.949	2.423	2.807	2.969
0.05625	0.350	1.443	1.968	2.461	2.665
0.028125	0.087	1.141	1.718	2.249	2.470
0.000879	0.071	0.850	1.411	1.995	2.233

Table C.4: Photometric sensor voltage reading for a resistor of 27 kΩ on the PT

[S] (mM)	68 Ω	150 Ω	220 Ω	330 Ω	390 Ω
0.225	1.678	2.504	2.856	3.160	3.275
0.1125	0.592	1.644	2.107	2.598	2.782
0.05625	0.077	1.077	1.648	2.171	2.399
0.028125	0.041	0.768	1.354	1.960	2.213
0.000879	0.055	0.423	0.996	1.690	1.922

Table C.5: Photometric sensor voltage reading for a resistor of 33 kΩ on the PT

[S] (mM)	68 Ω	150 Ω	220 Ω	330 Ω	390 Ω
0.225	1.272	2.155	2.616	2.909	3.119
0.1125	0.142	1.222	1.716	2.238	2.514
0.05625	0.054	0.653	1.278	1.788	2.107
0.028125	0.044	0.411	0.972	1.595	1.857
0.000879	0.041	0.191	0.727	1.359	1.602

Table C.6: Run of 5 voltage readings with 33 kΩ resistor on the PT and 150 Ω resistor on the UV LED

	Voltage (V)				
[S] (mM)	#1	#2	#3	#4	#5
0.250	2.260	2.260	2.263	2.282	2.246
0.225	2.037	2.065	2.091	2.103	2.065
0.2	1.844	1.895	1.879	1.878	1.887
0.18	1.717	1.684	1.713	1.700	1.686
0.15	1.478	1.536	1.452	1.466	1.455
0.129964	1.345	1.338	1.350	1.322	1.291
0.1125	1.164	1.151	1.203	1.143	1.102
0.09	0.976	0.973	0.957	1.000	0.972
0.075	0.831	0.840	0.851	0.833	0.813
0.05625	0.635	0.641	0.622	0.601	0.630
0.028125	0.347	0.344	0.408	0.344	0.325
0.014063	0.228	0.248	0.209	0.210	0.181
0.000879	0.124	0.107	0.112	0.112	0.097

C.3 Potential designs

This section presents noteworthy designs that where manufactured early on in the project but were never further developed.

C.3.1 Non-return valve

A non-return valve is a fluid equivalent to a diode. It will let the fluid travel in one direction but will stop it if flowing in the opposite direction. The mould consists of a block of ABS with an elongated cavity on the top, going almost all the way through the block, angled at 25°. Two channels with a diameter of 1.5 mm were extending on each sides, perpendicular to the cavity. As seen in Figure C.1, the resulting device had a small chamber with a lip of PDMS extending from the top. The protruding feature can be bent back and forth to either close or leave open the channel. The design was not extensively explored and only worked with high flow due to stiffness of PDMS. Further experiment could evaluate the effect of reducing the stiffness of PDMS. Refining the design should also be considered.

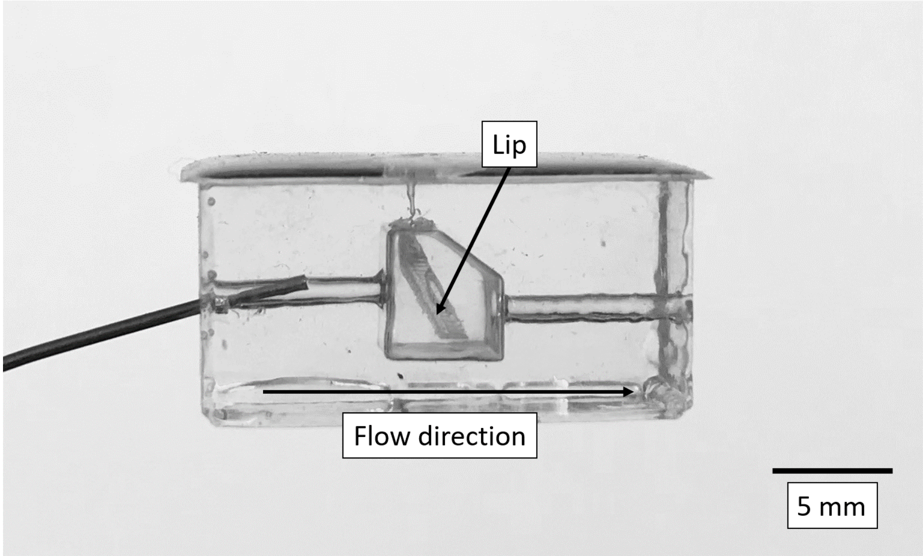

Figure C.1: Example of a non-return valve design

C.3.2 Stretchable and bendable channel

Figure C.2 shows a simple device with a channel of diameter of 1 mm, starting from center of the device. It then bent towards the surface of the device and ran parallel to the surface, with a thickness of PDMS of only 0.5 mm. If the device were to be bent, the channel would stretch and change its cross section If the channel was filled with a conductive liquid it could be used as a mechanical sensor.

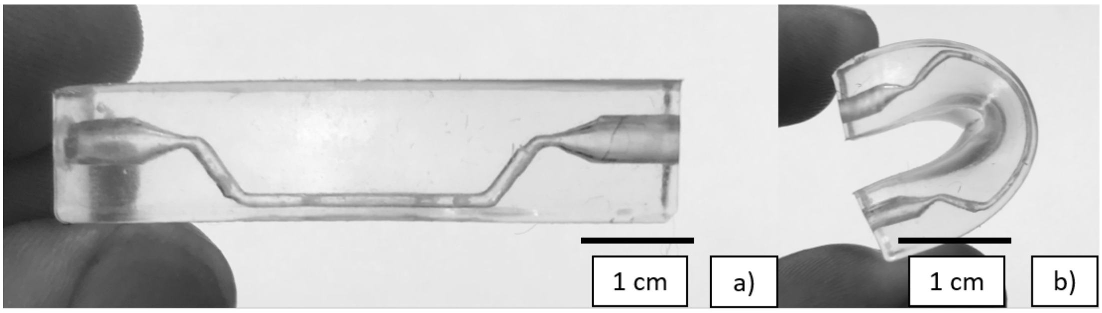

Figure C.2: Example of a channel with changing dimensions when a force is applied

C.3.3 Solenoid or heating element

Figure C.3 shows a simple microfluidic device with an embedded coil. The coil was wound around a channel with a diameter of 1.5 mm, creating either an electromagnet or a heating element. The generated electromagnetic field could be used to interact with ferromagnetic elements present in the channel, moving or separating fluids or be used as a sensor. As a heating element, it could be used to change the local chemistry, by affecting heat sensitive chemicals.

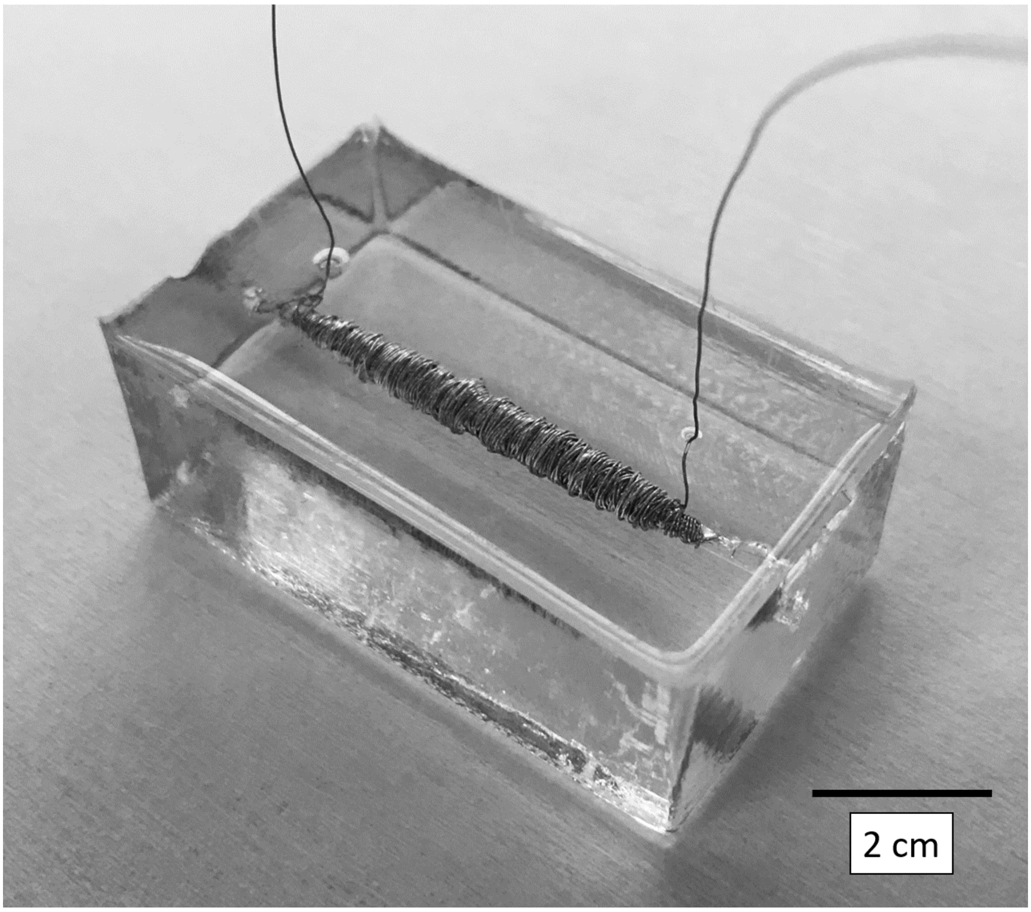

Figure C.3: Example of a channel surrounded by a copper coil

Appendix D

Chapter 5: PCB, BOM ans Raw Data

D.1 PCB design

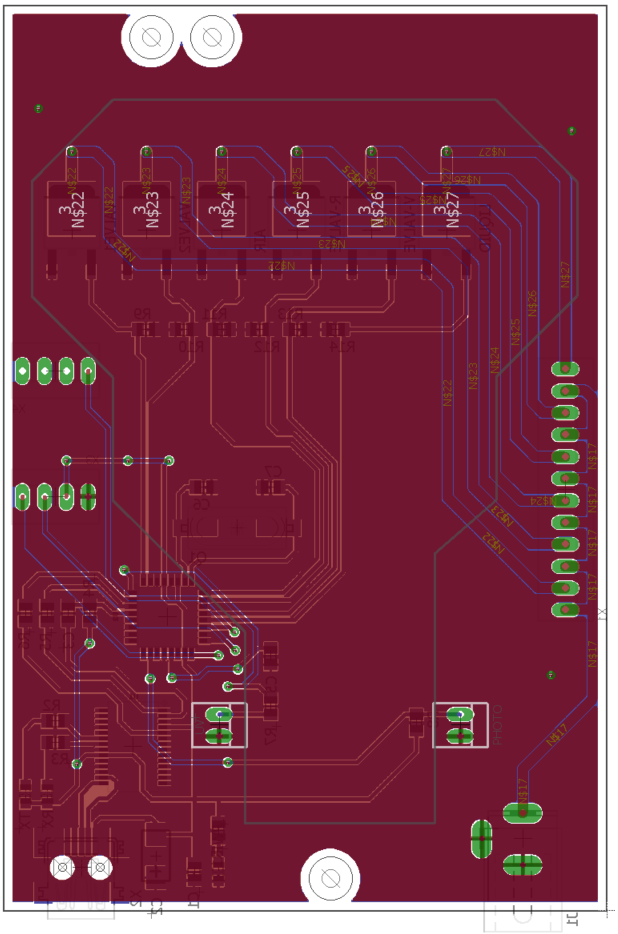

Figure D.1: CAD design of the control OCB for the integrated device

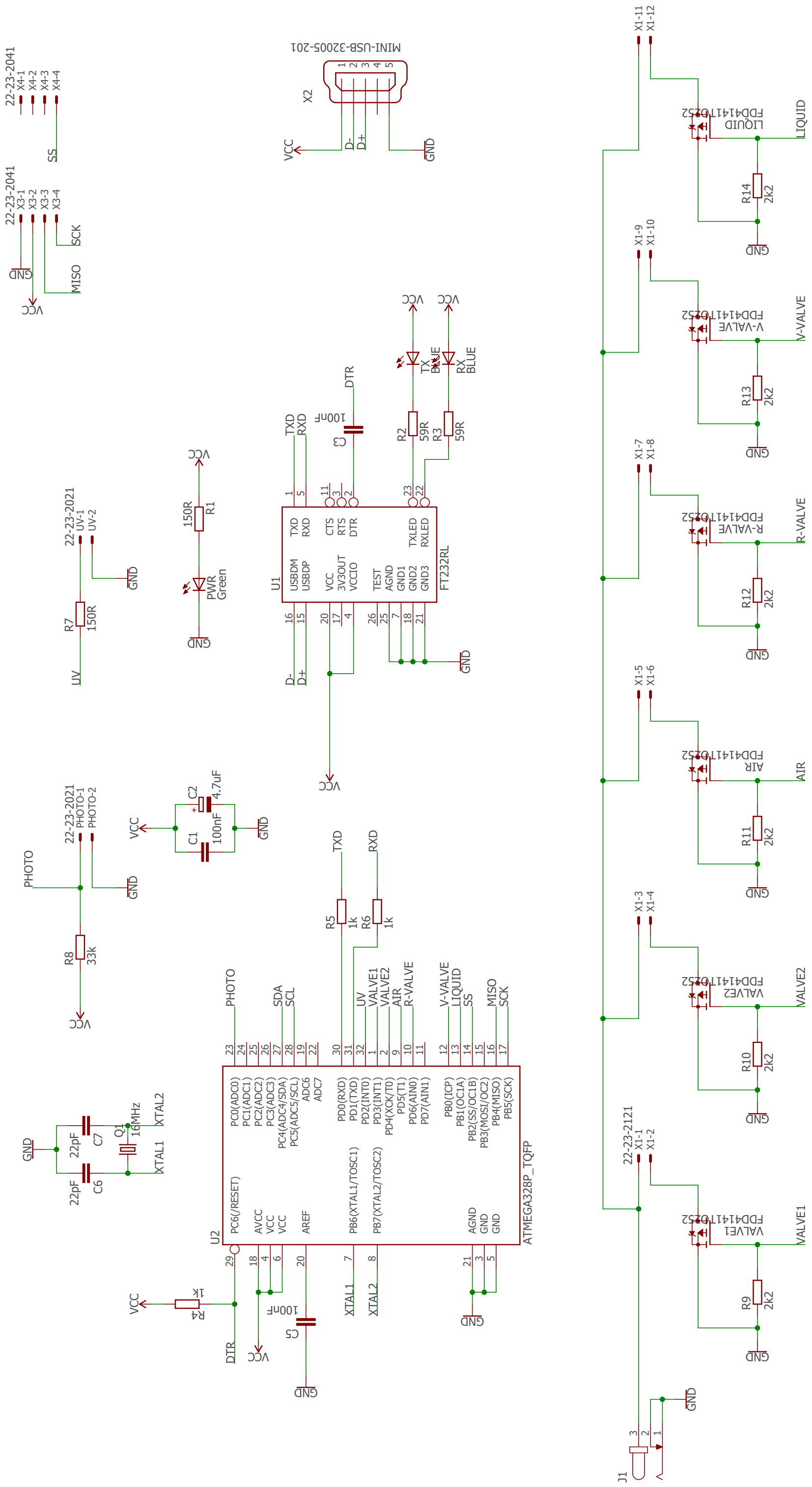

Figure D.2: Schematics of PCB for the integrated device

Table D.1: Bill of material of the final PCB, prices as of 10/02/2019

Item	Quantity	Manufacturer	Manufacturer code	Seller code	Unit cost
		Farnell			
MCU ATmega 328p	1	Microchip	ATMEGA328P-AU	1715468	£2.50
5 Psi digital pressure sensor	1	Honeywell	HSCDANN005PGSA5	1823234	£35.65
		RS Components			
33 kΩ resistor	1	Panasonic	ERA6AEB333V	566-187	£0.10
2.2 KΩ resistor	6	TE Connectivity	CPF0805B2K2E	666-2540	£0.11
1 kΩ resistor	3	TE Connectivity	RN73C2A1K0B	215-2428	£0.60
150 Ω resistor	2	TE Connectivity	RN73C2A150RB	215-1554	£0.46
59 Ω resistor	2	TE Connectivity	RN73C2A59RB	614-5288	£0.50
4.7 µF capacitor	1	AVX	TAJC475K025R	699-3009	£0.36
100 nF capacitor	3	KEMET	C0805C104K5RACTU	264-4416	£0.02
22 pF capacitor	2	KEMET	C0805C220J5GACTU	264-4416	£0.03
400 nm LED	1	Bivar	LED3-UV-400-30	454-4396	£3.32
Blue LED	2	Kingbright	KP-2012MBC	466-3762	£0.51
Green LED	1	VCC	CMD17-21VGC/TR8	137-1403	£0.18
Visible light phototransitor	1	Vishay	TEPT4400	700-0776	£0.29
N-channel MOSFET	6	Infineon	IPD100N04S4-02	110-7111	£0.58
16 MHz crystal	1	Fox Electronics	FOXSDLF/160-20	547-6531	£0.35
USB-serial chip	1	FTDI	FT232RL	406-480	£3.14
Mini USB	1	ASSMANN WSW	A-USB B-M5-SMD-C	674-1369	£1.54
DC plug	1	RS Pro	448-382	448-382	£0.61
12 pin PCB connector	1	Preci-Dip	800-80-012-20-001101	701-9806	£1.16
2 pin PCB connector	1	Preci-Dip	800-80-002-30-480101	701-9922	£0.18
				Total cost	**£52.16**

D.2 Proportional valve calibration data

Table D.2: Calibration data for valve 1

P (mbar)	#1 (V)	#2 (V)	#3 (V)	#4 (V)
136	0.313	0.270	0.240	0.229
119	0.738	0.768	0.714	0.749
102	1.135	1.042	1.095	0.953
85	1.263	1.211	1.296	1.192
68	1.379	1.305	1.315	1.242
51	1.374	1.320	1.361	1.272
34	1.418	1.373	1.403	1.330
17	1.444	1.383	1.403	1.340
0	1.446	1.383	1.437	1.334

Table D.3: Calibration data for valve 2

P (mbar)	#1 (V)	#2 (V)	#3 (V)	#4 (V)
136	2.301	2.273	2.306	2.209
119	1.964	1.964	1.965	1.860
102	1.750	1.696	1.676	1.648
85	1.612	1.554	1.552	1.487
68	1.539	1.496	1.497	1.439
51	1.481	1.403	1.424	1.427
34	1.506	1.431	1.382	1.388
17	1.508	1.410	1.416	1.369
0	1.511	1.369	1.423	1.314

D.3 Kinetic analysis

D.3.1 Well plate analysis data

Table D.4: Raw data form the multi mode reader

[S] (mM)	V (mM.s^1/µg.ml^1)
0	0
0.009	2.03252
0.0189	2.54065
0.0378	4.6748
0.0765	4.36992
0.153	8.92276
0.306	11.34146
0.612	12.8252